THE FLUXES OF SECONDARY GAMMA RAYS OBSERVED AT LOW EARTH POLAR ORBIT

A

THESIS

Presented to the Faculty of Science
of the P. J. Šafárik University

in Partial Fulfillment of the Requirements
for the Degree of

DOCTOR OF PHILOSOPHY

By

RNDr. Radoslav Bučík

Košice, Slovakia

December 2003

Abstract

The study of spatial distribution (in geographic and L-B coordinates) of low-energy gamma rays and their temporal variability in the spring of 1994 is examined using data from the low altitude polar-orbiting CORONAS-I satellite. Gamma rays in two energy channels $0.12 - 0.32$ MeV, $3 - 8.3$ MeV were measured by omnidirectional scintillation counter with large effective area (up to 250 cm^2).

Here we present geographical gamma-ray intensity map, averaged over the four-month period. Latitudinal effect studied for high energies is in a good agreement with earlier literature calculation assuming their production by primary cosmic rays and their secondaries in atmosphere and/or any local (spacecraft, instruments) matter. Comparison with previous satellite and balloon-borne experiments is done; contribution of local gamma rays to total detected flux is discussed. The irregular spatial structures of gamma-ray flux increases in subauroral zone and at lower latitudes are investigated. The most intense of them are detected at regions where the particles are mostly stable trapped.

The distribution of average gamma-ray fluxes in invariant L-B coordinate system is constructed and comparison with the energetic electrons measured on the same satellite is done. The enhanced fluxes in inner zone are well organized according to the minimum magnetic field strength at 100 km. Energy spectral characteristics of gamma-ray fluxes in the South Atlantic Anomaly are studied and compared with the NASA AE-8 trapped radiation model. Analysis of the spectral indices of bremsstrahlung photons indicates a significant contribution of albedo electrons to the total trapped electron flux in the inner boundary of outer radiation zone.

To explain the presence of the enhanced fluxes observed over the whole outer zone at CORONAS-I altitude we follow the temporal behavior of gamma-ray flux in atmospheric drift loss cone. Correlation with SAMPEX and CORONAS-I drift loss cone relativistic electrons is reported during the couple of magnetic storms in spring of 1994.

By the Monte Carlo simulation, the average mass thickness over various solid angles viewed by scintillation crystal is evaluated. On the base this value the detector field of view is qualified and local gamma-ray bremsstrahlung production is estimated.

Thus, the first time scheme of the composition of the overall gamma-ray flux at low altitudes with help of relatively high number of measurements ($\sim 1.8 \times 10^6$ data points) is proposed.

Contents

List of Figures

List of Tables

Acknowledgements

First I would like to express my heartfelt gratitude to my advisor, Karel Kudela. His abundant knowledge always stimulated and guided me. Without his advice and discussions with him, I could not carry out my study at all. I would like to thank Sergei Kuznetsov, who was principal investigator of the Solar Cosmic Rays (SCR) experiment on CORONAS-I, for many fruitful discussions. I am indebted to SCR team members at Institute of Nuclear Physics, Moscow State University. I thank Irina Myagkova, Andrei Bogomolov, Alexei Dmitriev and Sergei Ryumin for their help in understanding instrument operation and data analysis. I would like to thank John Blake at the Aerospace Corporation, Los Angeles for valuable advice and providing SAMPEX EHi electron data. Furthermore, I thank my colleagues at Department of Space Physics for their great support. My thank goes especially to Jana Štetiarová for introducing to IDL programming. I would also like to thank my former colleagues at Department of Mathematics, Technical University in Zvolen. Finally, I thank my family for their love and care, and especially my wife Jana. During the course of this thesis I have received financial support from Committee on Space Research (COSPAR) and the Copernicus Gesellschaft e.V. This work was supported by Slovak Scientific Grant Agency VEGA under grant 2/1147/21.

Chapter 1

Introduction

Gamma rays are produced in a variety of physical processes including both particle field and particle matter production mechanisms. Observation of these energetic photons provides a direct information on high-energy phenomena in many sites through Universe, ranging from magnetospheres to galaxies.

Low energy gamma rays, say up to 10 MeV, are the most penetrating photons encountered in the nature, giving possibility to probe source objects practically without losing information due to scattering. As a added bonus this gamma-ray domain covers discrete emissions lines. However, this striking features make low-energy gamma range as a one of the least explored energy regions in the gamma-ray observations. Due to low absorption probability of low-energy gamma rays in the matter the detection cosmic gamma rays requires the massive gamma-ray telescopes. At the top of the Earth's atmosphere or on a space platforms, regions charged by intense particle fluxes, low-energy gamma radiation is high and extremely complex in origin.

The main goal of this thesis is to study spatial and energy-spectral distribution of the secondary low-energy gamma-ray fluxes in the near-Earth's space environment. The emphasis concentrates on relation with primary cosmic rays and magnetospheric electrons which is aimed at contribution to the complex gamma-ray production scheme in satellite experiments.

The detailed statistical study of hard X or gamma-ray fluxes revealing the world-wide features of the flux distribution in the inner magnetosphere have not yet been performed.

More often, the particular characteristics have been studied at balloon or satellite platforms. There were only case studies based on the couple of orbits in the satellite experiments, which were preferable at low-latitude orbits. The primary reason follows from the fact that atmospheric background is minimal at equatorial region, to have a better conditions for extraterrestrial gamma radiation measurements.

In contrary of gamma radiation the fluxes of secondary protons and electrons in inner magnetosphere, primarily those in the radiation belts have been mapped in detail for a relatively long time. Except empirical models of radiation belts (AE [*Vette*, 1991] and CRRESELE [*Brautigam and Bell*, 1995] electrons, AP [*Sawyer and Vette*, 1976] and CRRESPRO [*Meffert and Gussenhoven*, 1994] protons) many efforts have been expended to model theoretically, particularly, highly variable fluxes in outer radiation belt [e.g. *Beutier and Boscher*, 1995; *Abel and Thorne*, 1999; *Khazanov et al.*, 1999; *Summers and Ma*, 2000].

The direct measurement of the electron precipitation, which is limited on the satellite vicinity, gives detailed measurements of the local environment. The remotely bremsstrahlung technique, due to low absorption of this radiation, becomes an important tool to study worldwide pattern of this phenomena, providing a different perspective on the precipitation process. Since the population of trapped energetic particles in the geomagnetic field have a dependence on the level of solar activity the measurements of low-energy gamma rays can be useful for indirect update of the existing empirical radiation models of the charged particle fluxes.

In this work we use gamma-ray data acquired by low altitude high inclination CORONAS-I satellite with the SONG instrument, developed at the Institute of Experimental Physics, Slovak Academy of Sciences in cooperation with the Institute of Nuclear Physics, Moscow State University. The polar orbit of the CORONAS-I satellite allows to scan all geomagnetic latitudes and to pass through the both inner and outer radiation belts. In addition, during the four-month observation period in March-June, 1994, the big amount of the data were accumulated.

The SONG instrument, was primarily intended to measure gamma-ray solar flare emissions during the time of the maximum of the 22nd solar cycle, where these emissions are more often and more intense. However, some technical and financial problems caused delayed of the CORONAS-I mission, and in fact the SONG instrument was operated in the declining phase of the 22nd solar cycle near the solar activity minimum. No solar events were observed during the March-June, 1994 according to the bursts list compiled by *S. V. Bogovalov*, 1994 [unpublished data] from 19 spacecraft observations. Therefore as a by-product analysis, the background conditions for detection of solar or other extraterrestrial emissions may be investigated.

Recently, updated version of the SONG device operates in wide energy range of $0.028 - 100$ MeV in new CORONAS (Complex Orbital Near-Earth Observations of the Activity of the Sun) mission, started by launching of the CORONAS-F satellite on July 31, 2001 [*Kuznetsov et al.*, 2002a], strictly in time of the maximum of the next, 23rd solar cycle. In its declining phase, high-energy solar gamma-ray emission was observed during the largest solar flare of the last two solar cycles on October 28, 2003. At present, except CORONAS-F, the hard electromagnetic radiation from the Sun is measured by low altitude (~ 600 km) RHESSI [*Lin et al.*, 2002] satellite, from thermal X-ray through nuclear gamma-ray line energies.

The work is divided into seven chapters, three appendices and bibliography. In the following text objectives and particular tasks aimed to investigate in this work are listed (chapter 2). Chapter 3 gives a summary of the current status and physical interpretation of gamma-ray observations. The subject matter is divided into two topics, secondary gamma radiation, and primary cosmic gamma rays, with concentration on atmospheric and artificial production by primary cosmic rays and population of trapped particles. A short description of experiment is given in chapter 4, where the observations are presented in geographic maps. Chapter 5 presents latitudinal distribution of the gamma-ray fluxes observed outside the radiation belts and effect of the albedo particles is examined. In chapter 6, data in magnetic coordinates and in the loss cones are modeled, and gamma-ray flux composition is discussed. Energy spectral characteristics are compared with AE-8 model and temporal variations of the electron fluxes are surveyed. Finally, conclusions are stated in chapter 7.

The appendices are organized as follows: the calculation of the power-low spectral index is outlined in appendix A; in appendix B a model of matter distribution on CORONAS-I satellite is presented; appendix C describes concept of the experimental database development.

Chapter 2

Objectives of the Thesis

This thesis is devoted to the study of secondary gamma-ray fluxes distribution, spatial and energy, in the near Earth's space environment. The emphasis is given on relation to the primary cosmic rays and the magnetospheric electrons. We attempt to study three main topics.

The study of the gamma-ray component due to primary cosmic rays and charged albedo particles above the atmosphere seen by satellite at low Earth's polar orbit.

In general we attempt to investigate

- The spatial distribution of low-energy gamma-ray fluxes in the geographical coordinates at altitude of ~ 500 km
- The latitudinal distribution of the secondary gamma-ray fluxes and comparison to the similar one for charged energetic particles
- Local time dependence of the gamma rays in relation to the local gamma-ray contribution
- Short – term variations of the primary cosmic rays above the Earth's atmosphere during the magnetic storms: latitudinal dependence and charged albedo effects
- Differential gamma-ray energy spectra at the equatorial and polar regions

- Estimation of the primary cosmic-ray induced contribution in the observed gamma-ray flux

The study of the gamma-ray component related to the magnetospheric electrons

Here we attempt to investigate

- The spatial distribution of the gamma-ray fluxes in the invariant magnetic coordinates L, B at constant altitude; comparison with available electron data in $L-B$ space
- L, B profile of the gamma-ray differential energy spectra and comparison with electron energy spectra (e. g. NASA AE electron model)
- Local bremsstrahlung production of the gamma-ray photons by the energetic electrons stopped in the vicinity of the detector
- Temporal variations of the gamma-ray fluxes in the atmospheric drift loss cone over the L-shells and connection with relativistic electron enhancements

The detector shielding in SONG/CsI environment on CORONAS-I satellite

By modeling of the matter distribution we attempt to

- Evaluate the nominal 4π detector field of view
- Estimate of the average thickness of the material for calculation of the local gamma-ray production

In order to accomplish all stated problems the database of the gamma-ray observations must be developed. This additional task is comprised of

- Obtaining and archiving of the data
- Analyzing of the raw data and identifying of the measurement's errors
- Development of the codes for calculation of the satellite position and required geomagnetic and astronomical parameters

Chapter 3

Current Status and Physical Interpretation of Gamma-Ray Observations

Generally, gamma radiation measured at balloon and near-Earth satellite experiment has primary (cosmic) and secondary components. The cosmic component may be the sum from the emission of various discrete gamma-ray sources plus the contribution of a diffuse emission. Important localised source presents the Sun during the solar flares. Diffuse gamma radiation consists of isotropic extragalactic and anisotropic galactic components. Secondary gamma rays come from interactions of primary cosmic-ray particles with nuclei in the upper atmosphere and materials around the detector or in the detector itself. When the detector is positioned in the trapped radiation belts this enhancement can become more important, mainly during electron precipitation events. Complex information about gamma rays production in space in the region 100 keV to 100 MeV can be found in *Chupp* [1976].

3.1 Secondary Component of Gamma Radiation

Fig. 3.1 illustrates the interactions cosmic-ray particles may have after entry into the atmosphere. Likewise these processes also occur upon interaction with material such as a spacecraft [*Dean et al.*, 1991]. A large number of secondary particles, such as protons, neu-

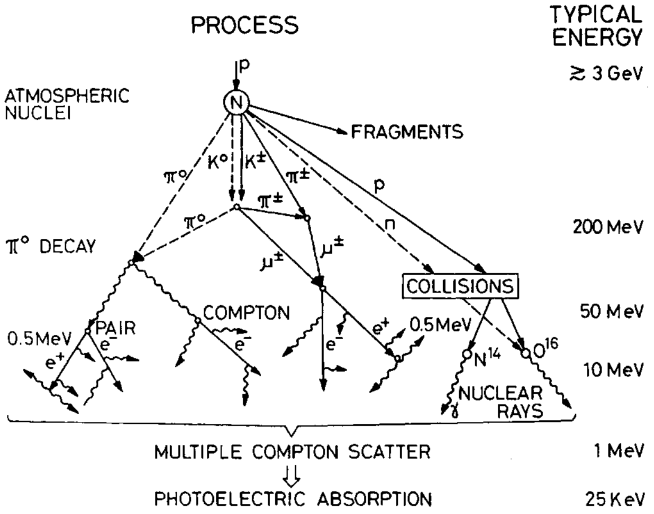

Figure 3.1. Secondary particle production by cosmic rays within the Earth's atmosphere [from *Allkofer and Grieder*, 1984].

trons and pions, etc. are generated. A charged pion decays first to muons which then decay to electrons $\pi^{\pm} \longrightarrow \mu^{\pm} \longrightarrow e^{\pm}$; a neutral pion decays immediately to two gamma rays $\pi^{\circ} \longrightarrow 2\gamma$. These gamma rays ($\sim$ 70 MeV) subsequently interact with other nuclei through pair production $\gamma \longrightarrow e^{+} + e^{-}$ and give rise to relativistic electrons. Another processes from which the electrons are generated include knock-on electrons ejected by primary cosmic-ray nuclei or by muons. Left panel of the Fig. 3.2 shows calculated production spectra at the top of the atmosphere ($\sim$ 0 g cm^{-2}, no attenuation is considered) of electrons and photons near the solar minimum. Solid curves are for a geomagnetic cutoff $<$ 0.5 GV, dashed curves are for 4.5 GV. Electrons produced in all the above interactions then produce gamma rays through bremsstrahlung, which is the main source of the low-energy gamma rays.

Although the major fraction of the secondary flux of gamma rays originates in the interactions of cosmic-ray nuclei with air and/or spacecraft constituent nuclei, secondary photons are also produced by electrons arriving from outer space [*Beuermann*, 1971]. These are primary electrons if their energy is above the local geomagnetic cutoff, which present only about 1% of the nucleonic component of the cosmic-ray flux. Below that threshold, only reentrant albedo electrons can enter the atmosphere [*Barwick et al.*, 1998]. These electrons

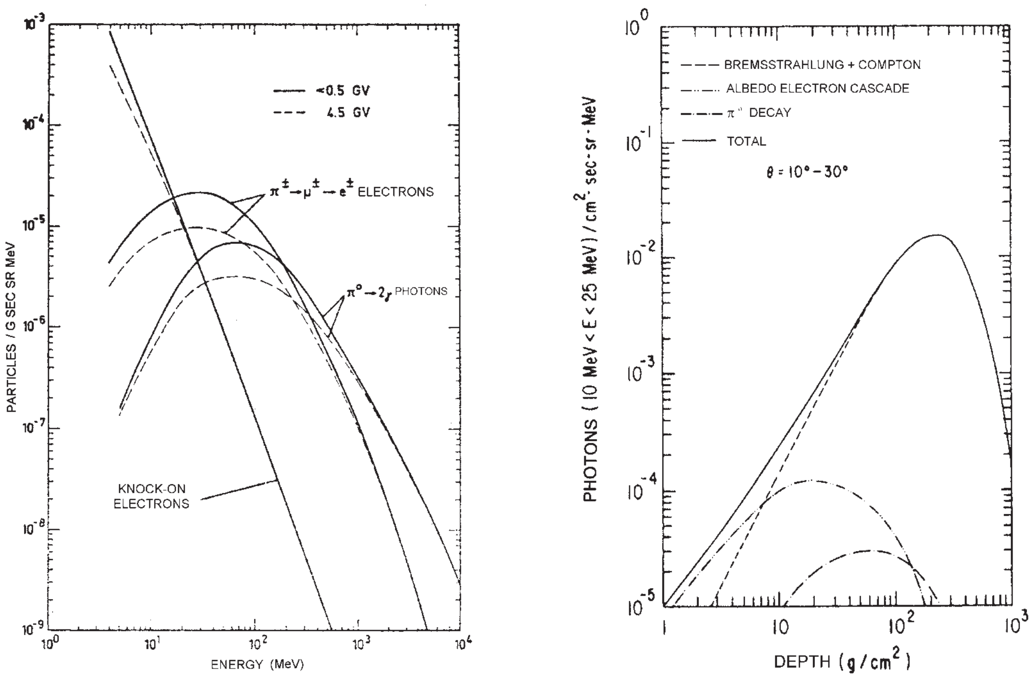

Figure 3.2. (*left*) Production spectra of downward-moving electrons and photons in 1968 for two different values of the geomagnetic cutoff [from *Beuermann*, 1971]. (*right*) Calculated growth curves for the downward medium-energy gamma-ray intensity at middle latitudes showing contributions of various production mechanisms [from *Morris*, 1984].

are originally produced inside the atmosphere and then leave it as splash albedo electrons. If their energy is below the geomagnetic cutoff, they are reflected by the Earth's magnetic field and fall back into the atmosphere in the other hemisphere [*Daniel and Stephens*, 1974]. Gamma rays produced as the results of bremsstrahlung processes of these electrons are assumed to be nearly isotropically distributed [*Dean et al.*, 1991].

In low energy region (below ~ 1 MeV) there is another strong component of bremsstrahlung gamma rays associated with electron precipitation from the radiation belts [*Imhof et al.*, 1976].

The line component of the atmospheric gamma-ray spectrum is dominated by the 0.511 MeV line from positron-electron annihilation. Other possible production mechanisms include inelastic scattering and spallation reactions on oxygen and nitrogen nuclei by atmospheric protons and neutrons. The most intense gamma-ray lines include for example: 4.44

MeV line from ^{12}C and ^{11}B, or 6.1 MeV line from ^{16}O [*Willett and Mahoney*, 1992; *Letaw et al.*, 1989]. However, the contribution of these lines to the gamma-ray production is negligible. *Martin et al.* [1975] reported that it presents only $\sim 5\%$ of the total atmospheric gamma-ray flux.

Gamma-ray lines produced by solar energetic particle impact of the Earth's atmosphere were first detected by the Solar Maximum Mission (SMM) spectrometer during the intense 20 October 1989 shock event [*Share and Murphy*, 2001]. The recent observation of gamma-ray lines and continuum emitted by the Earth's atmosphere was reported by *Share et al.* [2002] during the 21 April, 2002 solar energetic particle (SEP) event.

3.1.1 Atmospheric Gamma Radiation Due to Primary Cosmic Rays

Atmospheric gamma rays have been studied by several experiments both inside and outside the atmosphere, and in the wide range of energies. We primarily concentrate on low energy (below 10 MeV) gamma rays present above the atmosphere.

Balloon Altitudes

Gamma rays are produced as part of the nucleon-meson-electromagnetic cascade initiated when a cosmic ray strikes the atmosphere. These cascades are largely collimated in the direction of the incident cosmic ray, increasingly so at higher cosmic-ray energies. As the cascade progresses into atmosphere, the number of secondary particles increases, while the average energy per particle decreases. The result is the familiar 'growth curve' showing the gamma-ray intensity as a function of the depth in the atmosphere. An example of the calculated growth curve is shown on the right of the Fig. 3.2 [*Morris*, 1984], which include the contribution of various production mechanisms. The intensity of the secondary gamma radiation increases approximately linearly with atmospheric depth up to between 100 and 200 g cm^{-2}. At larger depths, absorption and energy losses produce a decrease in the intensity.

Fluxes of atmospheric gamma rays were measured and calculated for various arrival directions of secondary photons, characterized by zenith angle θ : horizontal ($\theta \sim \pi/2$), upward ($\theta \sim \pi$), downward ($\theta \sim 0$) flux, and for various atmospheric depths. Differential energy spectrum has been approximated by power low with negative spectral index between

-1 and -2, depending at least on energy, atmospheric depth, local rigidity, and arrival direction. Generally, towards the high energies observed and predicted gamma-ray spectrum becomes softer-approaches to the value of -2 [e.g. *Beuermann*, 1971; *Daniel and Stephens*, 1974; *Ling and Gruber*, 1977; *Ryan et al.*, 1979].

Spectral index (measured and calculated) of 4π-flux of gamma rays at middle latitudes ($R_c \sim 4.5$ GV), at floating altitude of 3.5 g cm^{-2} in energy interval from $0.3 - 10$ MeV have values between -1.5 and -1.4 [*Martin et al.*, 1971; *Ling*, 1975]. Energy spectrum measured at altitude of 4.8 g cm^{-2} residual atmosphere, at middle latitude (~ 4.3 GV) has for downward flux value of -1.5, and for upward flux -2.1 [*Akyüz et al.*, 1997]. In the energy range $4 - 45$ MeV experimental value of spectral index for downward direction has value of -1.4 and for upward direction value of -1.9 [*da Costa Ferreira Neri et al.*, 1992]. The slope of the energy spectrum of downward flux in experiment for energies between $2 - 25$ MeV is -1.5 [*Ryan et al.*, 1979]. It seems that upward moving photons have somewhat softer energy spectrum than the downward one. Since the upward moving radiation was observed independent of atmospheric depth near the top of the atmosphere, is assumed to be secondary upward radiation produced deeper in the atmosphere where the particles posses fewer energy (due to dissipation) than near the top [*Akyüz et al.*, 1997].

Contribution from decay of π° mezons dominates of higher energy gamma-ray flux and at the top of the atmosphere due to exceedingly short half-life time of neutral pion. Component from muons (decaying to electrons) is important deep in the atmosphere because of their weak nuclear interacting properties and relatively long lifetime. At low energy region, the main source of downward moving gamma rays at high altitudes (~ 3 g cm^{-2}) comes from bremsstrahlung of primary and reentrant electrons. The contribution from π° decay to the measured flux at these energies is less than 1% at 2.5 g cm^{-2} [*Graser and Schönfelder*, 1977]. Deeper into the atmosphere gamma rays arise from bremsstrahlung of electrons produced in showers. These electrons are mainly responsible for production upward gamma-ray fluxes [e.g. *Beuermann*, 1971; *Ryan et al.*, 1979; *Ling*, 1975; *Morris*, 1984]. At the top of the atmosphere, the fluxes toward the horizon become more intense due to increasing of thickness of the atmosphere seen by detector [*Fichtel et al.*, 1969]. So the horizontal flux corresponds roughly to the downward flux at great depth [*Morris*, 1984].

The balloon observations indicate that gamma-ray energy spectrum becomes harder toward the high geomagnetic cutoff. At higher rigidities, proportional more high-energy primary cosmic rays enter the atmosphere and produce a harder spectrum than at the lower rigidities. *Kasturirangan et al.* [1972] reported that the flux of 0.511 MeV photons reduces by a factor of 9 at 6 g cm^{-2} in going down from polar regions ($R_c \sim 1.3$ GV) to equatorial latitudes ($R_c \sim 16.9$ GV). *Martin et al.* [1971] found that at the top of the atmosphere (4 g cm^{-2}) the ratio of the measured gamma-ray flux at 14.1 GV and 3.6 GV is 3.

Calculations of *Morris* [1984] also reveal significant solar modulation effect on gamma-ray intensities near the top of the atmosphere. At solar minimum the gamma-ray intensity is about 20% greater than at solar maximum as is calculated for the middle latitudes. The intensity variation of the atmospheric gamma-ray lines with solar activity has been recently reported by *Harris et al.* [2003].

Satellite Altitudes

In order to be detected by a satellite, gamma rays must escape from the atmosphere. Two processes can lead to such escaping gamma rays. In first of these a small fraction of the cosmic-ray interactions produce secondaries at large angles to the incident directions, including some which travel upward in the atmosphere [*Thompson et al.*, 1981]. For example, there is experimental and theoretical evidence about a nearly isotropic production of low-energy pions with kinetic energy below ∼ 200 MeV [*Beuermann*, 1971].

The second source of escaping gamma rays arises from the curvature of the atmosphere. Cosmic rays which, strike the atmosphere at grazing incidence can initiate cascades which will penetrate through the top portions of the atmosphere and emerge before being absorbed. Viewed from outside the atmosphere, these penetrating cascades produce the strong horizon fluxes [*Gur'yan et al.*, 1979; *Thompson et al.*, 1981].

The flux of gamma rays coming directly upward from the Earth's atmosphere at satellite altitudes is essentially the same at the balloon altitudes (~ 3 g cm^{-2}), basically because at the gamma-ray energies of concern the interactions mean free pats are much greater than 3 g cm^{-2}, and at these positions the production of the upward flux practically does not vary with depth.

At energies between 40 keV and 2.7 MeV, *Imhof et al.* [1976] found that over the polar caps the gamma-ray energy spectra are similar to those observed near the magnetic equator, and the intensities are higher by about a factor of 4. The two differential energy spectra of the upcoming atmospheric component were represented by power laws

$$J = 1.723\, E^{-1.34\pm 0.03} \qquad \text{ph (cm}^2\text{ s sr keV)}^{-1}\ R_c = 3\text{ GV} \tag{3.1}$$

$$J = 0.591\, E^{-1.39\pm 0.03} \qquad \text{ph (cm}^2\text{ s sr keV)}^{-1}\ R_c = 14.5\text{ GV} \tag{3.2}$$

Mazets et al. [1975] have measured a rigidity dependence of 511 keV line intensity produced in atmosphere, which they assumed also applied to the continuum due to similar production mechanisms. From their analytical fit

$$J_{511} = 0.21\,(0.046 + \exp(-R/8.5)) \quad \text{ph cm}^{-2}\text{ s}^{-1} \tag{3.3}$$

valid within the $3 - 17.5$ GV, one obtains a ratio of 3.3 for the relative intensities at 3 and 14.5 GV, which compares with a factor of 3 as measured in above experiment [*Imhof et al.*, 1976]. Over the $3 - 17.5$ GV, atmospheric gamma-ray spectra deduced from data are

$$J = 0.54\, E^{-1.55\pm 0.10} \qquad \text{ph (cm}^2\text{ s MeV)}^{-1}\ 0.07 < E < 1\text{ MeV} \tag{3.4}$$

$$J = 0.68\, E^{-1.1\pm 0.2} \qquad \text{ph (cm}^2\text{ s MeV)}^{-1}\ 1 < E < 4.1\text{ MeV} \tag{3.5}$$

Gur'yan et al. [1979] found that for $R_c > 4$ GV the upcoming flux of gamma radiation is proportional to $R^{-1.13}$ using data above 80 MeV from high-inclination satellite. There was not observed the statistically significant rigidity dependence of the gamma-ray energy spectrum. The calculation of *Thompson* [1974] yields a dependence of $R^{-1.2}$ for upcoming radiation above 30 MeV. This is consistent with *Thompson et al.* [1981] observations of upcoming gamma rays at energies $>$ 35 MeV. In this experiment the gamma radiation coming from horizon is about an order of magnitude more intense than the radiation coming from the nadir (upcoming). The east-west asymmetry near the equator was also reported. Gamma-ray intensity shows maximum from the west and minimum from the east, reflecting the maximum value of the geomagnetic threshold in east direction for positively charged energy particles [*Rossi and Olbert*, 1970]. Predominance of western gamma-ray flux was also pointed out by *Morris* [1984] in both calculation and data.

The latitudinal dependences of gamma-ray fluxes on massive Salute-7-Kosmos-1686 orbital complex ($\sim 5 \times 10^4$ kg) and Mir orbital station (1.2×10^5 kg) are similar to $1/R$ for energy > 3 MeV and rigidity range of $3 - 15$ GV [*Bogomolov et al.*, 1999, 2002]. Salute-7-Kosmos-1686 gamma-ray energy spectrum between $1.5 - 65$ MeV does not vary with R_c in range $3 - 16$ GV and was approximated by power law with index of -1.44. Gamma-ray flux at middle latitudes (~ 3 GV) is about factor 3 higher than at the equator [*Bogomolov et al.*, 1996, 1998b]. In these experiments, the absolute values of the detected gamma-ray fluxes are significantly higher than those measured near the top of the atmosphere or on the lightweight astronomical satellites (e.g. CORONAS-I). The CORONAS-I gamma-ray fluxes (> 3 MeV) are lower about factor 5 and factor 2 in comparison with radiation detected on Mir and Salute-7-Kosmos-1686 platforms, respectively. *Bogomolov et al.* [1999, 1998a] found that gamma-ray fluxes are approximately linear dependent to the spacecraft mass. Authors also propose the main part of the detected gamma-ray flux on board massive spacecrafts is due to locally produced gamma rays in the ambient material. The similarity in latitude dependences confirms the similar nature of atmospheric albedo and local produced gamma rays, which are both caused by interactions of primary cosmic rays.

3.1.2 Atmospheric Bremsstrahlung Gamma Rays

Atmospheric bremsstrahlung X/gamma rays result from collision between precipitating energetic electrons and neutral atmospheric constituents. At low energies, the bremsstrahlung is emitted fairly isotropically, and gamma rays undergo little attenuation before exiting the top of the atmosphere.

Bremsstrahlung X rays driven by electron precipitation from the Earth's trapped radiation belts have been studied for long time [e.g. *Imhof*, 1981]. At higher altitudes, suggested causative mechanisms range from: (1) self-generated instabilities associated with exceeding the trapping limit [*Kennel and Petchek*, 1966], (2) lightning-produced whistler waves [e.g. *Voss et al.*, 1984], (3) ground-based VLF transmitter activity [e.g. *Vampola and Gorney*, 1983], and (5) enhanced, substorms-associated VLF chorus and plasmaspheric hiss intensities [e.g. *Imhof et al.*, 1986]. At lower altitudes, losses occur via Coulomb collisions with the atmospheric constituents, nearly independent of geomagnetic activity [*Lyons*, 1997]. Another source of atmospheric hard X rays from energetic electrons generated directly by upward lightning discharges has been proposed recently [e.g. *Fishman et al.*, 1994].

Satellite observations of bremsstrahlung have been used as a remote sensing technique to map the global distribution of electron energy deposition [*Imhof et al.*, 1974]. With this method it is possible to obtain a large-scale mapping of the precipitation, to separate temporal and spatial effects, and to obtain information on the energy spectrum of the electrons. The technique of measuring bremsstrahlung X rays from a satellite offers several important advantages: a large area of the atmosphere can be continually surveyed for electron precipitation, and this radiation is much more penetrating than are its parent electrons. Direct observations of precipitating electrons provide more detailed measurements over a very narrow region of space, however, in order to understand major electron precipitation events it is important to observe the phenomena also on a wide-spread scale.

Although electrons are almost continually precipitating at high latitudes, during magnetically quiet times the fluxes of energetic X rays emitted upward from the atmosphere over the polar regions of the Earth are often close to the albedo gamma radiation. At times of high geomagnetic activity, however, large fluxes of electrons are frequently precipitating into the atmosphere and these produce significant intensities of bremsstrahlung X rays [*Imhof*, 1981].

The importance of the bremsstrahlung contribution to the electron counting rate of the particle detectors has been recently pointed out by *Cayton et al.* [2003].

3.1.3 Local Production-Background

Photon-Electron Induced Radiation

Gamma rays considered here are part of the electron-photon cascades, which result from cosmic-ray interactions with the nuclei within the structure of the spacecraft. The precise background flux depends on the shape, mass and construction material of the spacecraft. All these factors make the gamma-ray flux of this nature a very complicated contribution to estimate. One of the methods assumed the locally produced gamma rays have the same spectral shape as the atmospheric gamma rays, but with the reduced intensity (~ 0.2). This approximation is derived from measurements aboard very massive (10^5 kg) Apollo 17 spacecraft compared to the normal astronomical satellites, which means that this method overestimates the local gamma-ray flux. Overall, the photon-electron background, for past satellite experiments, contributed a minor fraction ($< 5\%$) of the total detected gamma-ray flux [*Dean et al.*, 2003, and reference therein].

Except background due to primary cosmic rays, *Chupp* [1976] discuss bremsstrahlung background from radiation belt electrons stopping in the satellite near the detector.

Hadron Induced Radiation

In low-energy gamma-ray region, both the material of the satellite platform and the spectrometer itself become intense source of discrete gamma-ray lines superimposed on a continuum. These emissions (prompt or delayed due to activation) are highly dependent on the detailed design of the spectrometer and the environment in which it is operated. It is currently impossible to provide a generalized model, which is capable of offering a realistic estimate of the behavior of this type of background for a given spectrometer.

The origin of the lines are natural radioactivity, activation of the instrument material by cosmic-ray protons, trapped protons, and secondary neutrons, as well as a 511 keV contribution from the annihilation of the positrons produced within and near to the telescope. Here we concentrate on the non-photonic sources of instrument gamma radiation derived from heavy particle interactions.

Nuclei involved in proton bombardment are generally left in a long-lived excited state and may return to the ground state with the emission of a gamma-ray. This type of radiation cannot be eliminated by use of the veto counter because of the finite ($< \mu$s) length of the veto pulse.

Secondary low-energy protons (< 100 MeV) do not provide a significant contribution to the gamma radiation, due to fact they are brought to rest quickly by ionization. Neutrons produced in the materials which surround the primary detector, such as the spacecraft, the veto system itself and the atmosphere, are capable of producing gamma radiation by elastic and inelastic scattering as well as by thermal capture. The target nucleus, which is left in an excited state, my return to the ground state by emitting a gamma-ray.

The continuum has its origin in β-decays derived from activation of the construction materials by cosmic-ray protons, trapped protons, and by secondary neutrons. The unstable nuclides subsequently decays, emitting a β-particle and/or gamma rays.

Radiation induced by cosmic protons approaches the asymptotic level which is attained after a long exposure period. Although the passage through the radiation belts is a comparatively short time compared to the orbit, the intense proton flux which can be as high as 10^5 protons cm^{-2} s^{-1} (> 100 MeV) will led to the activation of long lived radioisotopes within the crystals. These radioisotopes will produce gamma radiation long after the passage thorough the belts. *Dean et al.* [1989] reported that spallation noise spectra due to passage through the trapped proton radiation belt is at least about one order higher than induced one due to cosmic-ray protons at polar region.

The dominant radiation feature resulting from an South Atlantic Anomaly (SAA) exposure in Oriented Scintillation Spectrometer Experiment (OSSE) on Compton Gamma Ray Observatory (CGRO) [*Johnson et al.*, 1993] is the beta-decay continuum from ^{128}I produced by the capture of secondary neutrons (produced by trapped protons) within ^{127}I in the NaI detector. The half-life of ^{128}I is 25 minutes. The radioisotope ^{128}I contributes at energies below the beta endpoint energy of 2.1 MeV. Some of the prominent gamma-ray features associated with cosmic-ray and SAA proton interactions and their products include 0.191 MeV from ^{123}I, a complex of lines near 0.25 MeV including ^{121}I (0.244 MeV) and $^{123\mathrm{m}}$Te (0.247 MeV), a complex of lines in the $0.6 - 0.7$ MeV range including ^{124}I (0.634 MeV) and ^{126}I (0.698 MeV). The instrumental induced radiation also dominates the Gamma Ray Spectrometer (GRS) counting rate spectrum below about 3 MeV [*Share et al.*, 1989] due to a long period exposure to the cosmic radiation on SMM.

3.2 Primary Cosmic Gamma Rays

3.2.1 Diffuse Gamma Rays

The cosmic gamma-ray flux is itself the sum of two components: an isotropic component with a constant flux for all galactic latitudes, and a second component of galactic origin whose flux varies with galactic latitude. The contribution of isotropic component at energies below 10 MeV is negligible, however, above ~ 150 MeV the galactic emission becomes more intense [*Lavigne et al.*, 1982].

Based on the Kosmos 461 observations, *Mazets et al.* [1975] deduced the gamma-ray diffuse spectrum in the range $60 - 400$ keV can be fitted fairly well with a power-law

$$J = 5.6 \times 10^{-3}\, E^{-2.8\pm0.05} \quad \mathrm{ph\ (cm^2\ s\ sr\ MeV)^{-1}} \tag{3.6}$$

Above 400 keV, the spectrum exhibits deviation from the power law. The measured values of the flux lie above power law extrapolation to higher energies. It is in the energy region 1 to 10 MeV where the largest experimental uncertainty lies. The latest measurements in the energy range of question on CGRO satellite [*Kappadath et al.*, 1995] demonstrated that the preliminary cosmic diffuse gamma-ray spectral shape is of the form:

$$J = 6.13 \times 10^{-3}\, E^{-2.3} \quad \mathrm{ph}\ (\mathrm{cm}^2\ \mathrm{s}\ \mathrm{sr}\ \mathrm{MeV})^{-1} \tag{3.7}$$

The question about the origin of the diffuse cosmic gamma-ray component having an astrophysical importance is still open. In most cases it was interpreted as the result of high-energy interactions in intergalactic space, including inverse Compton collisions of cosmic-ray electrons with the 2.7 K radiation, bremsstrahlung production of nonthermal electrons with intergalactic matter, interaction of cosmic-ray protons $> 10^{15}$ eV with 2.7 K radiation producing neutral pions, etc. An alternative to these 'diffuse' processes, diffuse gamma radiation is assumed to be superposition of the radiation from many unresolved external galaxies [*Schönfelder et al.*, 1980, and references therein].

3.2.2 Solar Flares and Gamma-Ray Bursts

In addition to time steady diffuse gamma radiation, a variety of cosmic transient events have been observed. These include solar gamma-ray emissions during periods of solar flares and gamma-ray bursts. In fact, many gamma-ray sources have so far been observed only by their intense transient emission.

Solar flares are the most powerful explosions, releasing up to $10^{25} - 10^{26}$ J in $10^2 - 10^3$ s, accelerating ~ 1 MeV ions up to tens of GeV and $\sim 10 - 100$ keV electrons to hundreds of MeV. How the Sun releases this energy and how it rapidly accelerates electrons and ions with such high efficiency, and to such high energies is presently unknown.

Particles accelerated by solar flares interact with the ambient solar atmosphere and create gamma rays, both lines and continuum. Line emission results from the interactions of protons and nuclei, while the continuum is from relativistic electron bremsstrahlung. Many gamma-ray flares have been observed to have durations less than 1 minute while a few have durations greater than 10 minutes. Gamma-ray lines from solar flares were first observed by *Chupp* [1976] in August 1972 with a NaI spectrometer flown on board the seventh Orbiting Solar Observatory (OSO-7). The lines were observed at 0.511 MeV from positron annihilation, at 2.223 MeV from neutron capture on ^{1}H and at 4.438 and 6.129 MeV from de-excitations of nuclear levels in ^{12}C and ^{16}O, respectively.

Gamma-ray continuum below about one MeV is electron bremsstrahlung. Continuum emission at higher energies is only rarely observed. This emission could be a combination of electron bremsstrahlung and π° meson decay.

The strongest predicted and observed line from solar flares is that at 2.223 MeV from neutron capture on hydrogen formatting deuteron, ^{1}H(n,γ)^{2}H. For example, the flux at maximum observed intensity during the June 7, 1980 and June 21, 1980 on SMM was ~ 0.07 ph cm^{-2} s^{-1}. Studies of neutron production in flares indicate that most of the neutrons responsible for this line result from the breakup of helium by protons. A significant fraction of the fastest ($>$ 100 MeV) neutrons can travel as far as the Earth before they decay, resulting in detectable neutron fluxes at the Earth following large flares. High energy solar neutrons were observed from a large flare in 1980 [*Trombka and Fichtel*, 1983].

The next most intense solar flare line is that at 0.511 MeV from the annihilation of positrons. The 0.511 MeV line results from nuclear interactions producing short-lived radionuclei and π^+ mesons, which decay by positron emission.

Present study of gamma-ray lines (2.223 MeV capture and 0.511 MeV annihilation line) and bremsstrahlung continuum observed by the Reuven Ramaty High-Energy Solar Spectroscopic Imager (RHESSI) during the 23 July, 2002 flare has been reported by *Murphy et al.* [2003]; *Share et al.* [2003], and by Yohkoh satellite for flare on 14 July, 2000 by *Yoshimori et al.* [2001, 2003]. The first results from measurements of solar gamma and hard X-ray emissions observed on CORONAS-F satellite have been reported by *Bogomolov et al.* [2003]; *Kuznetsov et al.* [2003]

Gamma-ray bursts are short, typically observable for a few seconds to tens of seconds, and have energies concentrated in the low energy region. Their differential energy spectra have slopes of the order of -1 in the region below 100 keV, and this slope steepens to approximately -2.5 above several hundred keV. The spectra of all observed events are very similar, implying a common production mechanism for these bursts.

The principal processes suggested for producing the gamma-ray continuum in bursts are bremsstrahlung which requires a hot plasma with $T > 10^9$ K, and synchrotron radiation in strong magnetic fields ($\sim 10^{12}$ gauss) by MeV electrons [*Ramaty and Lingenfelter*, 1982].

Chapter 4

CORONAS-I Experiment

4.1 Brief Description

Low altitude satellite CORONAS-I has been devoted to study of various aspects of solar activity [*Kuznetsov et al.*, 1991]. The SOlar Neutron and Gamma rays (SONG) device was a part of the complex measuring high energy electromagnetic and corpuscular emissions from the Sun. The instrument consisted of a large area CsI(Tl) crystal scintillator (20 cm diameter × 10 cm length) viewed by three photomultipliers. The whole scintillator counter was entirely surrounded by a 2 cm thick plastic scintillator anticoincidence shield for charged particles. It was viewed by another three photomultiplier tubes. Neutrons and gamma rays were distinguished according to the shape of the light impulse in the CsI(Tl), which depends on the ionization of the detected particles [*Dmitriev et al.*, 1993]. The low energy gamma quanta were measured in four energy release intervals, $0.12-0.32$, $0.32-1$, $1-3$, and $3-8.3$ MeV, with temporal resolution of 2.5 s. The spectrometer had no collimator and the axis of the spectrometer was parallel to the longitudinal axis of the satellite. More details are given in *Baláž et al.* [1994].

Energetic electron data were acquired with the Monitor Cosmic Ray (MKL - russian acronyms) sensor which measures electrons in the energy range of $0.5-12$ MeV [*Kuznetsov et al.*, 1995]. MKL was oriented in the anti-Sunward direction. The geometric factor was 0.55 cm^2 sr with acceptance angle of ±30°. In this work, two electron channels are used: $0.5-1.5$ MeV and $6-12$ MeV. The temporal resolution of the measurements was 22 s.

The CORONAS-I satellite was launched on March 2, 1994 into a nearly circular orbit at an altitude of 500 km and an inclination of 83°. During its first working period (until July 5, 1994) CORONAS-I satellite was three-axis stabilized and was directed with its longitudinal axis towards the Sun. This was true for both day as well as night passes (SONG was oriented towards the Earth on night side of the orbit). The SONG device was mounted on the platform for the scientific instruments. The platform was placed at a distance of 1 m above the forward end of the satellite. The mass of the spacecraft was 2300 kg. It is cylindrical in shape, approximately 2.3 m in diameter and 5 m high. Extending from the satellite were long-wire antennas and solar panels with a total span of 12.8 m.

4.2 Flux Conversion

The flux for a particular energy E (differential flux) and zenith angle θ is calculated directly from the counting rate by using the efficiency for detection of gamma rays. The count rate $\Delta N/\Delta t$ (counts s^{-1}) in a given energy and angle bin is equal to the incident flux F times the area A of the detector, the efficiency ε, the energy interval ΔE, and the solid angle $\Delta\Omega$:

$$\Delta N/\Delta t = F(E,\theta)\, A\, \varepsilon(E,\theta)\, \Delta E\, \Delta\Omega \tag{4.1}$$

The quantity F has units of photons $(\mathrm{cm}^2\ \mathrm{s\ sr\ MeV})^{-1}$, and ε is a function of energy and angle [*Ryan et al.*, 1977]. Since the detector has nearly an isotropic response, instead of A, the effective area for isotropic flux $G_\circ$ (omnidirectional geometrical factor) have been used, and ε has been considered to be independent of the direction of incidence. The detection efficiency $\varepsilon(E)$, which transforms the photon flux to counting rate, is determined by Monte Carlo method for parallel beam of photons along the detector axis [*Baláž et al.*, 1994]. Absolute efficiency for photo peak events and total interaction for the CsI scintillator versus incident photon energy is given in Fig. 4.1.

The omnidirectional geometrical factor as a 4π projected area of a cylindrical detector of diameter D and height H is calculated using the formula in *Golenetskii et al.* [1971].

$$G_\circ = \frac{\pi D H}{4}\left(1 + \frac{D}{2H}\right) \quad \mathrm{cm}^2, \tag{4.2}$$

which in the case of CsI(Tl) spectrometer is 314 cm^2.

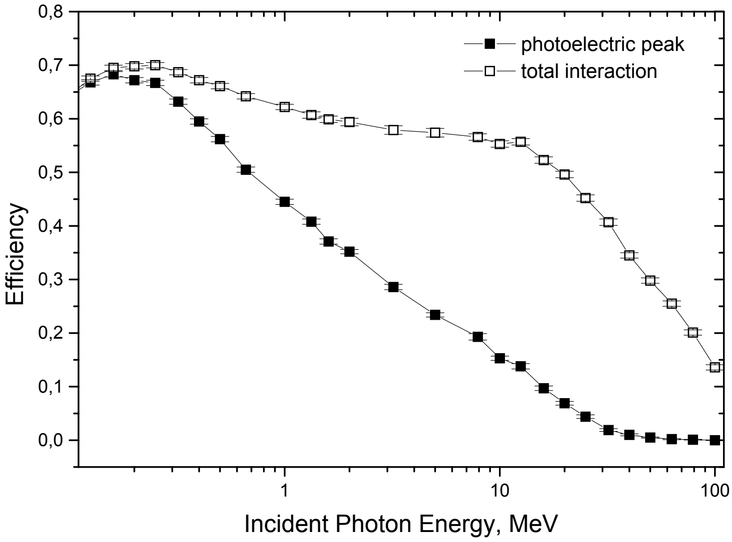

Figure 4.1. Absolute efficiency for photo peak events and total interaction for the CsI scintillator vs incident photon energy. Unlike photons below 200 keV, which lose their total energy in the detector due to the photoelectric effect, low-energy gamma rays in the range 0.3 – 10 MeV interact primarily through Compton scattering and pair production.

The mean efficiency ε of the scintillator has been determined according to

$$\bar{\varepsilon} = \frac{\int_{E_{min}}^{E_{max}} \varepsilon(E) E^{-\chi} \mathrm{d}E}{\int_{E_{min}}^{E_{max}} E^{-\chi} \mathrm{d}E}, \tag{4.3}$$

where $\varepsilon(E)$ is function obtained by polynomial approximation of simulated points in Fig. 4.1 between E_{min} and E_{max} limits. Even if the power law exponent χ varies from 1 to 2, the mean efficiency varies by less than 0.25% in both energy channels. We obtain $\bar{\varepsilon} = 0.693$ for $0.12 - 0.32$ MeV range, and $\bar{\varepsilon} = 0.574$ for $3 - 8.3$ MeV. The conversion from counting rate to flux was made essentially by dividing by $\bar{\varepsilon} G_{\circ}$. This implies that the counting rate contribution to the detector is the same from all directions in 4π solid angle.

The SONG device was primarily designed to measure a solar gamma-ray emission and instrumental setup was arranged in order there was not any shielding matter in direction to the Sun. To follow on gamma radiation produced both in the Earth's atmosphere and local matter, proper evaluation of the unwanted passive shielding in detector field of view becomes very important. Nevertheless, to have a reference values of the detected by SONG device the gamma-ray fluxes per unit solid angle there were used $\Delta\Omega = (2.6 \pm 1.0)\pi$ sr in which gamma rays were assumed to be detected [*Ryumin et al.*, 1996]. In this approximation the SONG placement on instrument panel on CORONAS-I have been considered. Authors also stressed that the solid angle in which the detector is screened by the satellite depends on the energy of the incoming gamma rays. Therefore, the absolute values of the measured gamma-ray intensities are very preliminary and hard to comparable with fluxes in other similar experiments. One obtains that conversion factor $\bar{\varepsilon}G_\circ\Delta\Omega$ is 1777 cm^2 sr for $0.12 - 0.32$ MeV, and 1472 cm^2 sr for $3 - 8.3$ MeV. Note, the gamma-ray mass attenuation coefficient up to energy 10 MeV decreases for most of the construction materials (e.g. for aluminium), therefore uncertainties in determination of the detector field of view (FOV) could be larger for lower energies. In appendix B, according to simplified model of the mass distribution in the CsI environment aboard CORONAS-I satellite, the detector FOV is evaluated.

4.3 Data Presentation

The data set analyzed here was collected over the period from March 1994 through June 1994. The extent of the set is 1.8×10^6 data points with the time resolution of 2.5 s. For the following analysis two (lowest and highest energies) out of four energy channels measuring the gamma rays by SONG instrument have been selected, namely $0.12 - 0.32$ MeV, and $3 - 8.3$ MeV. The data have been split into 180×180 geodetic longitude-latitude bins with the step of 2° in longitude and of 1° in latitude. The average number of points of measurements covering one individual bin is 60. The total data coverage is displayed in Fig. 4.2. The missing data area on north hemisphere is related to regions of data reception. For each of these pixels the population mean and variance has been estimated.

If we have n independent measurements y_i, the consistent and unbiased estimate (est) of population (true) mean μ and variance σ^2 are

$$\mathrm{est}\ \mu = \frac{1}{n}\sum_{i=1}^{n} y_i \equiv \bar{y} \tag{4.4}$$

$$\mathrm{est}\ \sigma^2 = \frac{1}{n-1}\sum_{i=1}^{n}(y_i - \bar{y})^2 \equiv s_{n-1}^2, \tag{4.5}$$

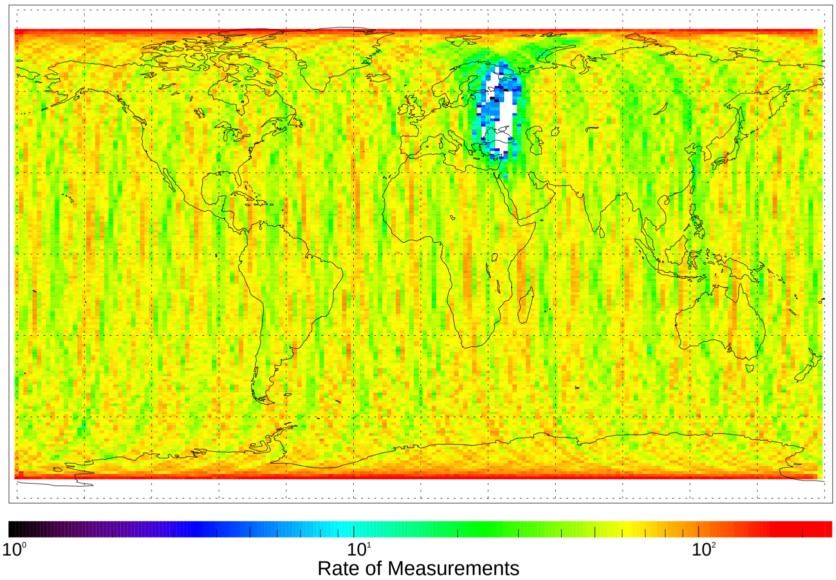

Figure 4.2. The map of covering of measurements by SONG device in individual bins [from *Bučík et al.*, 2000].

regardless of probability distribution followed by y. Note, consistent estimate converges to the true value, and mean of an unbiased estimate equals true value. It should be noted this is the zero approach suitable for a rough description of the measurement points to obtain primarily a qualitative picture. The detector counts per second are usually distributed as a Poisson distribution. However, when the number of counts is large the Poisson distribution converges a Gaussian. The Pearson's χ^2 test of normality of distributions did not confirm unambigously for each pixel the normality of the distribution. There are various possible effects influencing the inhomogeneity of the distribution, namely a- the temporal variability, especially at high latitudes due to the variations in flux of high energy electrons precipitating into the atmosphere, b- the changes in the orientation of the detector in given pixel with respect to magnetic field, in course of satellite northward and southward passes and due to slowly variable detector orientation in different magnetic local time sectors, and c- changes in zenith angle orientation of detector axis in different local time sectors.

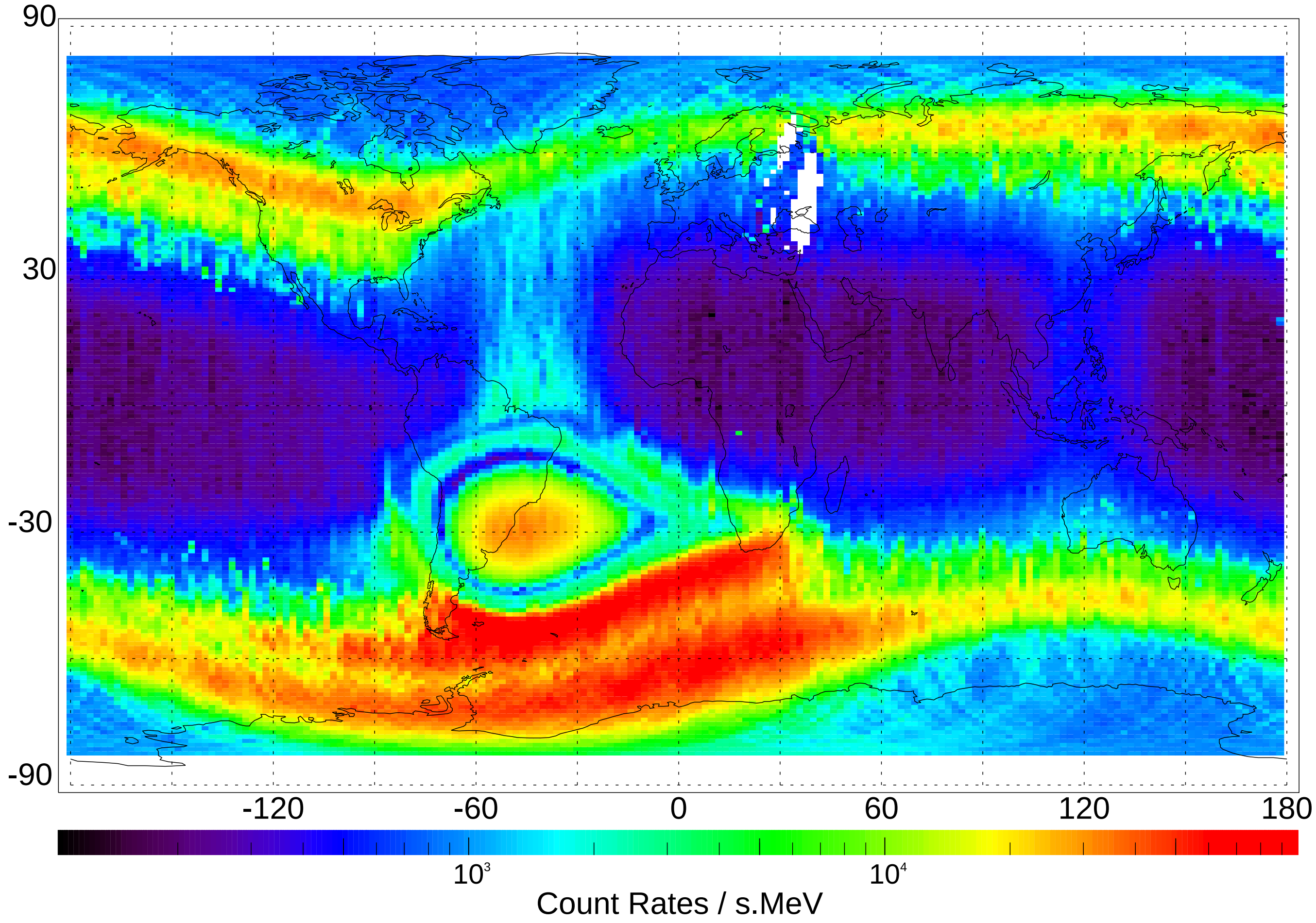

Figure 4.3. The map of average gamma-ray fluxes in energy range 0.12 – 0.32 MeV. Numerals, which denote vertical (latitude) and horizontal (longitude) axes of geographic map are in degrees. Colored scale matches the log of the counts [from *Bučík et al.*, 2000].

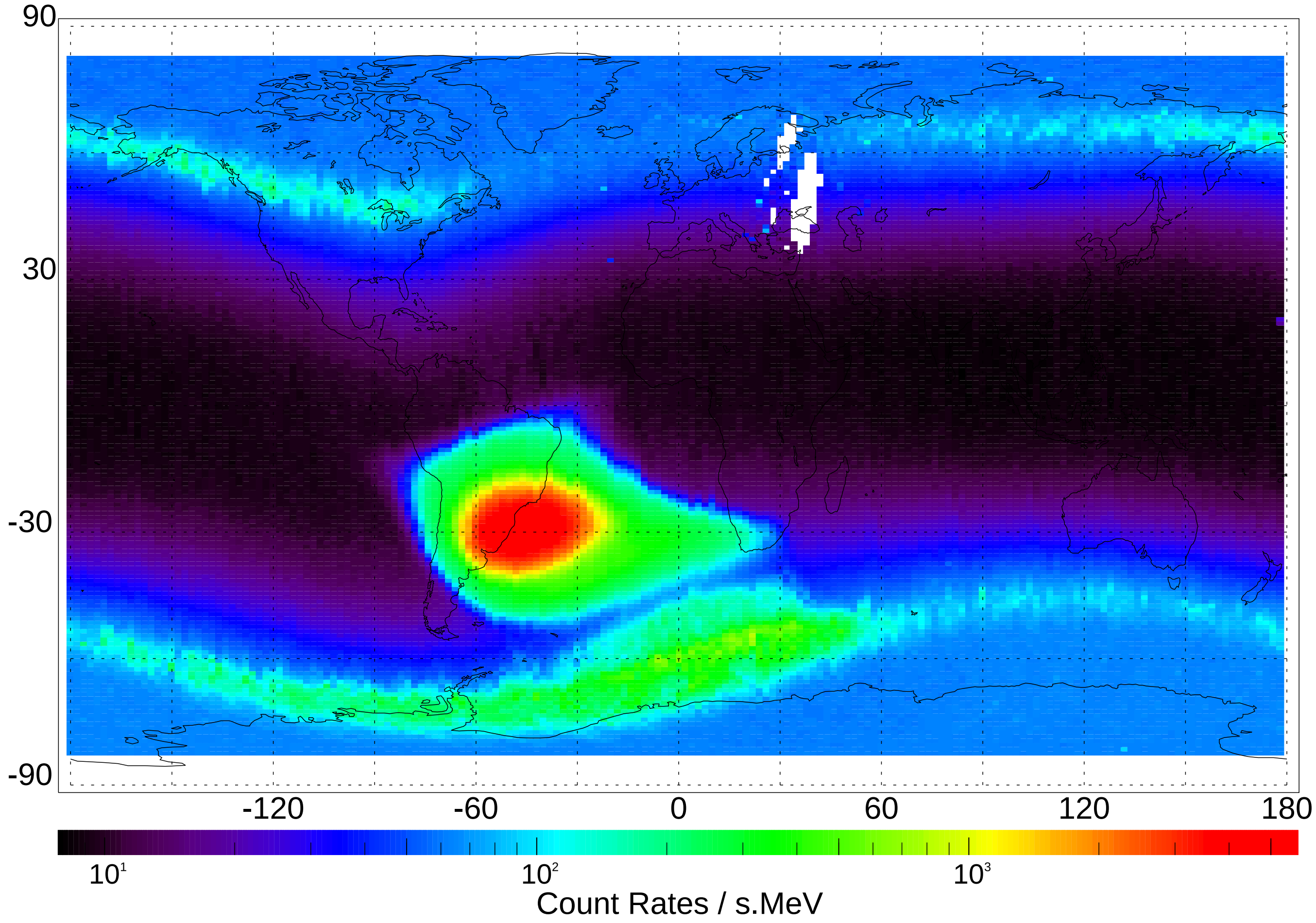

Figure 4.4. The map of average gamma-ray fluxes in energy range $3-8.3$ MeV. Numerals, which denote vertical (latitude) and horizontal (longitude) axes of geographic map are in degrees. Colored scale matches the log of the counts [from *Bučík et al.*, 2000].

The geographic maps at CORONAS-I altitude of low and high-energy gamma-ray distributions are shown in Fig. 4.3 and 4.4, respectively. Even using these large-scale figures, two important features of gamma radiation are prominent: (1) The irregular gamma-ray increases in auroral and subauroral zones, more pronounced in $0.12 - 0.32$ MeV range. (2) Monotonously variable lower flux along the latitude, seen better for higher energies. We assume the more intense component is connected with trapped and quasi-trapped high-energy particles, whereas weaker one is related to primary cosmic rays. Both components of measured gamma radiation are discussed separately.

Our geographical maps are very close to the geographical distribution of $0.19 - 3.2$ MeV electron intensity in altitude ranges $350 - 500$ km during the 12 month period from February of 1984 on Ohzora satellite [*Nagata et al.*, 1987]. Authors stressed that the intense electron region observed in the SAA is clearly separated from the auroral region in altitude range $350 - 850$ km contrary to proton one.

To our knowledge no detailed distribution of gamma-ray flux at energies studied here was reported earlier in literature.

Chapter 5

Gamma-Ray Flux Related to Primary Cosmic Rays

This feature of gamma radiation is investigated for high gamma-ray energies because in the energy interval $0.12 - 0.32$ MeV the studied effect is small as can be seen in Fig. 4.3. The obtained picture in Fig. 4.4 should be assumed to be the combination of the atmospheric gamma rays with any contribution of local photonic gamma radiation and of diffuse gamma-ray having no latitudinal dependence.

5.1 Diffuse Counting Rate

The representations of the spectral emissions, given by eqn. 3.6 and 3.7, have been used to estimate the contribution of the cosmic diffuse flux to the overall detected radiation in energy ranges $0.12 - 0.32$ MeV and $3 - 8.3$ MeV respectively. Diffuse counting rate has been obtained by folding the instrument detection efficiency into the above mentioned fits. The detector response due to diffuse gamma rays in $3 - 8.3$ MeV energy range has value of $\sim 4.76 \times 10^{-4}$ counts $(\mathrm{cm}^2\ \mathrm{s\ sr})^{-1}$ which presents about 1.5% of the overall gamma-ray flux measured near the equator and 0.2% at the pole.

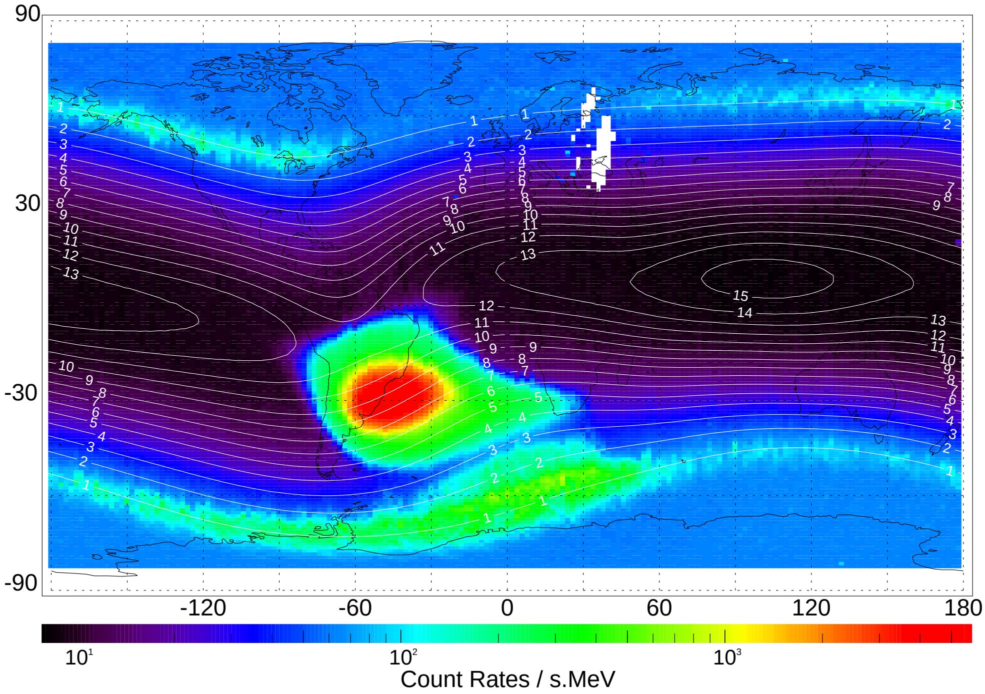

Figure 5.1. The distribution of $3 - 8.3$ MeV gamma rays at geographic map. Contours of vertical cutoff rigidities as calculated for epoch 1994.3 at altitude of 500 km. The contours are in units of GV.

5.2 Latitudinal Dependence

In low-energy region the primary particles are influenced by the geomagnetic field, which they must penetrate to reach the top of the atmosphere. A particle's penetrating ability is determined by its momentum per unit charge, a quantity called magnetic rigidity $R = pc/Ze$. Notice, momentum in GeV/c (in the ultrarelativistic limit this would also be the total energy in GeV) is equal to rigidity in GV for a single-charge particle. At a given point in the magnetosphere and in the given direction only the particles that have rigidities higher than a certain (cutoff) value are able to arrive to the specified point. The modulation of the primary cosmic rays by the geomagnetic field should result in cutoff rigidity dependence of any secondary products.

Fig. 5.1 illustrates the relation of the second measured component of high-energy gamma rays on CORONAS-I to the vertical cutoff rigidity, i.e. virtually on the primary cosmic-

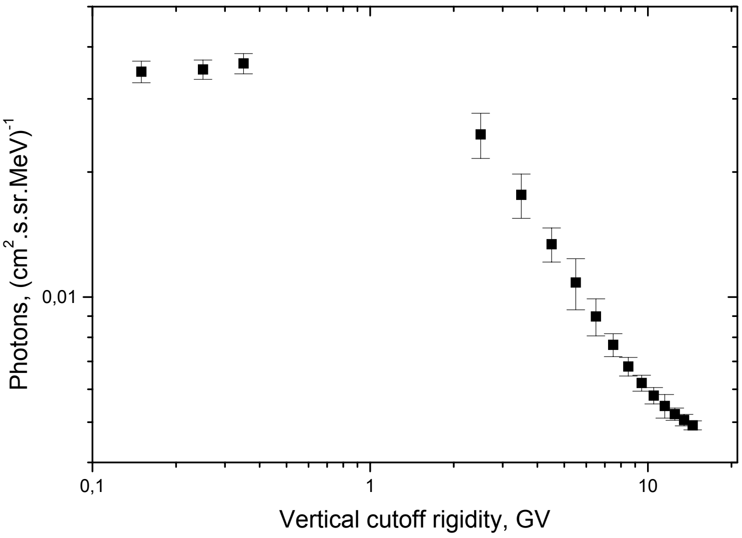

Figure 5.2. Dependence of 3−8.3 MeV gamma-ray flux on threshold rigidity of measurement point in vertical direction. The estimates of standard deviations are indicated by error bars [from *Bučík et al.*, 2000].

ray flux at the point of measurements. The cosmic-ray vertical cutoff rigidity (threshold value of magnetic rigidity in vertical direction) is computed as $R_c = 14.9/L^2$ (GV), the approximation of the formula (5) in the paper *Shea et al.* [1987]. McIlwain's L parameter is convenient to use on the basis that L is highly correlated with vertical cutoff rigidities for cosmic-ray particle entry. The increase of gamma-ray flux as cosmic-ray cutoff decreases, indicates its genetic relationship with cosmic-ray primaries. At $R < 1$ GV the $3 - 8.3$ MeV gamma-ray flux remains on the same level - rises a saturation value. This clearly indicates the cutoff to the differential energy spectrum of primary cosmic rays, which appears at kinetic energies $E \leq 1$ GeV per nucleon. From this simply follows there is no essential flux of cosmic-ray protons with energy < 1 GeV at top of the Earth's atmosphere, which would contribute to production of the secondary gamma rays.

Excluding the effects of trapped and quasi-trapped particles, the latitudinal[1] distribution

---

[1] The commonly used term 'latitudinal' follows from the known cutoff rigidity dependence on geomagnetic latitude (cutoff rigidity monotonousły increases as the geomagnetic latitude decreases).

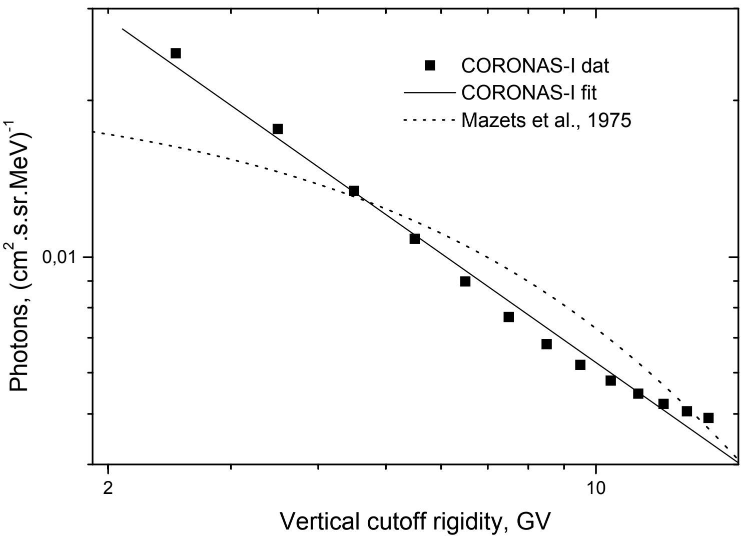

Figure 5.3. Our power law approximation and eqn. 3.3 are shown.

(i.e. variation of the flux with vertical cutoff rigidity R_c of the measurement point) of gamma rays in $3-8.3$ MeV channel has been obtained. It is displayed in Fig. 5.2. The region of the South Atlantic Anomaly was not included owing to the presence of gamma rays from the trapped radiation. The region near the plateau is not represented owing to the presence of outer radiation belt electrons at all longitudes.

The width of the rigidity intervals was 1 GV between 2 GV and 15 GV, and 0.1 GV between 0.1 and 0.4 GV, and an average number of measurements was $\sim$ 1040 records. The uncertainties presented in the figure by error bars are primarily determined by the dependence of the count rates on the longitude. For $R > 2$ GV the power spectrum fit of the latitudinal dependence $R^{-\gamma}$, with index $\gamma = 0.94 \pm 0.03$ determined by least squares method (see appendix A). The coefficient of determination r^2 equals 0.988, very close to unity, and the estimate of the σ equals 0.026. Indeed, the real spectrum can differ (could be softer) in some degree from computed one due to fact that fluxes are fitted in the middles of rigidity intervals. To take the middle value is proper if the spectrum has normal or uniform distribution in the particular interval. However, this is not the case, the spectrum would

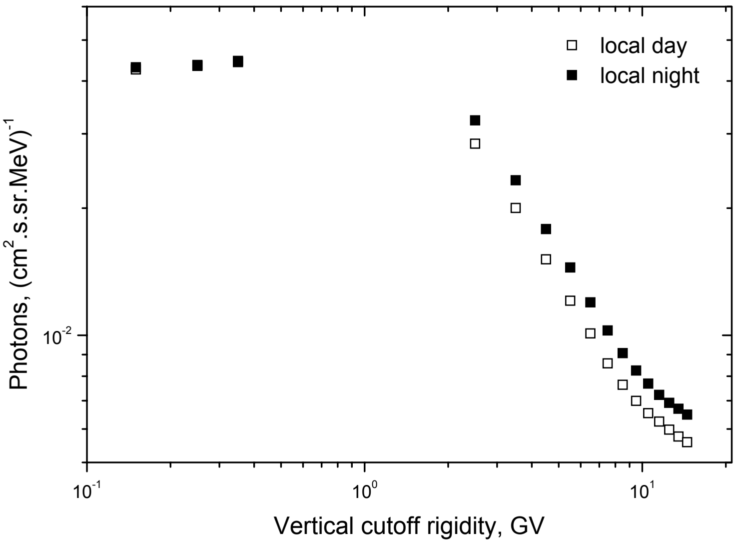

Figure 5.4. Dependence of 3-8.3 MeV gamma-ray flux on vertical cutoff rigidity for local day and local night [from *Bučík et al.*, 1999a].

have a power dependence.

The integral rigidity power law spectral index of primary cosmic rays, which is about -1.7 [e.g. *Beliaev et al.*, 1996] should be close to our value on the assumption that gamma-ray flux is proportional to the flux of charged cosmic-ray particles incident on the earth's atmosphere [*Golenetskii et al.*, 1971].

The flattening of the rigidity spectrum at low latitudes may partly reflect the non-applicability of the L parameter near the equator due to difference between the minimum L equator and cosmic-ray equator.

Note that gamma-ray dependence on magnetic rigidity would be decreased by somewhat contribution from reentrant albedo electrons, which can have rigidities below that of the geomagnetic cutoff value, and enhance the gamma-ray flux at low latitudes.

The ratio of polar to equatorial flux has a value of ~ 7, and ratio at 3.5 GV and 14.5 GV is ~ 3.6. These ratios are comparable with others earlier experiments at different altitudes and energies. The latitudinal profile is in good agreement with calculations assuming their production in the atmosphere. The polar - equatorial ratio of the total gamma-ray flux

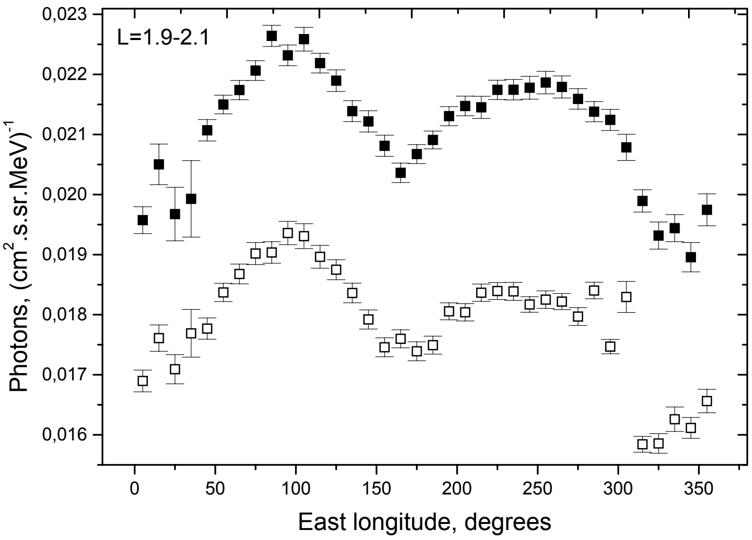

Figure 5.5. The longitudinal variations of $3 - 8.3$ MeV gamma-ray flux at $L = 1.9 - 2.1$ for local night (solid squares) and local day (open). 1σ statistical error bars are also indicated [from *Bučík et al.*, 2002a].

between 8.3 and 116 MeV detected by SONG device during single orbit in April 1995 is about 8 ± 2 [*Ryumin et al.*, 1996].

Since conditions of atmospheric gamma-ray observations on night side of the CORONAS-I orbit are significantly better due satellite solar orientation, the latitudinal dependences are given separately for the local times $10 - 14$ h (local day), and $22 - 02$ h (local night). During the time period March-June, 1994, the CORONAS-I's orbit passed through all local time sectors. For example, at beginning of April, 1994 the satellite orbit was in noon-midnight meridian with consecutive orbit precession to dawn-dusk plane in mid-May, 1994. Fig. 5.4 depicts the latitudinal dependences of detected gamma-ray flux for local day and for local night. From this figure is clear that at equal latitudes (geomagnetic thresholds) the measured flux on the night side is somewhat higher than detected one on the day side of the orbit. The night-day fluxes ratio varies from 1.23 in the equatorial region up to 1.33 on the intermediate latitudes. The differences between both night and day fluxes seem to be larger than only possible experimental deviations.

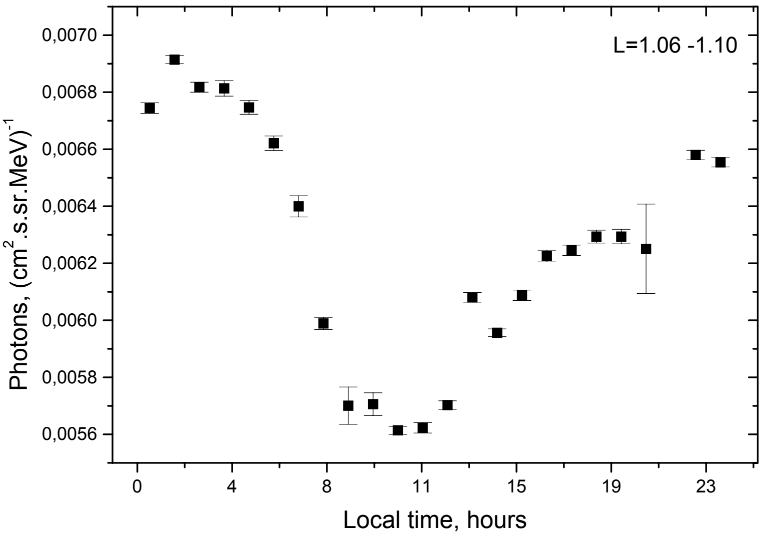

Figure 5.6. Gamma-ray flux in energy range $3 - 8.3$ MeV vs local time at $L = 1.06 - 1.1$. 1σ statistical error bars are also indicated [from *Bučík et al.*, 2002a].

5.3 Longitudinal and Local Time Variations

Due to azimuthal asymmetry in the real geomagnetic field the flux variation of secondary components on longitude is expected. The longitudinal dependence of gamma rays at various latitudes we search in the following seven L intervals: $1.06 - 1.1$, $1.1 - 1.3$, $1.3 - 1.7$, $1.7 - 1.9$, $1.9 - 2.1$, $2.1 - 2.5$, and $2.5 - 3$. Illustration of the gamma-ray longitudinal variation at $L = 1.9 - 2.1$ where the flux was found to be dependend on longitude in maximal degree is given in Fig. 5.5. This dependence is significantly weaker near the equator. The ratio between maximum and minimum flux values is about 1.2 in this L range and fall to 1.1 at other latitudes. These dependeces are very similar those obtained by *Kuznetsov et al.* [1997] for charged energetic particles (protons with $E_p > 70$ MeV, and electrons with $E_e > 55$ MeV). Their dependence is approximately about factor 2 larger in the range $L = 1.9 - 2.1$, if as a measure of strength of the dependence is considered the above mentioned ratio.

To have a better insight how flux varies with local time we inspect local time dependence in above L ranges. As a example, Fig. 5.6 shows the $3 - 8.3$ MeV gamma-ray flux versus local time near the equator $L = 1.06 - 1.1$, where variations of gamma-ray flux on longitude are minimal. Importance of the local time dependence follows from the fact that the contribution of atmospheric and local gamma radiation changes during various local times. The changes in local gamma-ray production seem to be stronger due to variation satellite orientation relate to impinging cosmic-ray protons (e.g. east-west asymmetry effect). Unfortunately we have no information about orientation of CORONAS-I axes, those perpendicular to its longitudinal axis and cannot use obtained results to evaluate the fluxes of atmospheric and local gamma rays.

The biggest contribution of the atmospheric gamma rays is expected at the local night - longitudinal axis is almost directed toward the atmosphere, and the smallest in noon mainly due to screening of the SONG instrument from atmospheric gamma rays by the satellite body. During the local dawn ($\sim$ 6 h) and dusk ($\sim$ 18 h) the contribution from atmosphere could also vary with satellite orientation, probably not so strong as in case of local radiation. However, fluxes on 6 h and 18 h seem to be in the limits of the experimental deviations.

Next, we attempt to evaluate the satellite body shielding effect. One can find that the acceptance angle of our cylindrical detector (considering only geometric effect) for blocking one of its bases, equal to 3 π sr. It is easily obtained using the eqn. B.6 in appendix B for the centre of the cylinder. The similar situation occurs at the local night or at the local day of the satellite orbit, where the atmospheric gamma radiation can be roughly received from all sides except one cylinder base which is actually averted from the Earth's atmosphere. At the local day, due to fixed satellite solar orientation the obtained acceptance angle is reduced about factor of 0.5 π sr (see Tab. B.6 in appendix B) due to satellite body screening. The ratio of the night-day acceptance angles is very close to the observed night-day flux ratio.

5.4 Charged Particle Flux Map

For comparison, the map of the overall flux of energetic charged particles - protons ($E_p > 70$ MeV) and electrons ($E_e > 55$ MeV) detected by the same instrument and during the same time period is given in Fig. 5.7. Fluxes measured at the center of SAA (empty area) were below the minimum observable value outside this region, and hence were not displayed.

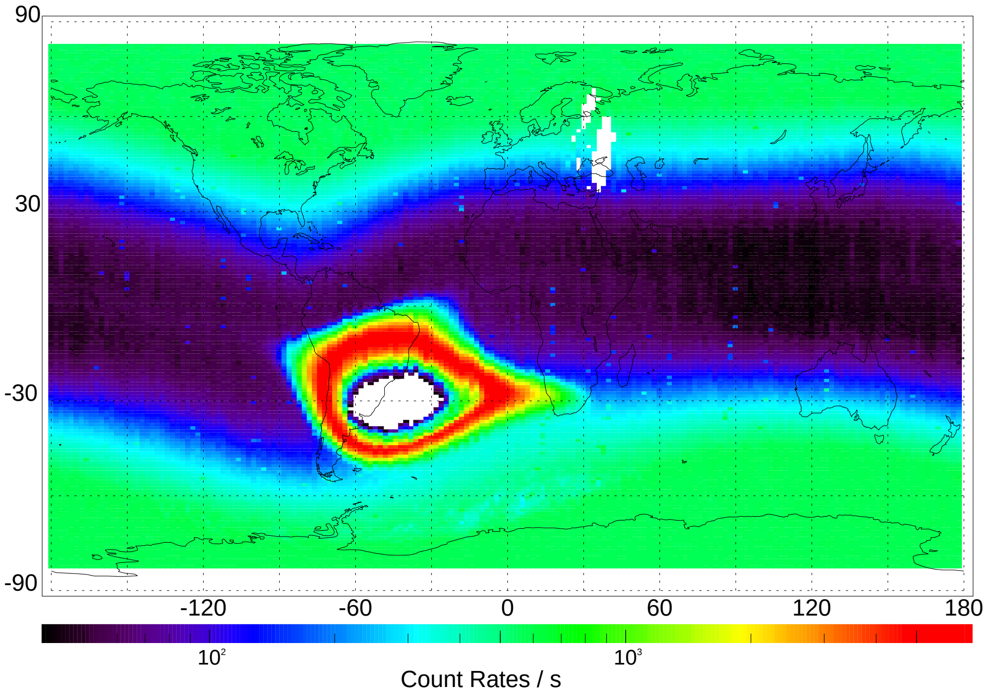

Figure 5.7. The geographic map of average fluxes of protons with energy $>$ 70 MeV and electrons with energy $>$ 50 MeV measured during four-month period in the spring of 1994 by the SONG device on CORONAS-I. The geometric factor for detection of charged particle flux is about 2000 cm^2 sr [from *Kuznetsov et al.*, 2002b].

Extremely low flux in the center of SAA is due to saturation effects of the SONG instrument. Similar rigidity pattern, even more visible at low latitudes, is evident for charged particles.

5.4.1 Energetic Charged Particle Flux: Composition and Short-Term Variations

Energetic charged particle fluxes (out of radiation belts) at satellite altitudes were investigated in several earlier experiments (e.g. Intercosmos -17). They reveal that the measured particle fluxes exceed primary cosmic-ray flux at all L values. The additional flux consists of the atmospheric albedo due to interactions of primary cosmic rays with residual atmosphere and upward flowing of its part, and of the secondary particle flux produced in satellite and detector material.

The rigidity spectrum of primary cosmic rays was taken from *Beliaev et al.* [1996]. If the

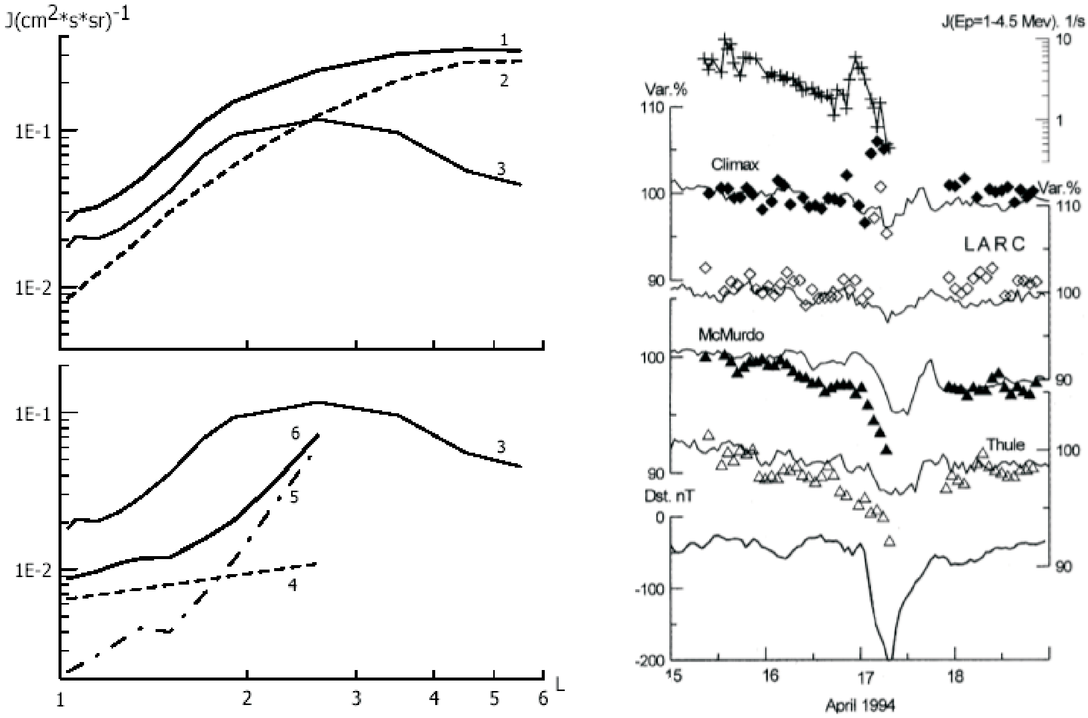

Figure 5.8. (*left*) L - dependence of particle fluxes (see text) [from *Kuznetsov et al.*, 2001]. (*right*) The SONG instrument's count rate obtained in the polar caps (triangles) and at the middle latitudes (diamonds) in North (open) and South (closed) hemispheres and NM data for April 15 – 19, 1994. At the bottom the D_{st} index (in nT) is shown. Magnetic storm is indicated by large negative excursion of D_{st} [from *Kuznetsov et al.*, 2002b].

integral rigidity spectrum is in the form $I_{CR} \sim R^{-1.7}$, the flux dependence upon Mclwain's L parameter takes form $I_{CR} \sim L^{3.4}$. Left top panel in Fig. 5.8 shows the intensity of charged particle fluxes measured by the SONG device, curve -1, and primary cosmic rays, curve -2. We observe similar L-dependence in the $1.2 < L < 1.8$ range. The difference between them - fluxes of atmospheric albedo and local particles, is displayed by curve -3 in both panels. An albedo flux is proportional to the primary cosmic-ray one in this L-interval. We see the contribution of albedo particles to the detector count rate depends on the latitude (or on the L value). Maximum albedo deposit relatively to primary cosmic-ray fluxes was observed near the geomagnetic equator (approximately 80% of the total measured flux) and minimum at high latitudes. Illustration of the electron flux with $E > 65$ MeV, curve -4, and proton albedo flux with $E > 500$ MeV, curve -5, and sum of proton and electron albedo fluxes, curve -6, according to Cosmos-1870 [*Abramenko et al.*, 1990] and Intercosmos-17 [*Efimov et al.*, 1985] data is shown on the bottom of the left part of Fig. 5.8.

Analysis of the short-term variations (named as Forbush effects) of charged particle flux on CORONAS-I makes relatively independent part of the present work. Apparently there would be probably right to expect gamma-ray variations connected with this type of cosmic-ray fluctuations. Notice, some literature evidence about long-term (11-year) gamma-ray variability related to the solar cycle variations has been previously mentioned (see sec. 3.1.1).

The intensity variations of primary-cosmic rays, which are caused by changes in the interplanetary medium conditions, provide information on traveling complex plasma structures in the heliosphere and their interference with energetic charged particles and Earth's magnetosphere. Forbush effects are sudden decreases of cosmic-ray intensity followed by a gradual recovery during several days -weeks. Forbush decreases are due to interplanetary shocks passing the Earth's orbit producing an effective barrier shielding cosmic-ray particles.

Cosmic-ray variations induced by solar activity are traditionally investigated using the ground-based Neutron Monitor (NM) network. However, the possibility to study the same variations by detectors with large geometric factors on board near Earth high-inclination satellite has been recently turned out, using the advantage of a single detector scanning particle variability at various latitudes during one orbit [e.g. *Bogomolov et al.*, 1995].

The intensity variations on CORONAS-I are discussed during magnetic storm on April $2-3$, 1994 (designated as Event 1, the peak $K_p = 6+$, $7+$; $D_{st} = -103$ nT, -111 nT) and stronger one beginning on April 17, 1994 (designated as Event 2, the peak $K_p = 8+$; $D_{st} = -201$ nT). Both events were observed by SONG instrument in channel measuring the fluxes of protons with energy > 70 MeV and electrons > 55 MeV, and preliminary analyzed by *Kuznetsov et al.* [1999].

Fig. 5.8 (right) shows time dependence of SONG instrument's count rate obtained in the polar caps and at middle latitudes in North and South hemispheres around the Event 2. The NM data for polar McMurdo and Thule NMs, and for mid-latitude Climax and LARC NMs are also displayed. At middle latitudes, the cosmic-ray intensity measured by SONG instrument is not corresponding to the profile measured at two mid-latitude NMs

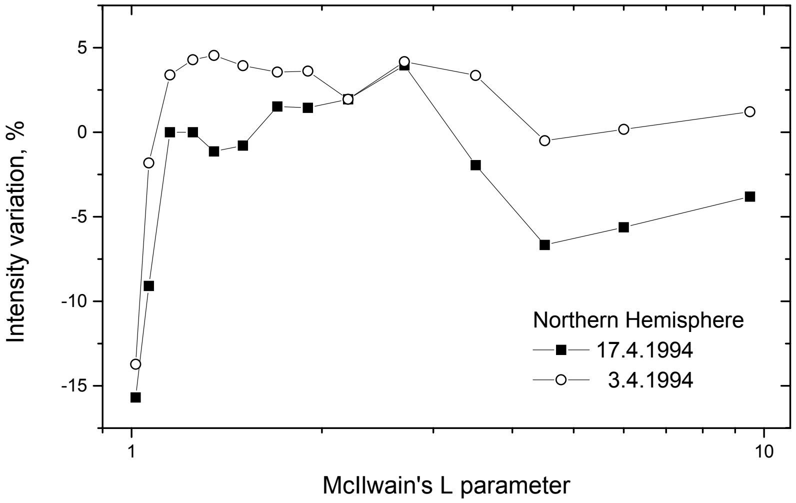

Figure 5.9. The intensity variation of charged particle flux (protons with energy > 70 MeV and electrons > 55 MeV) on L during the Forbush events on April 17, 1994, and on April 3, 1994 at Northern hemisphere [from *Bučík et al.*, 2001].

with $R_c \sim 3$ GV, instead, increases at the same latitude (however at different longitudes) are detected at initial phase of the magnetic storm. The SONG instrument data profiles in polar caps are similar to those observed by polar NMs; the significant decrease of the instrument's count rate on April 17 is observed.

To study more carefully the latitude dependence of these effects, the SONG data were binned into the fourteen bins in L parameter: $1 - 1.03 - 1.1 - 1.2 - 1.3 - 1.4 - 1.6 - 1.8 - 2 - 2.4 - 3 - 4 - 5 - 7 - 12$, and distinguished into the Southern and Northern hemisphere according to the minimum L equator on altitude 500 km. The data measured over the period from April 6 to April, 16, 1994, we use for mean background count rate N_b (the average K_p value was 4+).

The intensity variation $(N_e - N_b)/N_b$ of the SONG charged particle flux, where N_e is a mean count rate in event day, versus L for both events at the North and South hemispheres are shown in Fig. 5.9 and Fig. 5.10, respectively. These profiles should reflect the following three effects: (a) - the variations in Forbush decreases with latitude, (b) - changes in cutoff rigidity, and (c) - latitude dependence of charged albedo flux contribution. Relative slow changes in flux decrease (along L) at $L > 4.5$ are probably due to weak changes in cutoff rigidity during storm time at these L's, and that the Forbush decrease of primary cosmic rays stands further on the constant level at high latitudes. Note, there is observed plateau in latitude dependence of the integral charged particle flux (see fig. 5.8) above $L \sim 4$. From this follows that Forbush decrease should be most pronounced at high latitudes (near the plateau), and for the Event 2 achieves at least value of 6%. The increase in count rate at middle latitudes ($L \sim 2 - 3$) can be probably related to the maximum decrease of the corresponding geomagnetic cutoff.

Similar results about cutoff rigidity variations (the weak change at high latitudes and near equator, and maximum variations at the middle latitudes) one can find from *Smart et al.* [1999] calculations for altitude of 450 km. *Flückiger et al.* [1980] showed that during the initial phase of geomagnetic storm ($Dst \sim -100$ nT) cutoff rigidity variations reached $\sim 15\%$ between 2 and 3 GV. Similar results on rigidity cutoff variations were reported by *Lockwood and Webber* [1991]. Such variations of the geomagnetic cutoff, caused by the ring current development, could have led to the enhancement of the cosmic-ray flux detected by SONG instrument.

As can be seen from both Fig. 5.9 and Fig. 5.10, near-equatorial region is characterised by the strong depression of the SONG detected charged particle flux, instead of the weak Forbush decrease. Since maximum albedo deposit relatively to primary cosmic rays was observed near the geomagnetic equator, we suppose that in fact we observe the decrease in flux of particles, which have rigidity below the local geomagnetic cutoff, and therefore could be strongly affected by the fluctuations in the interplanetary magnetic field.

5.5 Induced Contribution

Our observations in $0.12 - 0.32$ MeV energy channel indicate that the detector counting rate was abnormally high (~ 20 times) for about 5 min after the satellite had passed through the anomaly. Radiation enhanced zone on the opposite hemisphere at $\sim 120°$ of longitude indicate the flux was considerably above the gamma-ray albedo level during at least 50 min after a radiation belt anomaly passage (probably until another anomaly passage in the next

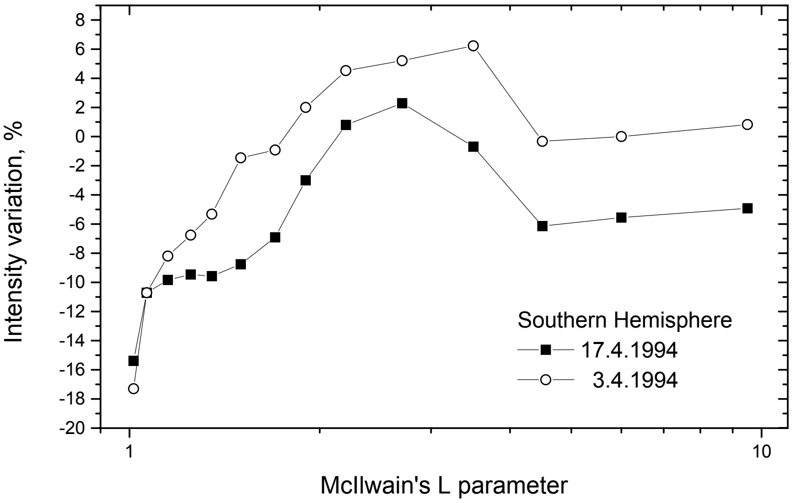

Figure 5.10. The intensity variation of charged particle flux (protons with energy > 70 MeV and electrons > 55 MeV) on L during the Forbush events on April 17, 1994, and on April 3, 1994 at Southern hemisphere [from *Bučík et al.*, 2001].

orbit). The same effect was observed by NaI(Tl) scintillation counter in two energy regions: 0.3 – 1 MeV and 1 – 3 MeV on OSO-1, the first satellite gamma-ray experiment in the nuclear line region [*Chupp*, 1976, and references therein].

There is no evidence for induced radiation presence between 3 MeV and 8.3 MeV although the greatest contribution in 3 – 8.3 MeV channel comes from 3 MeV gamma rays. This supports measurements by low energy gamma-ray telescopes obtained in SMM and CGRO missions, that spallation contributes mostly to energies below 3 MeV.

5.5.1 Estimation of the Cosmic-Ray Proton Induced Radiation

Induced contribution in the energy range 0.12 – 0.32 MeV has been evaluated by comparison of the latitudinal dependeces in two discussed energy channels (*I. N. Myagkova and A. V. Bogomolov,* personal communications, 1997). The reason is that in the raw data there are observed different latitudinal profiles for low and high gamma-ray energies at SONG device. The following assumptions have been considered: there is no induced radiation in

	Flux, ph $(\mathrm{cm}^2\ \mathrm{s\ sr\ MeV})^{-1}$	
Energy, MeV	Geomag. Equator	Polar Region
$0.12 - 0.32$	$(1.3 \pm 0.6) \times 10^{-1}$	$(4 \pm 1.2) \times 10^{-1}$
$0.32 - 1$	$(7.9 \pm 5.9) \times 10^{-2}$	$(1.74 \pm 0.59) \times 10^{-1}$
$1 - 3$	$(2.2 \pm 1.4) \times 10^{-2}$	$(9.5 \pm 1.4) \times 10^{-2}$
$3 - 8.3$	$(6.04 \pm 0.01) \times 10^{-3}$	$(4.29 \pm 0.01) \times 10^{-2}$

Table 5.1. Measured gamma-ray fluxes in the equatorial and polar region [from *Bučík et al.*, 2002a].

$3 - 8.3$ MeV range, i.e. all gamma rays have albedo origin; overall gamma-ray flux (N) in $0.12 - 0.32$ MeV range is due to induced (I) and albedo (A) one; the induced component has no latitudinal dependence - many spallation products may have half-lives great than CORONAS-I orbital period of $\sim$ 90 min; and the latitudinal effect of albedo gamma rays between 120 keV and 8.3 MeV is independent on energy - approximately same latitudinal dependences were observed in the three energy channels $3 - 8.3$, $8.3 - 16$, $16 - 29$ MeV during couple of orbits in April 1995 on CORONAS-I [*Bogomolov et al.*, 1998b].

By solving of the system of equations $I + A = N_{\mathrm{equator}}$, $I + r\,A = A_{\mathrm{pole}}$, where r is the ratio of the counts at the pole and at the equator in $3 - 8.3$ MeV energy range, the induced component between 0.12 and 0.32 MeV presents about 310 counts/s, which is 82% of total measured flux at geomagnetic equator and 53% at the pole. The induced contribution was subtracted as a constant simply from the detected gamma-ray flux. The result is already seen in Fig. 4.3.

5.6 Gamma-Ray Energy Spectra

Background gamma-ray spectra detected by OSSE instrument on CGRO [*Johnson et al.*, 1993], which are mainly due to induced radioactivity, and results of *Truscott et al.* [1995] calculations of photon energy spectra of radioactive isotopes emission produced in CsI and NaI crystals in near -Earth space have been used for correction of the measured fluxes also in

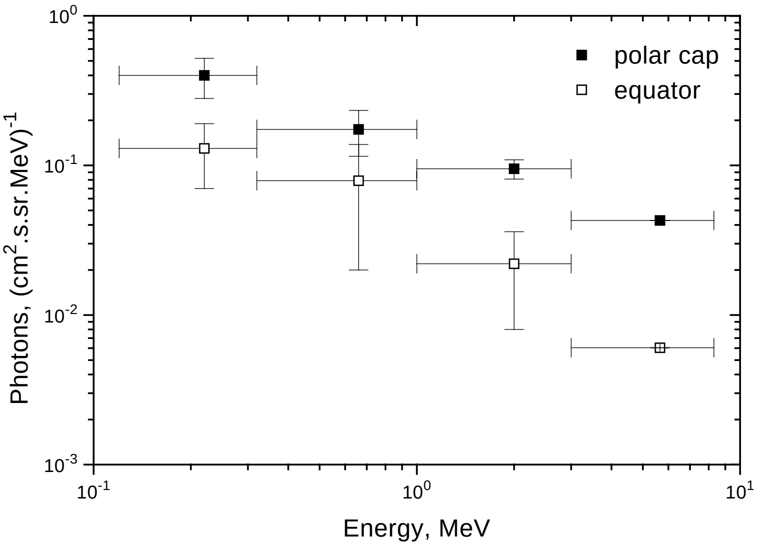

Figure 5.11. The differential gamma-ray energy spectra near the geomagnetic equator and in the polar region. 1σ statistical error bars are indicated for the middle of energy intervals [from *Bučík et al.*, 2002a].

the energy channels 0.32−1 MeV and 1−3 MeV. In the energy range of 0.32−3 MeV, induced radioactivity determines about 74% of total measured flux near the geomagnetic equator and about 47% in polar caps (*S. P. Ryumin*, personal communications, 1999). Since the latitudinal dependence of the induced gamma-ray flux practically absent [*Dean et al.*, 1991], the induced contribution was simply subtracted as a constant from the detected gamma - ray flux. Preliminary differential energy spectra after corrections for induced background in energy range 0.12 – 3 MeV are given in Fig. 5.11 for both equatorial and polar region. Corresponding differential fluxes are indicated in Tab. 5.1.

Considering the intervals for the highest and the lowest energies, the rough estimate of the spectral index χ of the power law dependence $E^{-\chi}$ may be done by

$$\chi = \frac{\log \frac{I_1}{I_2}}{\log \frac{E_2}{E_1}}, \tag{5.1}$$

where I_1, and I_2 are differential fluxes in 0.12 – 0.32 MeV and 3 – 8.3 MeV ranges, respectively, and E_1, E_2 corresponding energy midpoints. The obtained values of spectral indices are $\sim 1.$ at the equator and ~ 0.7 at the pole. The obtained spectra are rather hard than observed ones, especially at polar region. Similar tendency for higher energies (i.e. somewhat harder spectrum at high latitudes than at lower) was reported by *Bogomolov et al.* [1998b] using the single orbit SONG data in April 1995 in range of $8.3 - 116$ MeV. The power law spectral index was found to be equal to 1.1 ± 0.3 through the all latitudes [*Ryumin et al.*, 1996]. The softer energy spectrum at magnetic equator may be partly explained by contribution of the re-entrant electrons on closed filed lines at low latitudes.

Chapter 6

Gamma Rays Associated With Trapped Particles

The population of charged particles stably trapped by the Earth's magnetic field consists mainly of protons with energies between 100 keV and several hundred MeV and electrons with energies between a few tens of keV and 10 MeV. The maximum integral flux of protons above 100 keV occurs at $L \sim 3.1$. The energetic electrons occur throughout the Earth's trapping region. The electron population above 1 MeV is characterized by two zones of high intensities, below $L \sim 2$ and above $L \sim 3$, respectively, which are separated by a region of low intensities, called the slot region [*Walt*, 1994].

6.1 Gamma Rays in $L - B$ Coordinates

The most used coordinate system for particle flux mapping is $L - B$ coordinate system based on the trapped particle motion, introduced by *McIlwain* [1961]. Remind the points in $L - B$ diagram present different drift shells, determined by the actual magnetic L-shell and by mirror point field value B. Therefore, $L - B$ space maps fluxes at mirror points, i.e. fluxes perpendicular to the magnetic field strength. The B dependence in $L - B$ coordinates reflects pitch angle distribution. This is not the case when we map omnidirectional particle fluxes. Interpretation and significance of the omnidirectional mapping in $L - B$ diagram in symmetric or nearly symmetric fields (as in the magnetosphere below $L \sim 6$) have been

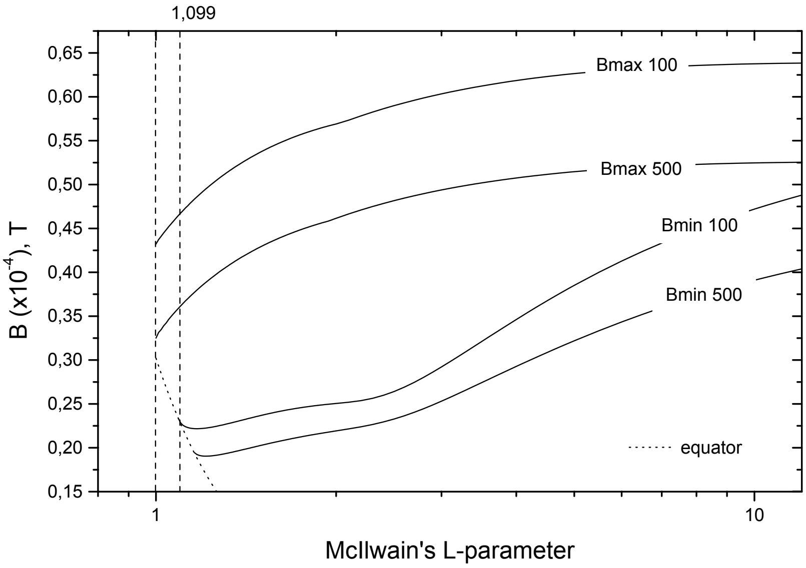

Figure 6.1. The levels of 100 and 500 km altitudes in $L-B$ space. The L, B coordinates are determined by International geomagnetic Reference Field (IGRF) model 1990 extrapolated to the time of observation. No external fields are included. The curves of the minimum and maximum magnetic field strength at 100 (500) km are marked by Bmin 100 (500) and Bmax 100 (500) for L shells starting from unity. The dotted curve presents dipole magnetic equator. Two vertical lines at L equals 1 and 1.099 are also displayed. The significance of the last one is later discussed. Note that owing non-dipolar nature of the Earth's magnetic field, L-values a bit less than 1.0 are also possible. These L shells seems to be less important for our analysis. [from *Bučík et al.*, 2003a].

earlier discussed by *Roederer* [1970].

6.1.1 Data in $L-B$ Space at Constant Altitude

Roederer [1970] pointed out that physical region for one particular $L > 1$ is bounded by two values, namely, magnetic field at Earth's surface and magnetic filed at equator (i.e. minimum B value). Due to azimuthal asymmetry of real geomagnetic field, the physical region for the lowest L shells is not opened for all longitudes. This longitude range is bounded by two values where minimum B (definitely in dipole field) intersects the Earth's surface. In contrary the dipole approximation, the altitude of the fields values varies with

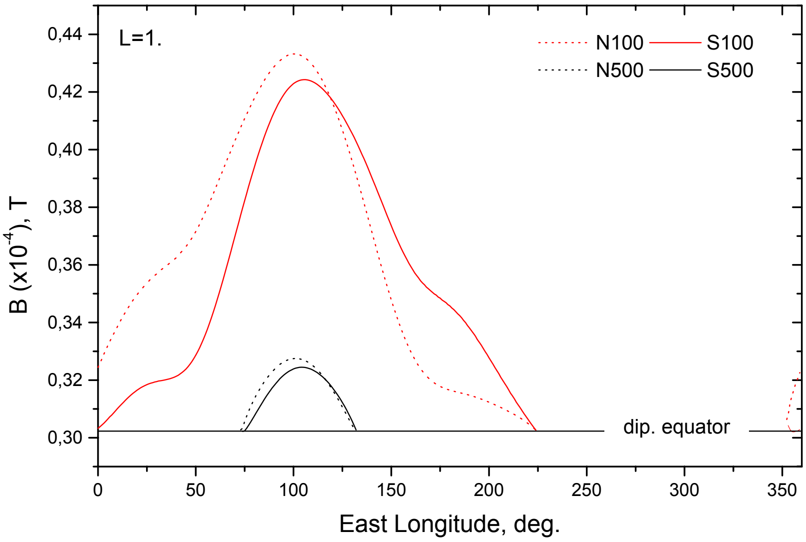

Figure 6.2. The longitude spread of northern (dot) and southern (solid) mirror points at both 100 (red) and 500 km (black) altitudes at magnetic shell $L = 1$. The solid horizontal line indicates magnetic equator in dipole approximation (i.e. no longitude dependent). [from *Bučík et al.*, 2003a].

longitude, differently on south and north filed value from minimum B. Each magnetic field value, lock in the certain B range, which is L-shell determined, has own altitude spread. From field geometry follows that B at its maximum altitude presents maximum field at given altitude, and vice versa. Similarly, magnetic field at minimal altitude is minimum filed for this altitude.

Altitude-Section of $L - B$ Space

A constant altitude in real magnetic field selects no various B values but various B ranges on different L shells. Therefore, the fixed altitude in $L - B$ coordinates is bounded by two curves, namely, the curve of the minimum magnetic field strength $B_{\min}$, and curve of the maximal value of the magnetic field $B_{\max}$, respectively. At given L-shell, magnetic field values are spread with the longitude. It is not seen in $L - B$ diagram. At lower L-shell, the minimum field on a given altitude agrees with the minimum at given L, i.e. with equatorial

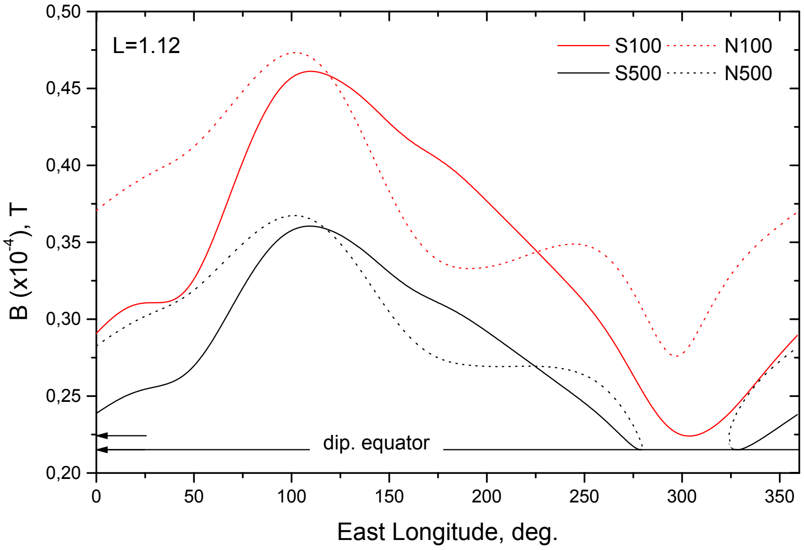

Figure 6.3. The longitude spread of northern (dot) and southern (solid) mirror points at both 100 (red) and 500 km (black) altitudes at magnetic shell $L = 1.12$ (*bottom*). The solid horizontal line indicates magnetic equator in dipole approximation (i.e. no longitude dependent). [from *Bučík et al.*, 2003a].

field value. It is demonstrated in Fig. 6.1 where the levels of 100 and 500 km altitudes are displayed. From this figure is seen that some of the diagram points (or the drift shells) are common for both altitudes; different altitudes are attained on different longitudes. Altitude of 100 km is often considered as a limit between zero and total absorption [*Vampola and Gorney*, 1983]. Its significance has been recently tested by *Réveillé et al.* [2001]. The altitude of 500 km is near average altitude of CORONAS-I satellite, which gamma-ray data are mapped in $L - B$ coordinates.

Generally, for one particular altitude there are three sets of magnetic L shells: the first group - the lowest L values are skipped by the altitude, the second set is composed with shells, which are not account for all longitudes, and into third group comes those, which are defined at all longitudes. Note that at the second set of L shells, magnetic equator appears. All three shell groups are separated by two boundary L values; lower one presents the first L-shell defined on specific altitude, and should appear on the magnetic equator (strictly

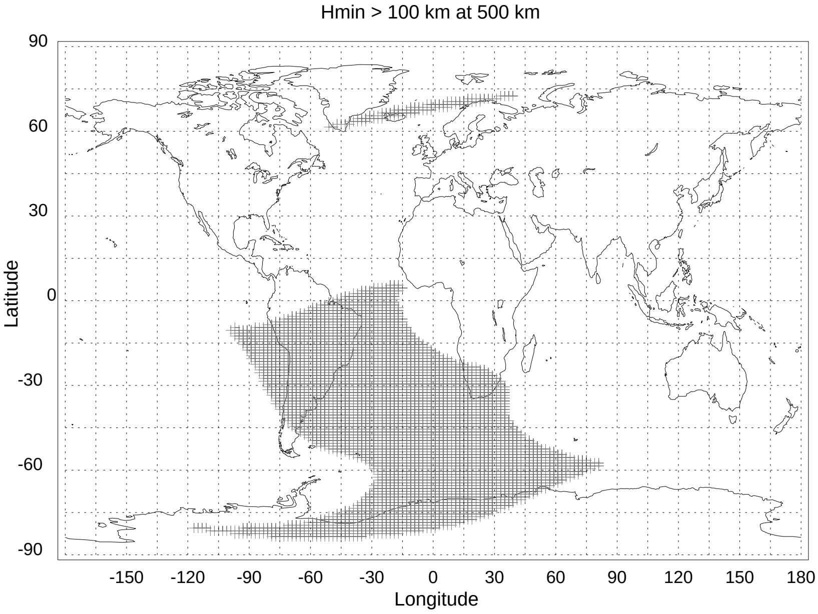

Figure 6.4. The shaded areas indicate the stable trapped regions at 500 km. The zone consists of the set of $[L, B]$ points at 500 km for which L-coordinate is less than 8 and B-coordinate is below B^{100}_{min}. [from *Bučík et al.*, 2003a].

only in dipole field), second one is the last L-shell where the equatorial field value is still presents.

Longitude Spread of B Field

The magnetic field variation with longitude on L shells equal 1, 1.12, and 3.9 are illustrated in Fig. 6.2, 6.3, and 6.6. The Fig. 6.2 shows that magnetic equatorial value appears both at 100 and 500 km altitudes. One can find that B_{max} at 500 km (at north) appears at 100 km near the 160° East Longitude (E. L.), and continues to descent much more deeper. However, the altitude 500 km presents maximum height for this field value. Since all mirror points at 500 km fall below 100 km somewhere at other longitudes, there could not be stable trapped particle population at 500 km.

In Fig. 6.3, the arrows indicate the interval of B values at $L = 1.12$ which lowest altitude descent for all longitudes is above 100 km. The charged particles having mirror points in this field range, e.g. those at 500 km, could be stable trapped. Notice, upper limit of this range consist of B_{min} at 100 km (labeled by B^{100}_{min}). Equivalently, the altitude of 100 km

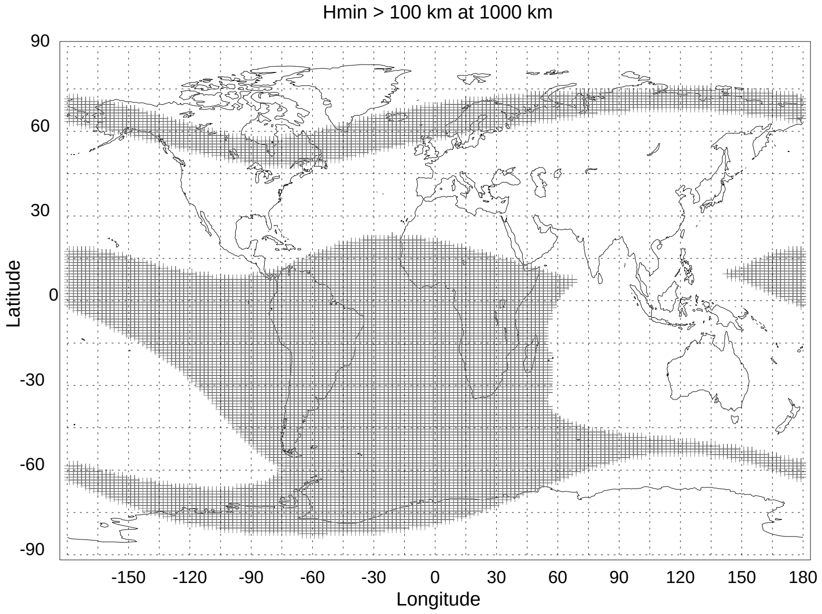

Figure 6.5. The shaded areas indicate the stable trapped regions at 1000 km. The zone consists of the set of $[L, B]$ points at 1000 km for which L-coordinate is less than 8 and B-coordinate is below B_{min}^{100}. [from *Bučík et al.*, 2003a].

does not reach magnetic equator at $L = 1.12$ at any longitude. The closest approach takes place at longitudes near the 300° E. L. for southern mirror points. At these longitudes, the near-equatorial particles (at quite narrow B-range) are stable trapped. It is seen from the Fig. 6.3, only those particles can be stable trapped (e.g. at altitude of 500 km) which mirror points have magnetic field value below B_{min}^{100}. A minimum longitude trace altitude H_{min} of these L, B points is above 100 km.

The L-shell in Fig. 6.3 is close to the limiting L value separating the stable trapping zone; below this boundary L, the stable trapped population can not be maintained. On the assumption that altitude of 100 km is trapping boundary, this limiting L-shell have been found as a last magnetic shell where altitude 100 km accounts the equator. One can find that L equals 1.099. We conclude, above $L = 1.099$ the B_{min}^{100} curve separates regions of stable and non-stable trapped particle population. The results is seen in Fig. 6.1. At altitude of 500 km the larger area lies in the non-stable trapping zone. We expect toward the higher altitudes the non-stable trapping zone reduces. In Fig. 6.4, 6.5 we see examples how B_{min}^{100} curve in geographical coordinates cuts the stable trapped regions (shaded areas)

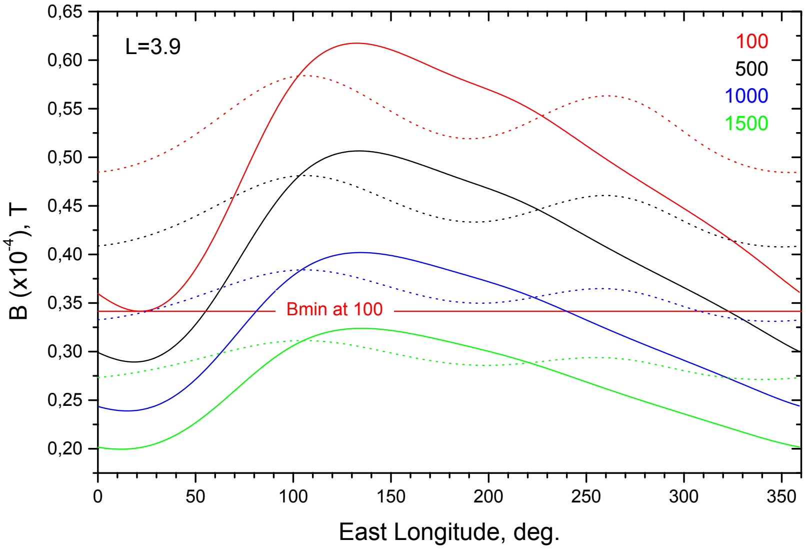

Figure 6.6. The longitude spread of northern (dot) and southern (solid) mirror points at 100 (red), 500 (black), 1000 (blue), and 1500 (green) altitudes at magnetic shell $L = 3.9$. The field B_{min}^{100} is indicated by solid horizontal red line. [from *Bučík et al.*, 2003a]

both at 500 and 1000 km.

The longitude distribution of mirror points at altitudes of 1000 and 1500 km are added at $L = 3.9$ (Fig. 6.6). Notice any intersection of the solid curve (southern field value) with dot (northern field) determines the altitude of the magnetically conjugate mirror point.

At longitude intervals of $0° - 55°$ E. L. and $320° - 360°$ E. L. the southern mirror points at 500 km have conjugate points in altitude range of $1000 - 1500$ km, which can be easily deduced from position of dot-north blue curve. Therefore, charged particles having these mirror points are locally (on specific field line) trapped. They are also stable trapped (i.e. on their whole azimuthal path) because their south mirror points do not fall below 100 km. The conjugate-northern mirror points are still somewhere above $900 - 1000$ km.

Between the 55° and 320° E. L. the southern mirror points at 500 km have conjugate points above altitude of 100 km (may be above 300 km), particles could be locally trapped. However, the stable trapping is not possible; particles in course of their azimuthal drift encounter the altitude 100 km, they are in so-called drift loss cone (DLC).

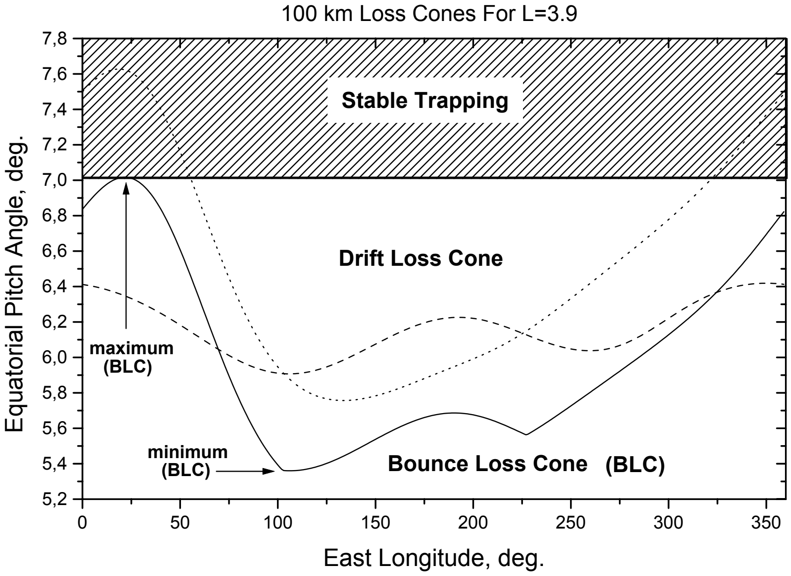

Figure 6.7. Illustrating the loss cones in terms of equatorial pitch angles at $L = 3.9$. Northern (dash) and southern (dot) 500 km mirror points are also displayed. The BLC is defined as the larger of either the northern or southern 100 km BLC.

In 0° – 70° and 325° – 360° E. L. intervals, the conjugate points of the northern mirror points at 500 km are below 100 km altitude where particles are lost in the atmosphere. Since, bouncing along the field line destined particle into the atmosphere, we say that particles are in the bounce lost cone (BLC). In 70° – 325° E. L. range, the northern mirror points at 500 km have conjugate points above 100 km. In this longitude range, locally trapped particles are in the DLC because they are destined to enter the atmosphere by southern mirror points during azimuthal drift.

The Fig. 6.7 depicts the relationship between the equatorial pitch angle of a particle on $L = 3.9$ shell and its destiny as a function of east longitude. A particle that has a local mirror point below 100 km will be immediately lost into the atmosphere, i.e. it's in the BLC. A particle which has an equatorial pitch angle between that of the local BLC and the maximum BLC (which occurs at $\sim 25°$ E. L.) is in the DLC, since at some longitude, it will encounter a 100 km mirror altitude and be lost into the atmosphere. Particle with equatorial pitch angles greater than this maximum BLC are considered stable trapped. A

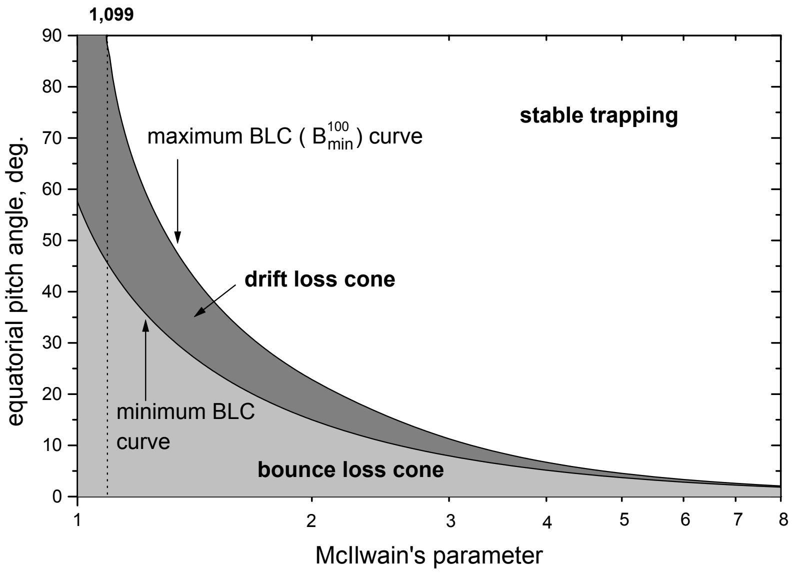

Figure 6.8. Aperture of loss cones as a function of L. Particles in DLC area can be temporarily trapped over some portion of longitude.

thorough discussion of this effect is available elsewhere [e.g. *Vampola and Kuck*, 1977]. The loss cone aperture variations over L shells is illustrated in Fig. 6.8.

6.1.2 Application for Gamma Rays

The trajectory of CORONAS-I in $L-B$ space and the spacecraft altitude variation for a single representative orbit on day 25.6.1994 is demonstrated in Fig. 6.9 and 6.10.

CORONAS-I observations of the $0.12-0.32$ MeV and $3-8.3$ MeV gamma rays over the period from March through June 1994 in $L-B$ coordinate system are shown in Fig. 6.11 and Fig. 6.12, respectively. Note, the data in $0.12-0.32$ MeV are not corrected for cosmic-ray proton induced background.

The data have been divided into the pixels according to the L, B coordinates. The McIlwain's L parameter was chosen from 1 to 6. In this range data have been separated into the 180 intervals with the step of $\Delta L = 1.01^{i+1} - 1.01^{i}$, where $i = 0,\ldots,179$. The B has constant step with $\Delta B = 2\times 10^{-7}$ T. The average number of measurements points

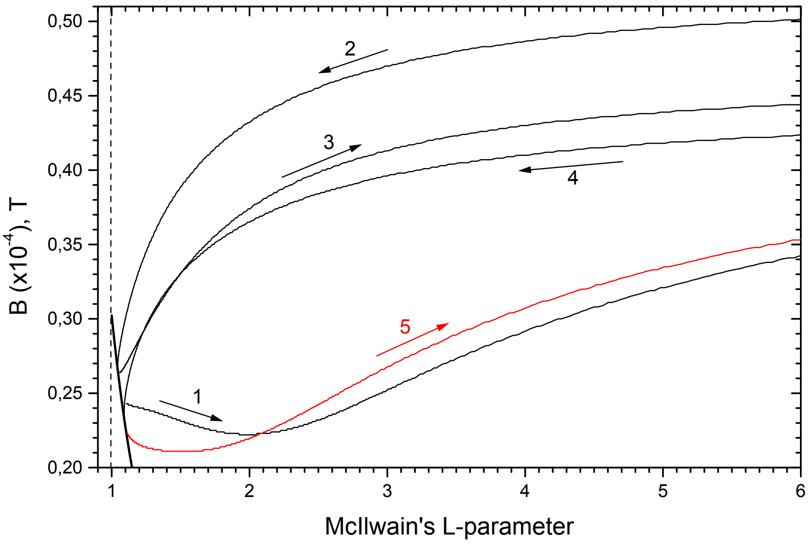

Figure 6.9. The trajectory of CORONAS-I in $L-B$ space for a single orbit on day 25.6.1994 (black line). The part of the next orbit is displayed by red. The direction of motion of CORONAS-I is indicated by arrows. Thick line in the left corner indicates the magnetic equator [from *Bučík et al.*, 2003a].

in one individual pixel is 50 and the total amount of the data in the selected L range is 1.05×10^6 data points. For each of these pixels the estimation of the mean and variance have been evaluated.

The inspection shows that enhanced radiation clusters into two L bands. In the energy range of $3-8.3$ MeV, the first one is bounded by $1.1 < L < 2.1$ with the flux maximum at $L \sim 1.28-1.4$, and the second one corresponding to L shells between $2.4-5.3$ with flux maximum at $L \sim 3-4.5$. The two bands are separated by the zone of flux decreasing. Comparison with nominal locations of the trapped radiation belts shows that the first, more intense zone is centered onto the inner radiation belt an the second wide band lies at position of the outer radiation belt as well as at peripheral regions of the slot between the belts. The presence of the enhanced fluxes above the albedo background level in the stable trapped region between the belts may indicate the existence of the unstable radiation belt. The weak growth of the gamma-ray flux in the slot region may be relict of the unstable

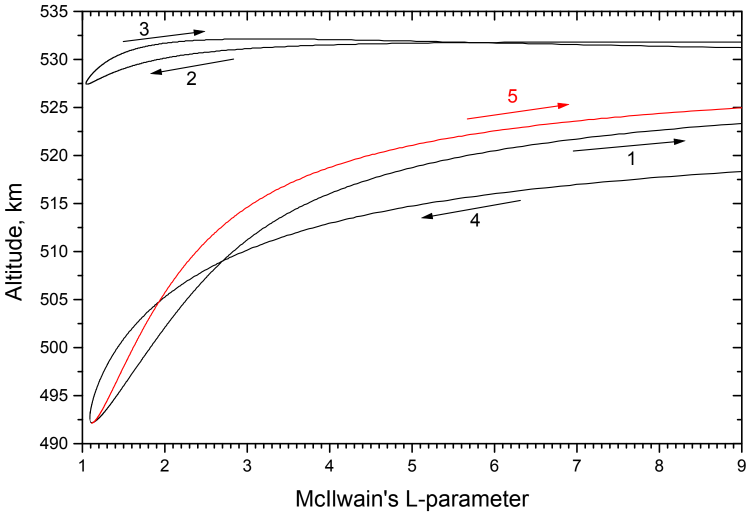

Figure 6.10. The altitude of the CORONAS-I vs L-shell parameter illustrates the satellite altitude variation for a single orbit on day 25.6.1994 (black line). The part of the next orbit is displayed by red. The direction of the spacecraft motion is indicated by arrows [from *Bučík et al.*, 2003a].

belt of energetic electrons, formed after electron injection and consequent radial diffusion during and after the strong magnetic disturbances [*Blake et al.*, 1992; *Xinlin et al.*, 1993]. Such electron population can have relatively large lifetime. *Galper et al.* [1999] observed the unstable high-energy (10 – 50 MeV) electron belt in the slot region more than 2 years after its creation on March 24, 1991.

The flux distribution in Fig. 6.11 is more complicated. It depicts extremely high fluxes just on the boundary of the inner radiation belt. Toward the centre of it the more light zones are seen, which is most probably caused by the instrument overloaded due to a very large particle flux in the inner belt region.

Obtained $L - B$ maps are similar (by position and a pattern of the spatial structure of the enhanced flux) to the another one containing electron fluxes measured by MKL device on the CORONAS-I satellite during the same time of the observation. The distribution of average electron fluxes in energy ranges of 0.5 – 1.5 and 6 – 12 MeV in $L - B$ coordinates is shown in Fig. 6.13.

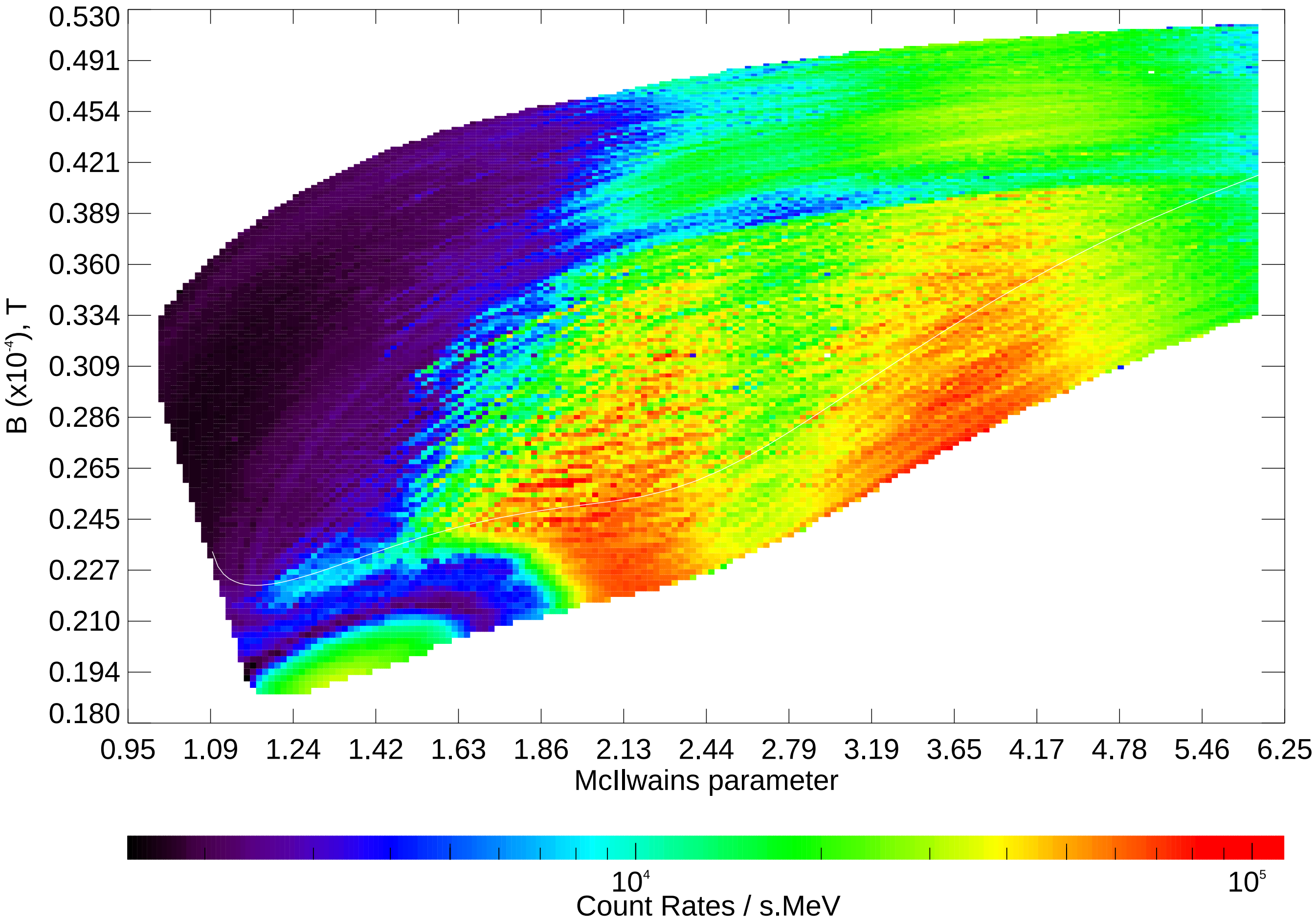

Figure 6.11. Distribution of average gamma ray fluxes at CORONAS-I altitude in $L - B$ co-ordinate system for energy range of $0.12 - 0.32$ MeV during the period March-June, 1994. B_{min}^{100} is displayed by white. Colored scale matches the log of the counts. [from *Bučík et al.*, 1999b].

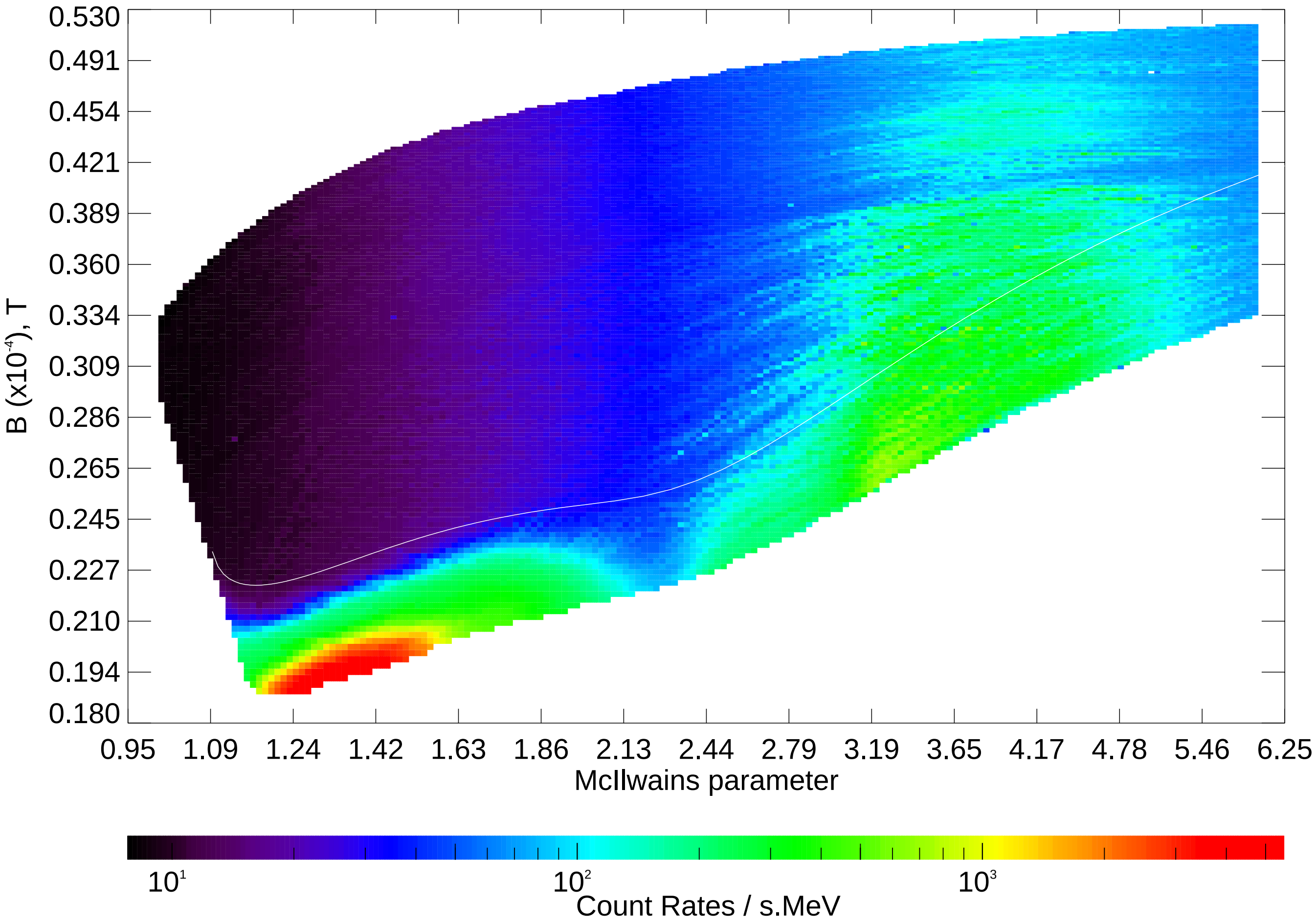

Figure 6.12. Distribution of average gamma ray fluxes at CORONAS-I altitude in $L - B$ co-ordinate system for energy range of $3 - 8.3$ MeV during the period March-June, 1994. B_{min}^{100} is displayed by white. Colored scale matches the log of the counts [from *Bučík et al.*, 2003a].

Inner Zone

It is evident that enhanced fluxes of $3-8.3$ MeV gamma rays observed in the inner zone ($L<2$) are well organized according to $B_{\min}^{100}$ curve. The population of stable trapped electrons with energy >3 MeV presents in the inner belt and impinging on any local matter near the detector could be responsible for the high bremsstrahlung fluxes in energy interval $3-8.3$ MeV observed on CORONAS-I.

At specific $L-B$ position, not only mirroring particles can contribute to the gamma-ray production, also particles which mirror deeper below the satellite altitude. Thus, B-coordinate corresponds to the smallest mirror point magnetic field intensity for particles at CORONAS-I altitude. This fact can explain the structure of the gamma-ray flux distribution: higher fluxes are observed towards the equator. Since all particles mirroring along the field line are passing through the magnetic equator in course of their longitudinal bounce displacement, the flux could rise gradually as a magnetic field approach to its minimal value. However instead of slowly varying flux with field B, we observe the steep gradient of gamma-ray flux in the inner zone. *Lemaire et al.* [1995] discussed that in the inner zone the steep gradient of particle flux is controlled by the density distribution of the atmosphere.

Outer Zone

Contrary inner zone, the enhanced fluxes in the outer radiation belt are also observed out of the stable trapping region. *Blake et al.* [2002] presented comparison of Solar Anomalous and Magnetospheric Particle Explorer (SAMPEX) and CORONAS-I drift loss cone observations of relativistic electrons and $3-8.3$ MeV gamma rays over the March-June, 1994.

Since atmospheric cutoff takes place far from the magnetic equator where an overall flux has maximum, the gamma-ray flux gradient observed in the outer zone is not so steep than in the inner radiation belt.

To clarify more carefully the observed flux in outer zone, we follow for gamma rays at $L=3.9$ along the longitude. At this L-shell the peak of drift loss cone gamma rays have been found over the studied time period [*Blake et al.*, 2002]. Illustration of the south and north atmospheric precipitation zones is diagrammatically given in Fig. 6.14. In longitude intervals $0^\circ-20^\circ$ and $230^\circ-360^\circ$ E. L. at Southern Hemisphere and $100^\circ-190^\circ$ E. L. at

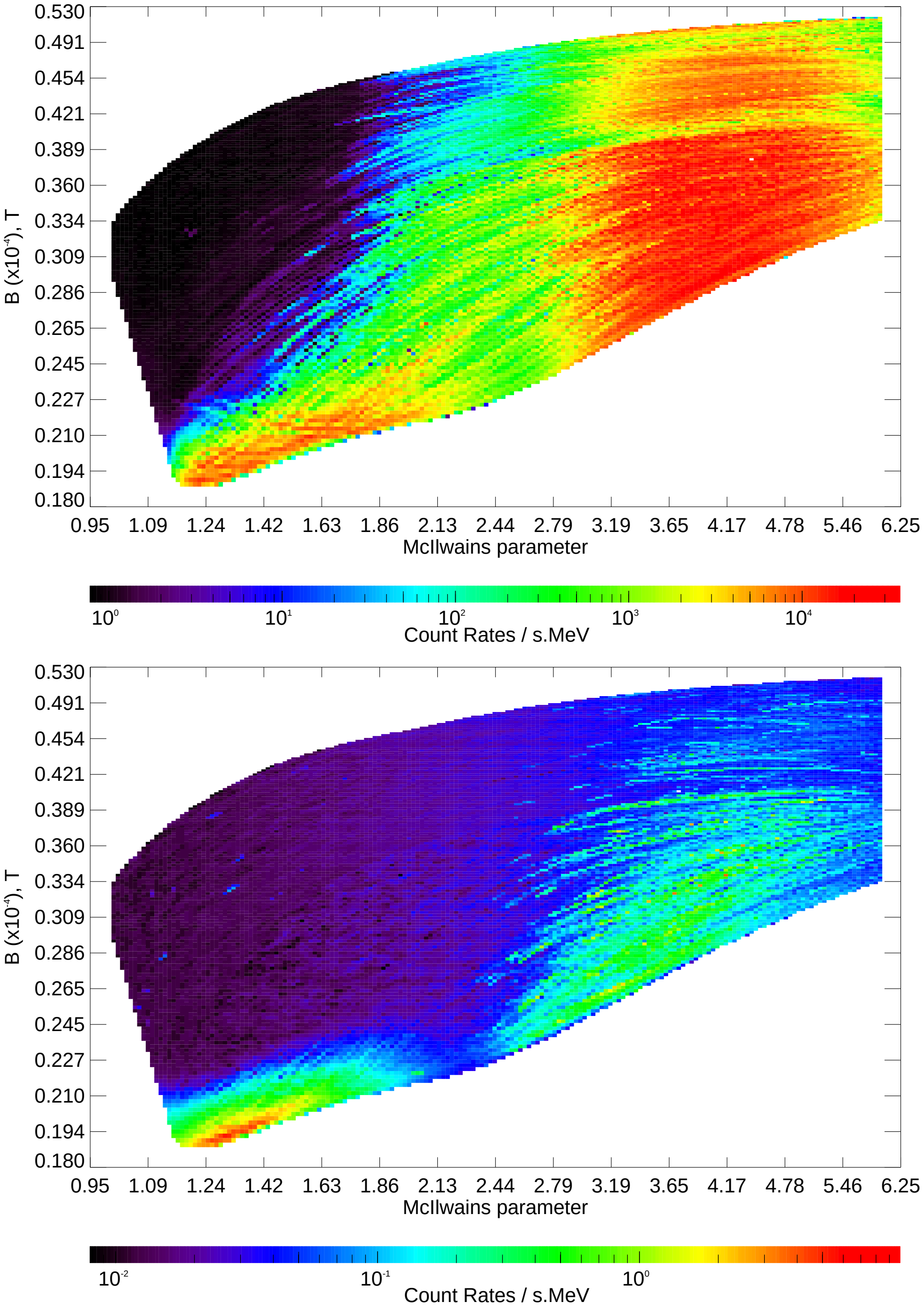

Figure 6.13. Distribution of average electron fluxes at CORONAS-I altitude in $L - B$ coordinate system for energy ranges of $0.5 - 1.5$ MeV (*top*) and $6 - 12$ MeV (*bottom*) during the period March-June, 1994 [from *Bučík et al.*, 1999b].

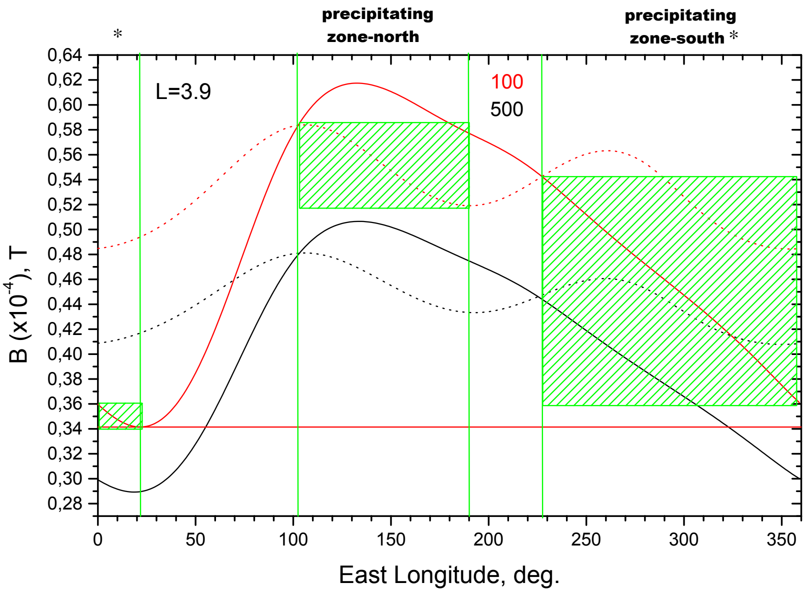

Figure 6.14. South and north precipitation zones at $L = 3.9$ are indicated by green dashed area. The remaining graphic has the same meaning as in the Fig. 6.6 [from *Bučík et al.*, 2003a].

Northern Hemisphere, the quasitraped electron population build up during azimuthal drift, due to continuous injections over longitudes, is destined to enter the altitude of 100 km. We suppose remote bremsstrahlung is observed approximately in the same longitude intervals at satellite altitude.

The detail inspection of the Fig. 6.14 leads to the preliminary scheme of various bremsstrahlung components of the gamma-ray flux along the longitude at satellite positioned in the outer zone, specifically at $L = 3.9$. The scheme is given in Fig. 6.15.

Gamma rays from DLC electrons produced both in the atmosphere and in the satellite mater have to rise west before precipitating regions due to electron accumulations during the eastern azimuthal drift. An amount of the bremsstrahlung photons could be also determined by the aperture of the loss cones. For example, in the range $120° - 220°$ E. L. the aperture of the local bounce loss cone at 500 km is larger at Northern Hemisphere than at Southern Hemisphere (see Fig. 6.14). It implies higher bremsstrahlung fluxes due to higher flux of quasitrapped electrons in this longitude interval. However higher fluxes at north

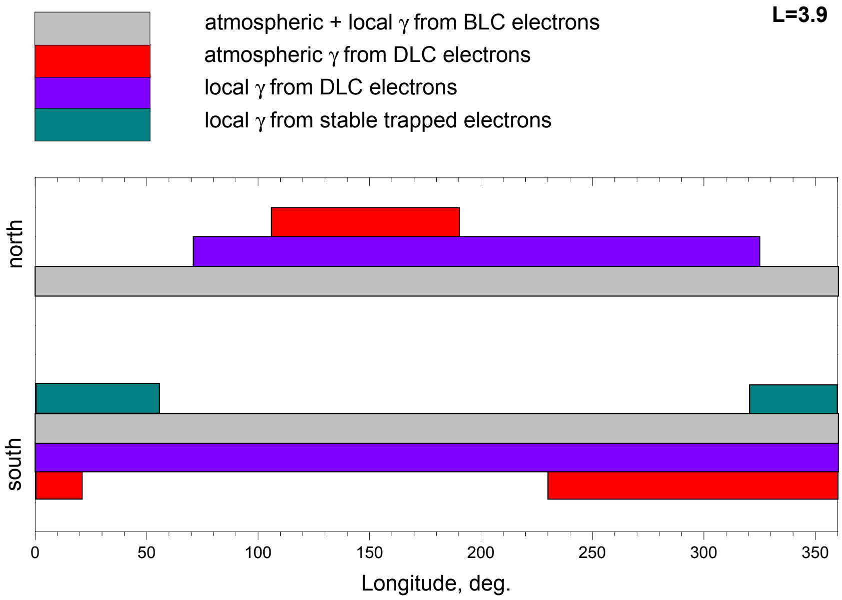

Figure 6.15. The schematic diagram illustrating the longitude distribution of various sources of the bremsstrahlung photons at $L = 3.9$ seen by satellite on south and north [from *Bučík et al.*, 2003a].

could be rather caused by the presence of the atmospheric precipitation zone here. Remember flux of drift loss cone electrons is the essentially same both for local and atmospheric bremsstrahlung production.

Probability for production of bremsstrahlung photos is inversely proportional to the radiation length, one can find that production of photons in Aluminium (an element, typical in construction materials) is higher about factor ~ 1.5 than in the atmosphere. Since into the specific point in $L - B$ space at satellite altitude can contribute bremsstrahlung photons from large-scale atmospheric areas, the gamma-ray flux produced in the atmosphere by the bremsstrahlung process can be evenly higher. A more quantitative study comparing local and atmospheric bremsstrahlung production is being undertaken.

As can be seen from scheme at Fig. 6.15 the gamma rays due to BLC electrons are distributed at all longitudes. Notice only particles that strictly mirror at altitude of 500 km are closed in northern BLC longitude intervals of $0° - 70°$ and $325° - 360°$ E. L. (see Fig. 6.6).

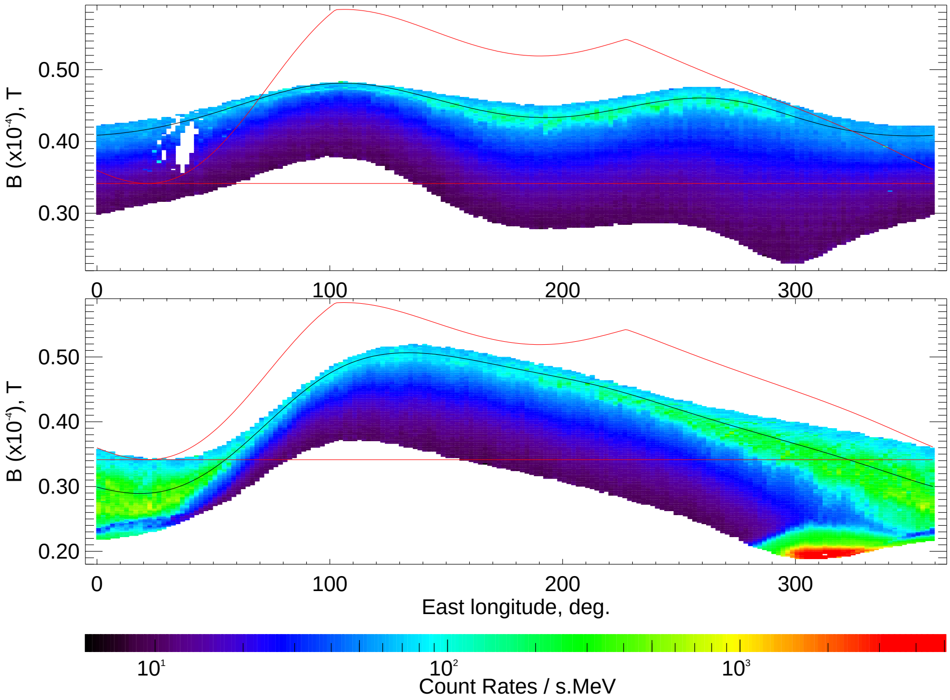

Figure 6.16. The longitude spread of $3 - 8.3$ MeV gamma rays at both north (top) and south (bottom) observed by CORONAS-I satellite. L-shell of 3.9 at 500 km is indicated by black line. Only fluxes between $L = 1.2$ and $L = 6$ are displayed. Loss cones at $L = 3.9$ are illustrated by red curves. Below the red horizontal line the stable trapping zone is indicated, above, the DLC area is bounded by mountain-shape red curve. The remaining place on the graph pertains to the BLC [from *Bučík et al.*, 2003a].

The proposed longitude spread of various bremsstrahlung sources in gross features agrees well with our measurements on CORONAS-I satellite presented in Fig. 6.16. The east-west asymmetry due to eastern electron drift and north-south asymmetry in position of atmospheric precipitation zones and in the loss cone aperture variation seems to explain partly the measured data. We see that proper interpretation of particle data in altitude-section requires data tracking along the longitude for L-shell and altitude intersections.

At the present time, a model for electron loss via drift in the DLC in the outer belt has been reported by *Sheldon and Benbrook* [2003], which predicts that almost all of the outer belt precipitates in a small geographic area over the Weddell Sea in Antartica ($\sim 310° - 350°$ E. L.), the zone covered by our most intense gamma-ray flux enhancements.

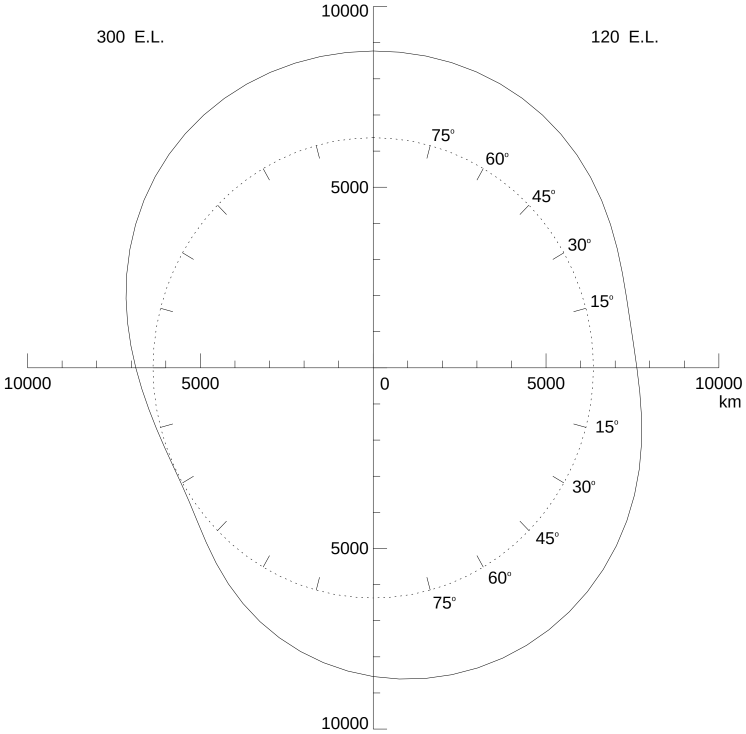

Figure 6.17. The intersection (solid curve) of the $B = 3.021 \times 10^{-5}$ T surface with the meridional plane at 300° E.L. As can be seen the closer approach of the field to Earths's surface is attained at 300° E.L. in the Southern hemisphere, the region of the SAA.

Enhanced Fluxes in the Geographical Map

Separation of the dipole centre from the Earth's centre and the inclination of the magnetic axis with respect to the rotation axis produce a local depression in the low altitude magnetic field distribution at constant altitude. As the trapped particle population is tied to the magnetic field, the lowest altitude radiation environment peaks in the region where the magnetic field is depressed [*Roederer*, 1970]. This region is located to the south east of Brasil, and is called the South Atlantic Anomaly.

The illustration of the north-south and azimuthal asymmetry in the Earth's magnetic field distribution is displayed in Fig. 6.17. The depression of the magnetic field strength in the region of SAA is illustrated in Fig. 6.18.

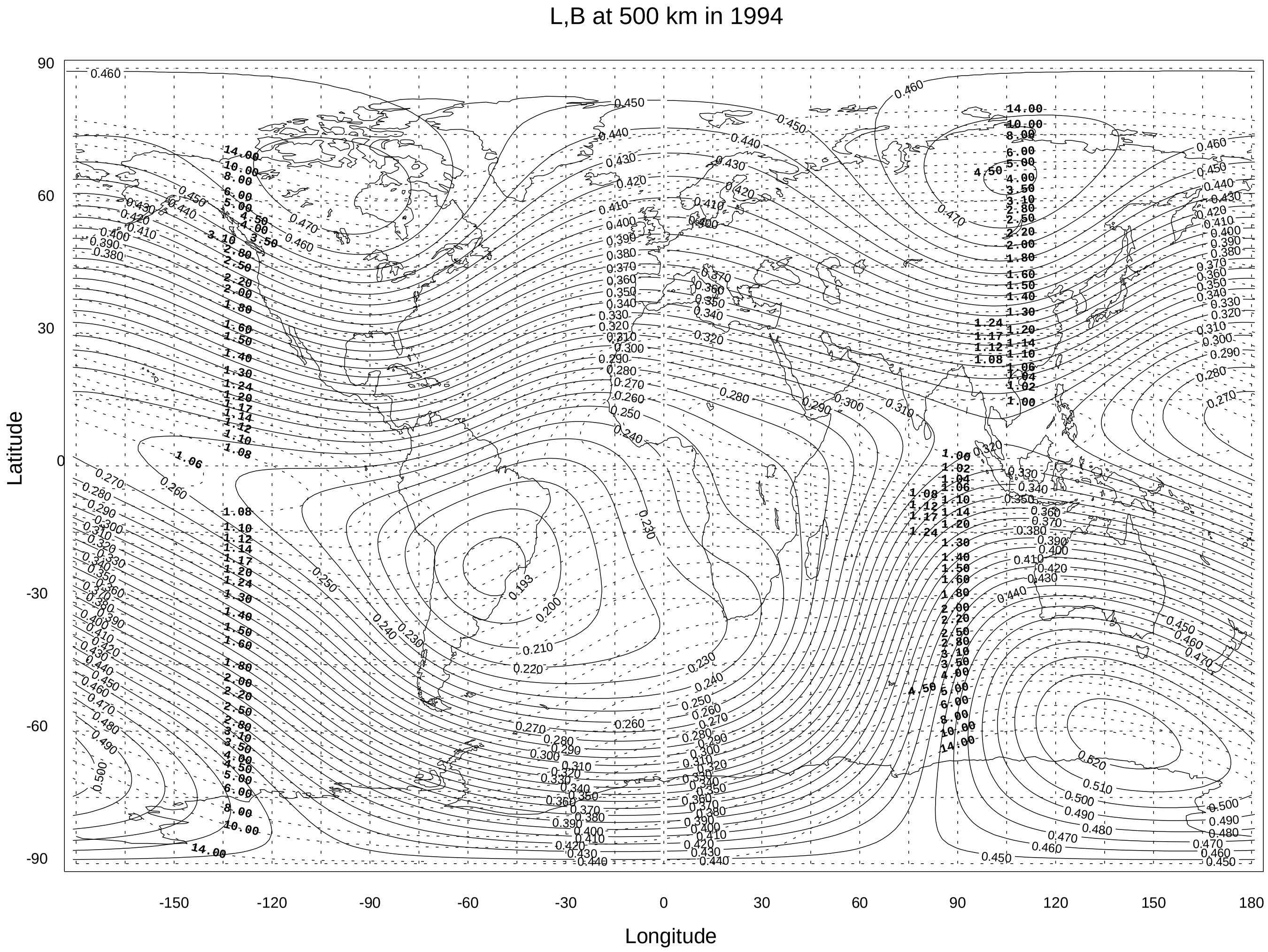

Figure 6.18. The map of the L, B coordinates for the real geomagnetic field. The solid lines represent isointensity lines for geomagnetic field at altitude of 500 km. The field intensity is in units of 10^{-4} tesla. The dotted lines are the lines of the intersection of the magnetic shells, L with the altitude of 500 km.

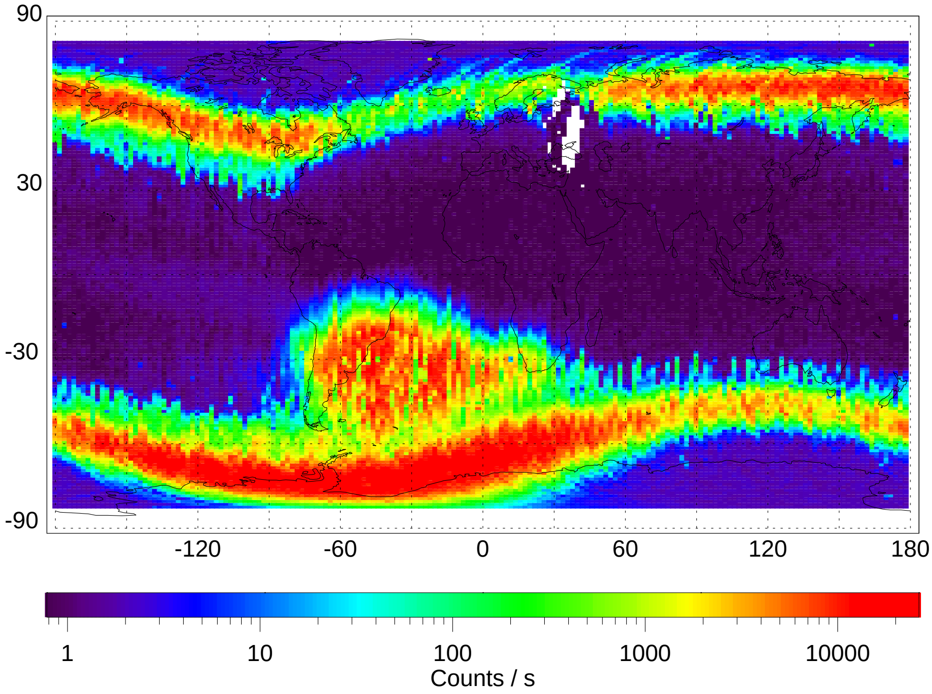

Figure 6.19. Map of the average electron fluxes in the energy range $0.5 - 1.5$ MeV detected by MKL electron sensor aboard CORONAS-I during the period March-April, 1994 [from *Bučík et al.*, 2003b].

The SAA shows up clearly in both geographical maps of gamma-ray flux distribution in Fig. 4.3, and 4.4. Outside the SAA gamma-ray flux is very high at high latitudes where field lines from the outer electron belt reach down to low altitudes. The enhanced fluxes in SAA and down this area coincide with the zone where $H_{min} > 100$ km (see Fig. 6.4).

For comparison with $0.12 - 0.32$ MeV gamma rays, the geographical map of electron fluxes in the energy range $0.5 - 1.5$ MeV is shown in Fig. 6.19. It is clear from this figure that electrons in the DLC are observed at similar L shells in geomagnetically conjugate regions. What is observed on CORONAS-I at given longitude is the mixture of all electrons in DLC that have been scattered somewhere west of the satellite position and at both ends of the field line.

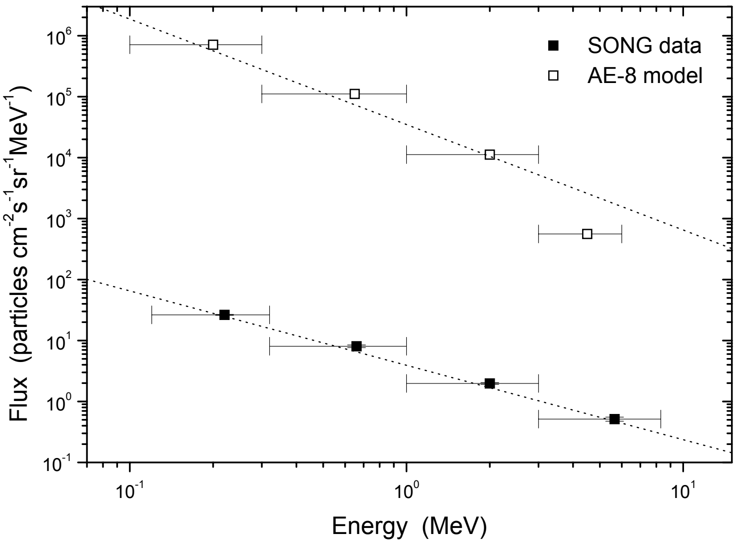

Figure 6.20. Example of the energy spectra at selected (L, B) pair of the AE-8 electrons and gamma rays measured with SONG device. The dashed lines represent a power law approximations $I_e = 3.49 \times 10^4\, E^{-1.73}$, $I_\gamma = 3.92\, E_\gamma^{-1.22}$ [from *Bučík et al.*, 2002b].

6.2 Energy-Spectral Characteristics

Method

For the spectral analysis, the CORONAS-I data measured in the outer radiation zone ($L = 3 - 5$) have been separated into 19 intervals in L with stepsize of $\Delta L = 0.1$ at L shells between 3 and 4.6, and $\Delta L = 0.2$ at L between 4.6 and 5. In the inner belt region we chose 8 intervals in L with stepsize of $\Delta L = 0.05$ at $L = 1.2 - 1.6$. Only those data have been chosen which pitch angles varied from 75° to 105°. At $L = 3 - 5$, six various intervals in B were selected with step of $\Delta B = 2 \times 10^{-6}$ T between the minimum value at altitude 500 km and $B_{\min}^{100}$. Note, here we are concerned with measurements at positions where the minimum drift altitude is above 100 km. The average number of measurements in individual pixel is 77 (excluding those with number of observations less than 10). In the region $1.2 < L < 1.6$, we performed the same treatment. Between two boundary values of B in the inner zone we have chosen 6 ranges with step of $\Delta B = 4 \times 10^{-7}$ T. The average number of measurements

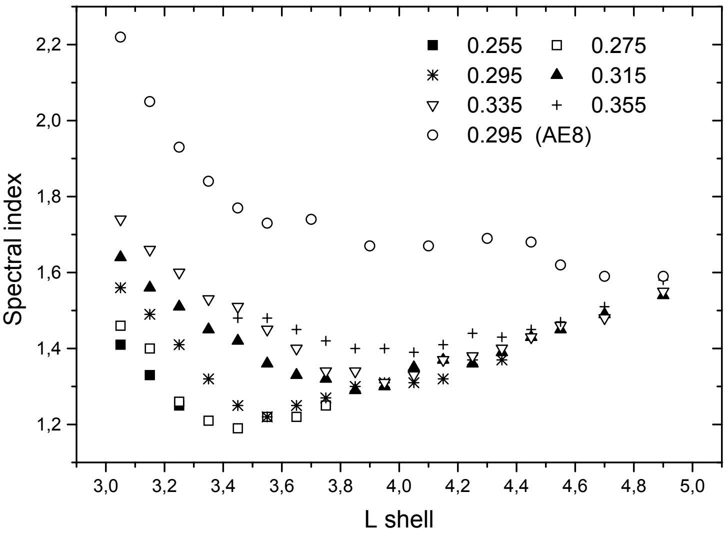

Figure 6.21. The variation of the gamma-ray energy spcetrum on L at various values of B. The numerals at symbols indicate field in units of 10^{-4} tesla. The spectrum is fitted in the 0.12 − 8.3 MeV range. The open circles represent the AE-8 spectral indices at $B = 0.295 \times 10^{-4}$ T between 0.1 and 6 MeV. [from *Bučík et al.*, 2002b].

in the bins in the inner region is 106. The positions of these pixels is represented by their centers. Notice that the edge pixels including the minimal values of B at given L interval also cover the $[L, B]$ points which have not been indeed attained on altitude 500 km.

The selection of the boundary values of L parameter has been done in accordance with the AE-8 model [*Vette*, 1991]. The differential omnidirectional fluxes of AE-8 electrons have been evaluated for epoch of solar minimum (magnetic field model for epoch 1964). The unidirectional fluxes in the model were obtained dividing omnidirectional ones by factor 4π sr. The pitch angles of observations are obtained from the known satellite orientation in the earth's magnetic field.

It has been obtained from the SONG data that the $3-8.3$ MeV mean gamma ray albedo flux is equal to 0.186 photons $(\mathrm{cm}^2 \text{ s sr})^{-1}$ at $L = 3-5$. This intensity achieves at least 7 % of total measured flux at altitude of 500 km, and it was subtracted from the detected gamma ray flux. Because of the hardness of the albedo spectrum, this contribution is not

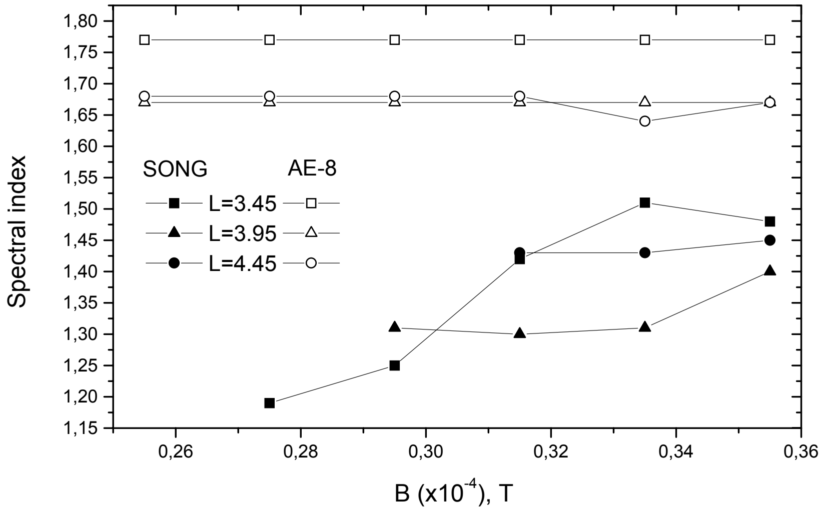

Figure 6.22. The SONG (solid symbols) and AE-8 (open symbols) spectral indices plotted as a function of the Earth's magnetic field for three L values [from *Bučík et al.*, 2002b].

as significant in the remaining three energy channels (lower energies).

The spectra of energetic electrons trapped in the radiation belts are often considered to be monotonic, the intensities falling off as the energy increases. Several analytic forms of electron energy spectra have been used. Among these were exponential and power law distributions. In the present work, the incident electron distribution is assumed to be power in shape. Example of the energy spectra of AE-8 electrons and gamma rays measured with SONG device at $L = 3.55$, $B = 2.95 \times 10^{-5}$ T are shown in Fig. 6.20. Power law fits to the data points are illustrated.

NASA AE-8 Electron Model

The National Aeronautics and Space Administration (NASA) trapped radiation model AE-8 consists of arrays of integral omnidirectional electron fluxes in the energy range 0.04 MeV to 7 MeV in the Earth's radiation belts ($L = 1.2 - 11$). The fluxes are stored as functions of energy, L-value, and B/B_0 (magnetic field strength normalized to its minimum value on

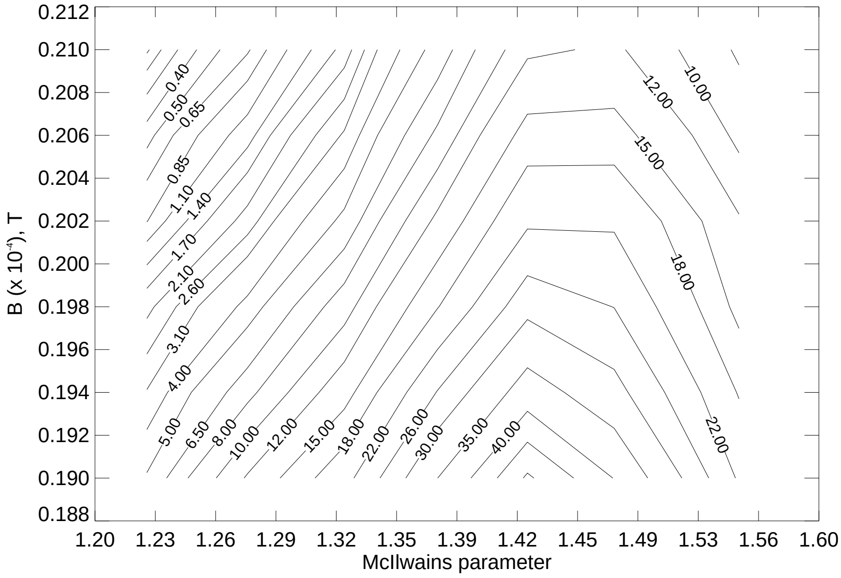

Figure 6.23. The lines of the equal intensity of the bremsstrahlung photons in L, B coordinates. The fluxes have been obtained from eqn. 6.3, integrating over the $3 - 8.3$ MeV range and corrected for absorption and detector efficiency. The numerals denote the photons $(\text{cm}^2 \text{ s sr})^{-1}$ [from *Bučík et al.*, 2002b].

the field line). As the NASA model is based on data collected before 1970, it essentially describe the radiation environment of the 1960s.

6.2.1 Outer Zone

The differential gamma ray energy spectrum in the $0.12 - 8.3$ MeV range has been approximated by a power law using the iterative histogram-fitting procedure (analogy of the least squares method, where the minimum of the sum of the squares of the differences between approximated and measured fluxes in the particular energy channels is iteratively obtained, by selection of the power low indices). The dependence of the energy spectrum on L at various values of B is shown in Fig. 6.21. Also shown is the AE-8 spectral index at $B = 2.95 \times 10^{-5}$ T. The variation of the slope of the gamma-ray spectrum on B at a given L is evident and is decreasing towards the high values of L. Starting from $L \sim 4.5$ this dependence is a very weak. In the region $3 < L < 5$ and $0.255 < B < 0.355$ $(\times 10^{-4})$ T the model AE-8 does not include such variation (see Fig. 6.22). It can also be seen from

Fig. 6.21 that the form of this dependence is characterised by softening of the energy spectra with increasing B, i.e. with decreasing of the geomagnetic cutoff at given L. This fact can be probably explained by albedo origin of electrons with $E > 120$ keV at $L = 3 - 4$ on altitude 500 km. The increase of the less energetic component of the primary cosmic rays by decreasing of the rigidity cutoff make the spectrum softer. The possibility of the formation of the trapped electron flux by cosmic ray primary nuclei in the region $L = 2 - 4$ is discussed in *Gusev et al.* [1987].

Up to a certain value of L (which depends on B) the gamma-ray spectrum in the $0.12 - 8.3$ MeV range is a decreasing function of L, and one can see similar pattern in model AE-8 (see Fig. 6.21). The position of minimum of the spectral index at $L = 3.5 - 4$ agrees with the trapped radiation model. As can be seen from Fig. 6.21, the gamma ray energy spectrum on the magnetic shells with $L > 3.5 - 4$ is softened with increasing L. It may be explained by the fact that the dominant source of such electron population beyond the $L \sim 4$ is their acceleration during diffusion on lower L shells. The weak dependence of gamma-ray spectrum on B at $L > 4$ gives also support for non-albedo production mechanism. Different L-variation of the spectral index at $L > 4.3$ may be caused by fact that AE-8 static model does not include magnetic storms effects which strongly affect electrons at higher L.

At lower energies the gamma rays are created mainly by bremsstrahlung of electrons stopped in any matter near the detector. The differential spectral shape of electron bremsstrahlung has equal or slightly harder slope than the electron one [*Chupp*, 1976]. Comparing the SONG and the AE-8 spectral slopes, it is evident that the electron spectrum within the energy range $0.1 - 6$ MeV is significantly softer than that belonging to gamma rays between 0.12 MeV and 8.3 MeV detected by SONG device. The flattening of gamma-ray spectra might be caused in part by Compton scattered gamma rays (what is the most important absorption process in the $0.1 - 10$ MeV range) before reaching the detector, due to the fact that the Compton cross section increases with decreasing of the energy. Another important reason for the difference between spectral slopes which must be taken into account are large temporal variations in the outer zone. It should be noted that in the AE-8 static model, averages were taken over long intervals (six months or more).

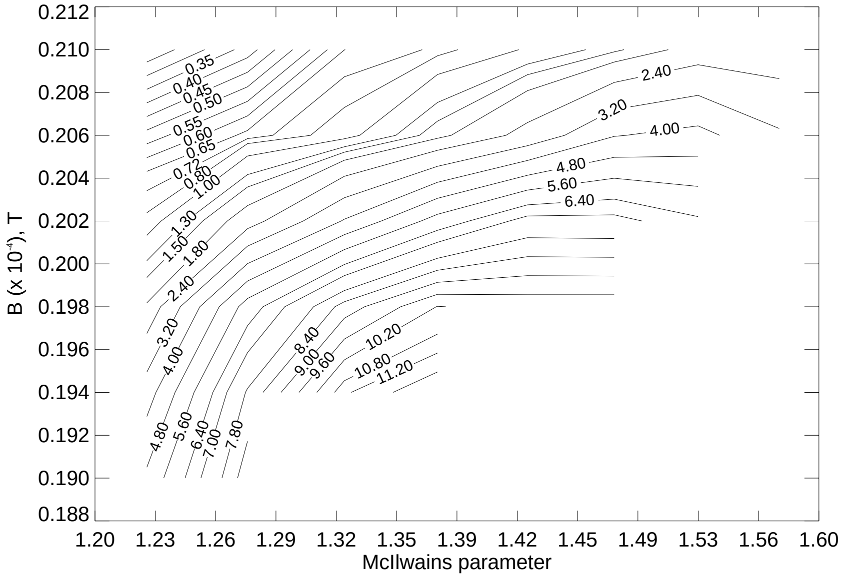

Figure 6.24. Contours of constant intensity of the gamma rays in L, B coordinates, detected by SONG device in energy channel 3 – 8.3 MeV. The numerals denote the photons $(\mathrm{cm}^2\ \mathrm{s\ sr})^{-1}$ [from *Bučík et al.*, 2002b].

6.2.2 Inner Zone

Owing to overflow of the SONG instrument for lower energies in SAA, we deal only with spatial distribution of gamma-ray fluxes in the 3 – 8.3 MeV channel. Since the rates of spallation and neutron induced gamma rays with energy above 3 MeV are very low, it is possible to expect that in energy range 3 – 8.3 MeV, bremsstrahlung gamma radiation could make a significant contribution also in the inner belt region.

If an incident electron spectrum is given in the form $I_e(E)\mathrm{d}E = K_e E^{-\alpha}\mathrm{d}E$, then the resulting differential spectrum of gamma rays is given by *Chupp* [1976]

$$I_\gamma(E_\gamma)\mathrm{d}E_\gamma = \frac{N_A}{A}\Delta x \int_{E_\gamma}^{\infty} \sigma_B(E, E_\gamma)\mathrm{d}E_\gamma K_e E^{-\alpha}\mathrm{d}E, \tag{6.1}$$

where N_A is Avogrado's number, A is the target mass number, Δx is the absorber thickness (g cm^{-2}), and $\sigma_B(E, E_\gamma)\mathrm{d}E_\gamma$ is the differential cross section for emission of a photon of energy E_γ in $\mathrm{d}E_\gamma$. In the highly relativistic case, with no screening by atomic electrons (near-collisions), the radiation cross section for $m_0c^2 < E < 137 m_0c^2 Z^{-1/3}$ is [*Chupp*, 1976]

$$\sigma_B(E, E_\gamma)\mathrm{d}E_\gamma \cong 4\sigma_0 Z^2 \ln\left(\frac{2E}{m_0c^2}\right)\frac{\mathrm{d}E}{E_\gamma}, \tag{6.2}$$

where Z is the atomic number, m_0c^2 is electron rest energy, and $\sigma_0 = 5 \times 10^{-28}$ (cm^2 per nucleus).

Replacing eqn. 6.2 in eqn. 6.1, we obtain

$$I_\gamma(E_\gamma)\mathrm{d}E_\gamma \cong \frac{N_A}{A}\Delta x 4\sigma_0 Z^2 K_e \frac{\alpha}{(1-\alpha)^2} E_\gamma^{-\alpha}\mathrm{d}E_\gamma. \tag{6.3}$$

Since the gamma ray intensity decreases exponentially after traversing a thickness Δx, the eqn. 6.3 must be multiplied by exponential term $\exp(-\mu\Delta x)$, where the average mass attenuation coefficient μ for energies between 3 and 8.3 MeV in aluminium equals 2.8×10^{-2} cm^2 g^{-1} [*Hubbell and Seltzer*, 1997].

Fig. 6.23 presents lines of the equal differential flux of bremsstrahlung photons in the $L - B$ coordinates, approximated for $3 - 8.3$ MeV range, and produced by AE-8 electrons between 0.1 MeV and 4 MeV on the assumption that the total shielding of the main counter, estimated in appendix B, is $\Delta x = 16.24$ g cm^{-2} of aluminium. Finally, the computed bremsstrahlung fluxes was multiplied by detector efficiency in 3-8.3 MeV channel. Since the AE-8 model does not include electrons above 4 MeV in the studied $L - B$ region, the inner belt electrons in the energy range 0.1 to 4 MeV practically do not contribute to $3 - 8.3$ MeV bremsstrahlung photons. So the power-law extrapolation used on Fig. 6.23 overestimates the bremsstrahlung effect.

The contours of the equal intensity of the gamma rays measured by SONG device in channel $3 - 8.3$ MeV are shown in Fig. 6.24. The position of the maximum intensity tends to appear at $L \sim 1.4 - 1.5$, the range consistent with AE-8 prediction. The similar pattern and absolute value of the observed and the calculated gamma-ray intensity is seen for L shells below ~ 1.3. At $L > 1.3$ the SONG gamma-ray fluxes depend on L less than those determined by AE-8 model.

6.3 Temporal Variability

During magnetic storms relativistic electrons in the outer radiation belt varies dynamically in location and intensity on both short and long time scale. The inner zone shows long-

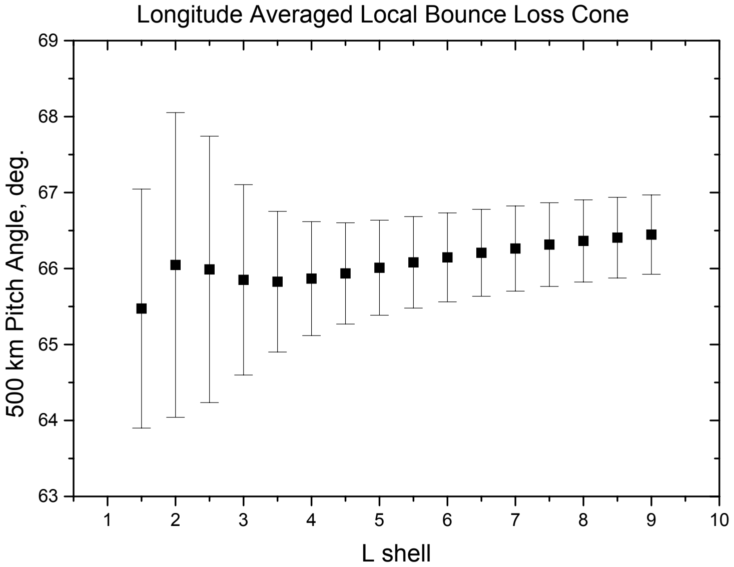

Figure 6.25. Illustrating the longitude averaged bounce loss cone at 500 km versus L value. The standard deviations of the 500 km pitch angles are indicated by error bars [from *Bučík et al.*, 2003b].

term stability being affected only by the most intense geomagnetic storms. Although the relationship between relativistic electron fluxes and magnetic storms has been known for many years [*Paulikas and Blake*, 1979], the exact mechanisms causing variations of the relativistic electrons are still not understood.

Here we report temporal (long time scale) and spatial ($1 < L < 9$) variability of the relativistic electron fluxes seen in drift loss cone with energetic particle sensor on board the CORONAS-I satellite. We concentrate mainly on the region around the location of the peak intensities and examine three relativistic electron injection events during time when satellite was in operation.

The illustration of the local bounce loss cone at 500 km is shown in Fig. 6.25. Particles at local pitch angles in the interval $\sim 66^\circ - 90^\circ$ are considered to be trapped (temporarily or stable). Because the width of this range is comparable with the field of view of the instrument - 30°, it samples both bounce and drift loss cone particles at the same time. Since the fluxes of electrons in the drift loss cone are steadier in time and generally much larger we believe that at locations where $h_{min} < 100$ km, mostly electrons in the drift loss cone are observed.

The great advantages of observing electrons in the drift loss cone are that all such electrons must have been injected only a short time before and that there is no stable population to mask the dynamics. The significance of the atmospheric drift loss cone for the study of acceleration and loss effects has been recently pointed out by *Blake et al.* [2001b,a].

6.3.1 $L - t$ Diagrams

Fig. 6.26 (top) shows the time history of the logarithm of daily averaged count rate of $0.5 - 1.5$ MeV electrons from day 94/64 until 94/184 in the interval of $1 < L < 9$ binned in bins $0.1L$. The measurements were taken only when CORONAS-I was in the drift loss cone and thus show only electrons with lifetimes of no more than a few tens of minutes. Thus we observe continuing injection and loss of relativistic electrons in the Earth's magnetosphere. Fig. 6.26 shows that there were several injections during the time of observation, with variable injection location and electron intensities. On the average these fluxes had a maximum value at $L = 3.8 - 4.6$. Note the $6 - 12$ MeV electrons also peak in this broad region. Substantial temporal variability of electron flux in the slot region and rather constant flux in the L range between 1 and 1.5 is also evident. The white vertical bars in the spectrogram plot means data missing for these days. They are shown to see the time coincidence with the gamma-ray profile. The energetic electron enhancements in the drift loss cone in the inner zone connected with geomagnetic storms during March-April 1994 on CORONAS-I have been studied by *Kuznetsov and Myagkova* [2002].

Similar variations of energetic electron fluxes ($E > 2$ MeV) were measured at geostationary orbit by GOES 7 satellite in the interval of March-May, 1994 [*Rostoker et al.*, 1998]. SAMPEX observation of $2 - 6$ MeV electrons from July 1992 to June 1999 demonstrate intense, 27-day recurrent electron acceleration events (due to high-speed solar wind streams) in 1993-1995 for $3 < L < 5$. Moreover, the most intense events were observed from mid-1993 through 1994 [*Baker et al.*, 2001].

It's known that near D_{st} minimum large convection electric fields are present and particle injections can occur. Following an injection the electrons are quickly transported inward by

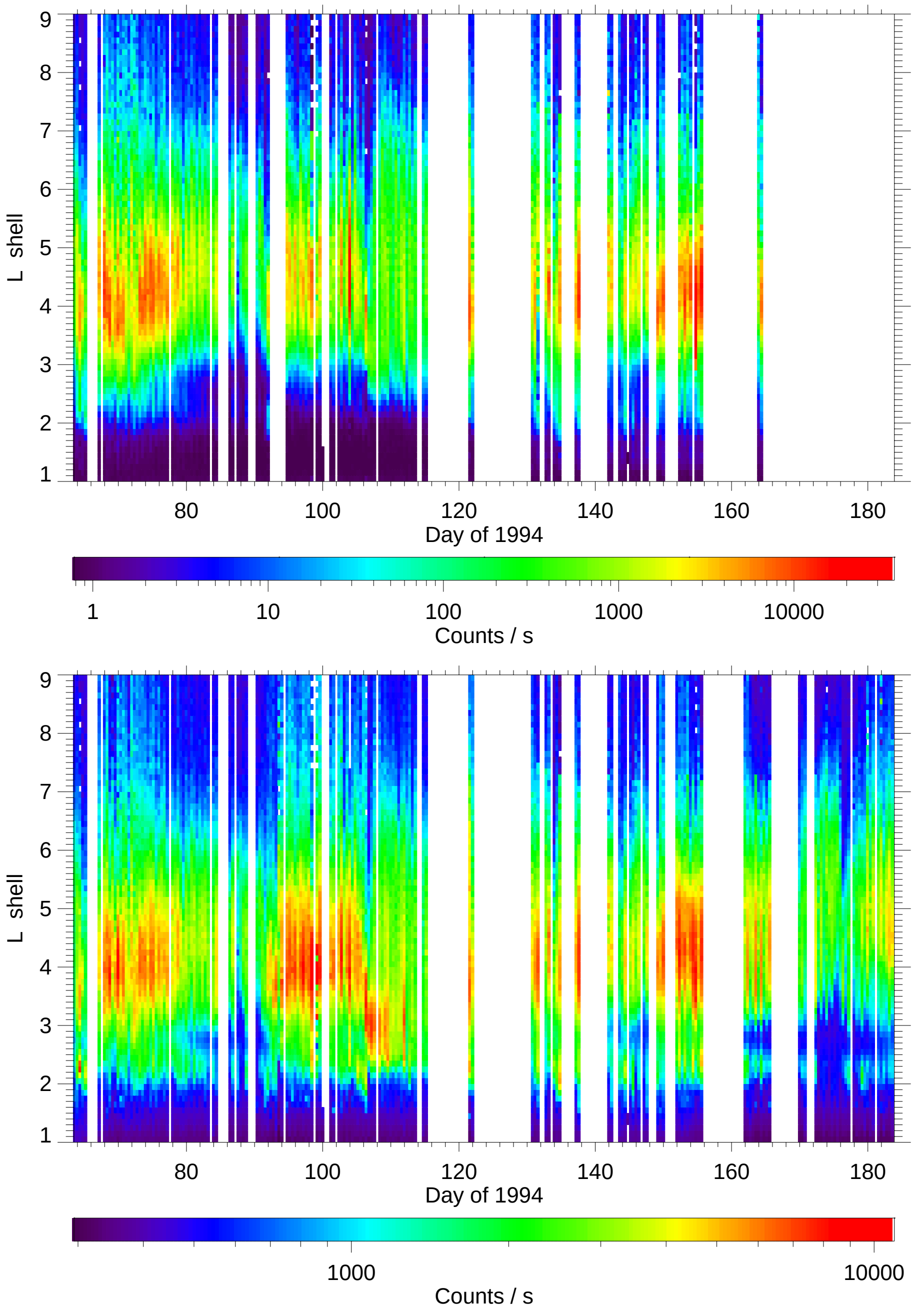

Figure 6.26. $L - t$ diagrams of drift loss cone MKL electrons in the energy range $0.5 - 1.5$ MeV (*top*) [from *Bučík et al.*, 2003b], and 0.12-0.32 MeV SONG gamma rays (*bottom*) during the four months period between 1994/64 and 1994/184 [from *Blake et al.*, 2002].

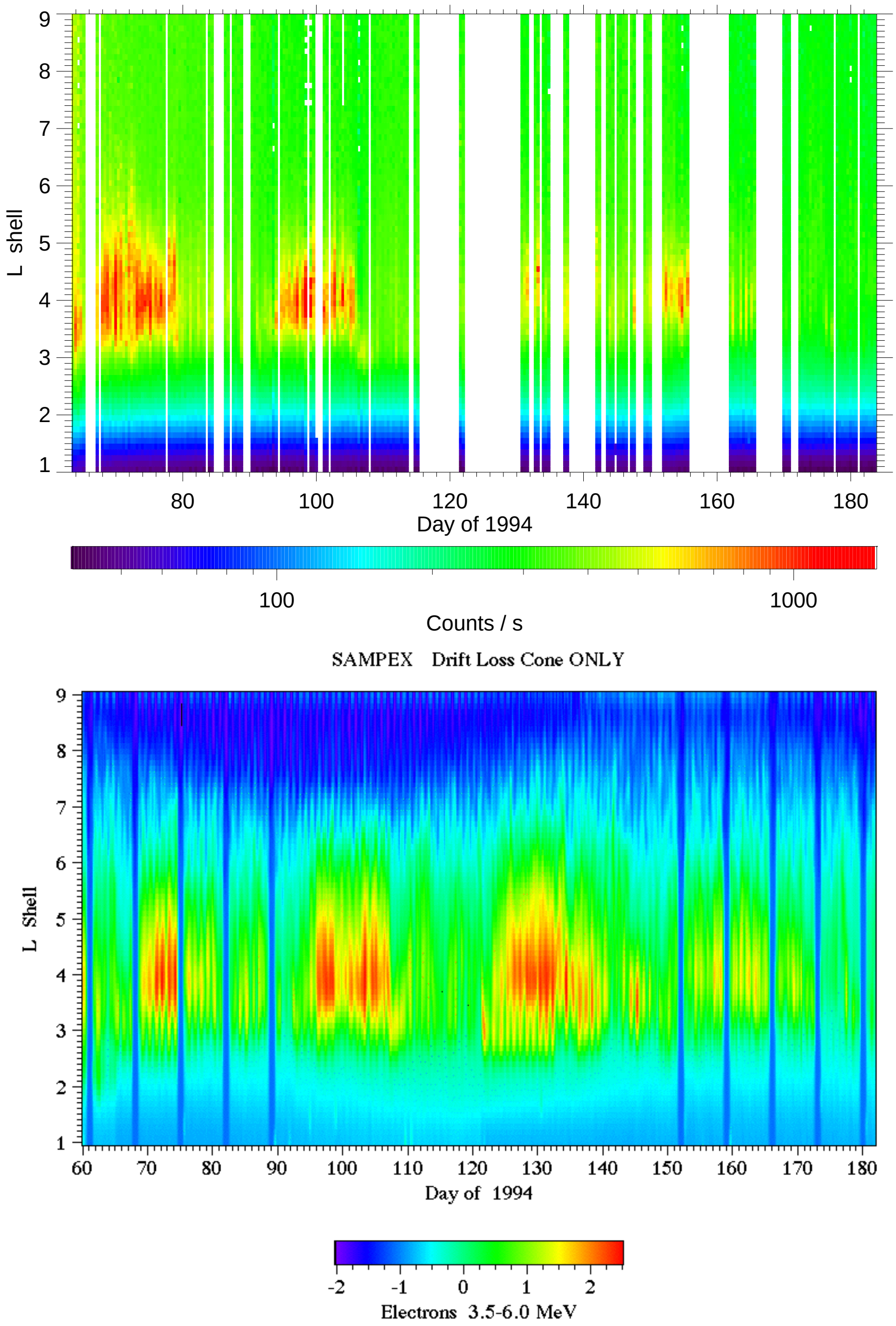

Figure 6.27. $L - t$ diagrams of drift loss cone CORONAS-I gamma rays in the energy range 3 – 8.3 MeV (*top*) and 3.5-6 MeV SAMPEX electrons in Spring of 1994 (*bottom*) [from *Blake et al.*, 2002].

radial diffusion. The electrons diffuse inward to an L value determined by the magnitude of the storm. After the electrons reach L values of $\sim 3.8 - 4.6$ their transport becomes much slower as their loss. Therefore electron flux peak near this location as can be seen in the Fig. 6.26. Observations also demonstrate the nearly simultaneous variation of the relativistic electrons over a large range of L values. The general $L - t$ pattern of the shape of the intensity peak in the drift loss cone has been discussed by *Blake et al.* [2001b], who suggests that newly energized electrons diffuse slowly both inward an outward in L from the peak location, broadening the injection peak with time. Once the acceleration ends, the flux continues the slowly decay. Slower diffusion and a large loss rate at lower L make broadening the injection peak to higher L much more prominent. This would explain the appearance of the relativistic electrons in higher L regions ($L > 5$). *Miyoshi et al.* [2003] studied the rebuilding process of outer belt relativistic electrons and proposed that the outward diffusion from acceleration region might coexist with the nonadiabatic acceleration in the whole outer belt.

Both Fig. 6.26 and Fig. 6.27 show that an excellent correlation exists between the parent electrons observed in the drift loss cone by SAMPEX and MKL and the daughter photons observed by CORONAS-I. This study suggests that it may be possible to monitor for space weather purposes the intensities of relativistic electrons in the radiation belt by remotely sensing MeV bremsstrahlung from a low-altitude spacecraft. For the future, there is need to examine more carefully time coincidence of photons from the atmosphere and local energetic electrons.

6.3.2 Variation in the Intensity Maximum

We focus mainly on two injection events which took place on March $6-8$, 1994 (designated as event 94065) and April $2-4$, 1994 (94092), and partially also on event on April 17, 1994 (94107). However, during the first two events we have bad temporal covering of the main phase of the related magnetic storms. The first half of 1994 was in the declining phase of the solar cycle approaching sunspot minimum, a time when recurrent high speed flows from coronal holes are though to drive magnetic storms [*Baker et al.*, 1986]. The analysis of the interplanetary medium parameters indicate that associated storm events 94065 and 94092 was connected with the magnetosphere passage across the boundary of a high-velocity

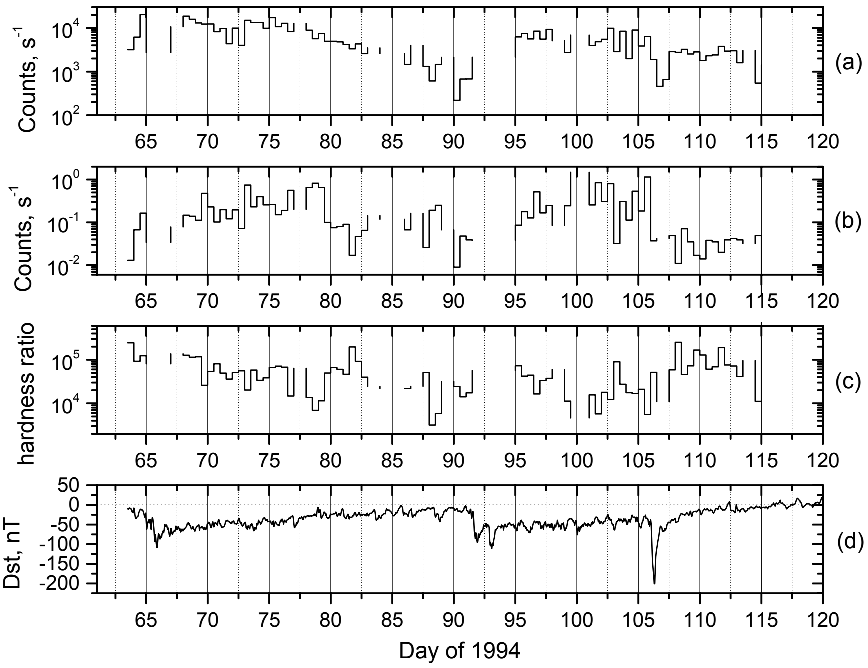

Figure 6.28. (*a, b*) the 12-hour-averaged 0.5 – 1.5 and 6 – 12 MeV electron fluxes in the drift loss cone plotted as a function of day number in 1994 at $L = 3.8 - 4.6$, (*c*) hardness ratio of the energy electron spectrum at $L = 3.8 - 4.6$, (*d*) D_{st} index [from *Bučík et al.*, 2003b].

solar wind streams and event 94107 was assumed to be induced by coronal mass ejection [*Kuznetsov and Myagkova*, 2002].

Fig. 6.28a and 6.28b show half-day averaged drift loss cone electron fluxes versus time at peak intensity location ($3.8 < L < 4.6$) in the energy ranges of $0.5 - 1.5$ and $6 - 12$ MeV. The electron albedo background, which dominates in $6 - 12$ MeV channel and disguises the injection events in high latitudes was subtracted from observed electron flux at $L = 3.8 - 4.6$. The temporal history of D_{st} is also plotted in Fig. 6.28 to show the relationship between D_{st} and the features of the electron injection events. Fig. 6.28c shows the variation of the electron energy spectra at $L = 3.8 - 4.6$. As a measure for the electron spectra we use count rate ratio between two MKL channels with energy ranges of $0.5 - 1.5$ and $6 - 12$ MeV.

It seems that response of the energetic electrons was the weakest for the event 94107

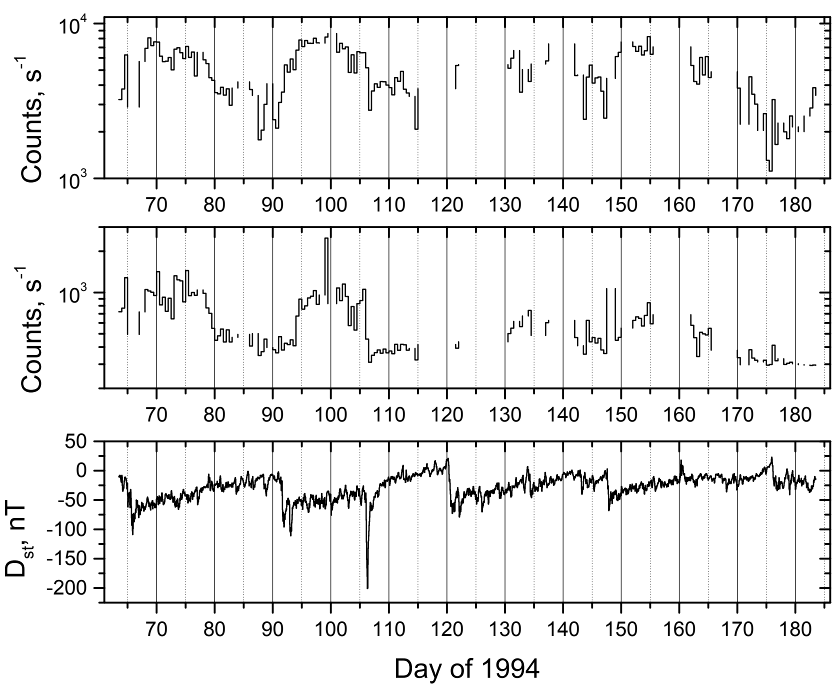

Figure 6.29. Half-day averaged DLC gamma-ray fluxes vs time at $L = 3.6 - 4.2$ in the energy ranges $0.12 - 0.32$ MeV (*top*) and $3 - 8.3$ MeV (*middle*).

although the D_{st} minimum reached value of -200 nT. In contrast, the strongest electron response was observed during the event 94065 with D_{st} minimum of -109 nT. Event 94092 has lower flux levels through over L range than event 94065, although those two storms have comparable D_{st} minimum. No simple relationship between the strength of a magnetic storm and the strength of the relativistic electron event has been reported by *Reeves* [1998]; *McAdams et al.* [2001]. In these works is concluded that the mechanism responsible for accelerating the relativistic electrons is not the same as the process that injects particles into the ring current.

The count rate plots in Fig. 6.28 shows that low energy electron flux in the drift loss cone reaches the maximum immediately after D_{st} storm main phase, whereas the high energy electron flux increased more gradually over several days. The subsequent gradual rise in the high energy electrons could be explained by inward radial diffusion. Recently, it has been suggested that energization is not due to diffusion alone, but that a local heating process (such as shock acceleration or wave-particle interactions) which does not converse the particle's magnetic moment have to be involved for the subsequent enhancements of the more energetic electrons [*Li et al.*, 1997; *Miyoshi et al.*, 2003].

As can be seen in Fig. 6.28c, the evolution of the energy spectrum during the magnetic storms is similar across all three storms regardless magnetospheric conditions. Immediately after main phase of the storm the spectra softened and during phase when D_{st} increased the spectra hardened. The spectral softening at the beginning of the storm 94065 is probably due to fact that less energetic electrons were continuously injected during the decrease of D_{st}. The gradual hardening of the electron spectrum up to day $\sim$ 80 could be explained by acceleration of seed electron population during their inward transport to lower L shells and/or local acceleration in the heart of radiation belt by plasma waves. As a storm progresses the abrupt hardening of energy spectra is probably due to higher rate of loss of low energy electrons and /or electron acceleration. It should be noted that in this study we ignore any magnetic local time variation in the electron fluxes. For example, at beginning of 94065-injection event, the CORONAS-I's orbit was near the dawn-dusk plane with consecutive orbit precession to noon-midnight meridian at onset of the next event (94092).

To show the relationship between MKL electrons and gamma-rays in the drift loss cone at the L shells where the maximum enhancements were observed the 12-hour-averaged $0.12 - 0.32$ and $3 - 8.3$ MeV gamma-ray fluxes in DLC are given in Fig. 6.29.

The dynamics of the energetic electrons during the studied period has never been yet thoroughly explored, neither in so relatively wide energy interval nor in such wide L shell range. A more quantitative study of the features of the variations in the fluxes of relativistic electrons and time coincidence with daughter gamma rays reviewed here is being undertaken.

Chapter 7

Conclusion

The initial and essential part of the present work was comprised to the production of the gamma-ray database (CD-archived) of measured fluxes by the SONG instrument on CORONAS-I. This database is given to the access of the international space science community. The packed of programs on computation satellite orbit and required geophysical parameters was developed. This packed has been recently used for data on CORONAS-F experiment.

Detailed spatial distribution of gamma-ray fluxes averaged within a four month period at 500 km altitude in geographic and magnetic invariant coordinates has been obtained. Two contributions are identified: by primary cosmic rays and charged albedo fluxes, and due to magnetospheric electrons.

7.1 Gamma Radiation by Primary Cosmic Rays

The intensity of the first component was found to be inversely proportional to the primary cosmic-ray cutoff rigidity. The presence of re-entrant albedo electrons at closed field lines at low latitudes seems to be one of the reasons of the hardness of this dependence in comparison with similar one for primary cosmic rays. The same fact can also partly explain softer gamma-ray energy spectra observed near the equator than at the pole. The prevalence of albedo charged particle flux near the equator in integral energy channel measuring electrons and protons with energy release of 70 MeV for protons and 55 MeV for electrons was also deduced from our measurements.

During the magnetic storms, charged albedo flux dominance can explain anomaly in Forbush decrease, which maximum was observed at equatorial region. The charged particle flux increase at middle latitudes at beginning of the magnetic storm was attributed to the local rigidity cutoff variation - its diamagnetic decrease due to ring current builds up. The possibility of the cosmic-ray variation study by detectors on high-inclination satellites was in the present work demonstrated.

The saturation of the $3-8.3$ MeV gamma-ray flux for $R < 1$ GV agrees with cutoff to the differential energy spectrum of primary cosmic rays at $E \leq 1$ GeV. The structure of rigidity cutoff distribution at altitude of 500 km in geographical map is similar to the $3-8.3$ MeV gamma-ray flux distribution. These are reasons why we believe that first detected component of gamma rays are secondary gamma radiation produced by primary cosmic rays in the Earth's atmosphere and flowing out to the satellite altitude with any unresolved local contribution. However, the local gamma rays seem to have a minor importance in observed gamma-ray flux. It was found the night-day asymmetry in detected gamma-ray intensity could be explained by the shadowing effect of the satellite body from the atmosphere, indirectly confirming that CORONAS-I gamma rays are mainly due to atmospheric gamma radiation.

The induced contribution due to primary cosmic-ray bombardment, which decreases the latitudinal effect for energies up to 3 MeV was estimated and subtracted from the gamma-ray flux in energy channel of $0.12-0.32$ MeV.

The distribution in $L-B$ coordinates showing the regular pattern of the atmospheric gamma rays of the cosmic origin is well-arranged according to the McIlwain's L parameter, quantity highly correlated with the geomagnetic cutoff.

7.2 Gamma Rays in Relation to the Magnetospheric Effects

We found that most intense fluxes, irregularly distributed at geographical maps lies at stable trapped zones. In $L-B$ coordinates enhanced fluxes concentrate into two areas, which correspond to the nominal location of the trapped radiation belts. The most intense is clustered into the inner radiation zone. Both inner and outer zone enhancements are separated by the region of the flux decreasing, corresponding to the slot region between the belts. In order to interpret gamma-ray fluxes in the magnetic coordinates, the trapped electron population in altitude-section in $L - B$ space of the Earth's magnetic field and electron longitudinal distribution in the loss cones have been modelled.

Detailed energy spectral characteristics of the gamma-ray flux in outer stable trapped zone show intensity peak between L shells of 3.5 and 4, where the power low spectral index has minimal value, indicating high energy part of the gamma-ray electron parents presents here. Time profile of the MKL electron spectrum in the DLC of the outer radiation belt manifests energization conected with the magnetic storms in March-June 1994 period. The significant contribution of albedo electrons to the formation of the trapped electron flux in the inner boundary of the outer radiation belt was gather from the spectral analysis. In the same part of the outer belt the gamma-ray spectral profile along the L shells copies the AE electron model one. Discrepancy at higher L-shells can be explained by not including the temporal variations in the model.

Similar energy spectral slopes between MKL, AE electrons and SONG gamma rays in outer and slot regions could also confirm that observed gamma-ray flux is mainly due to bremsstrahlung electrons as a only one effective production mechanism of low-energy gamma continuum in the Earth's environment. The simple test on the bremsstrahlung production by AE inner belt electrons in the limits of our simplification following from the production scheme and uncertainties in flux reconstruction is in good agreement with our observations, in those L, B positions where AE-8 model agrees with spatial pattern of the measured gamma-ray flux.

Mapping of the CORONAS-I MKL electron fluxes in energy ranges of $0.5 - 1.5$ MeV and $6 - 12$ MeV in geographic and $L - B$ coordinates and qualitative comparison with SONG $0.12 - 0.32$ MeV and $3 - 8.3$ MeV gamma-ray fluxes reveals the similarity in position of enhanced fluxes and similar pattern of the structure of spatial distribution of enhanced fluxes both in outer and inner radiation zones.

Temporal variability of the gamma rays at the atmospheric drift loss cone coincide with the D_{st} profile indicating couple of magnetic storms during the studied time interval. The coincidence with the SAMPEX and MKL relativistic drift loss cone electrons presents gamma rays as a good proxy for the population of the precipitating energetic electrons. No substantial time variable flux in the inner belt was observed, basically indicating the not strictly magnetospheric origin of the inner belt electrons.

In summary, based on our analysis the enhanced fluxes of gamma rays observed in inner radiation belt (SAA in geographical map) are artificial effect of the satellite and of the instrumental matter. In the outer radiation belt (high latitudes in localized region below SAA, and small area at north), and in the other intensity-enhanced regions, gamma rays are combination of both the Earth's atmosphere and the local matter (artificial) emissions.

We can conclude that the most intense fluxes of the low-energy ($0.1 - 10$ MeV) gamma rays in the near-Earth's space are present during the magnetic storms when the outer radiation belt electrons are precipitating into the Earth's atmosphere. However, these are only transient enhancements. The steady in time, the intense (less than previous one) gamma-ray flux was identified as an atmospheric gamma radiation due to primary cosmic rays and albedo charged particles. In satellite experiments on low-Earth polar orbit, the additional artificial intense gamma-ray flux is produced, most intense one is still present when satellite passes the stable trapped zone and temporary one at high latitudes during the magnetic storms.

7.3 Mass Distribution Around the Crystal

The matter distribution in the complex experimental setup around the CsI crystal of the SONG instrument on CORONAS-I satellite has been modeled. The methods of the solid angle calculation and Monte Carlo average mass thickness estimation have been developed, giving the possibility to calculate mean matter in various directions, and with variable size of the solid angle. However, accuracy of the proposed model is limited by knowing of the real mass distribution in whole space around the detecting crystal. We select the six solid segments supposing (the density variation in the surrounding instruments was unknown in the present study) having the most different mass density. Specifying the position of the detecting element (CsI crystal), and values of the masses and dimensions of the ambient objects, the detector shielding for the present CORONAS-F experiment can be evaluated.

Knowing the average mass thickness distribution in the different six solid angles the nominal 4π detector FOV was qualified and for local bremsstrahlung production the simulated mass thickness was used.

Appendix A

Estimate of the Index γ by Least Squares Method

Minimizing

$$\sigma^2 = \frac{\sum_{i=1}^{n}(y_i - y(x_i))^2}{n-2}, \tag{A.1}$$

where $y \propto x^{-\gamma}$ presents simple power low model, we obtain

$$\gamma = \frac{n\sum_{i=1}^{n} X_i Y_i - \sum_{i=1}^{n} Y_i \sum_{i=1}^{n} X_i}{n\sum_{i=1}^{n} X_i^2 - \left(\sum_{i=1}^{n} X_i\right)^2}, \tag{A.2}$$

where $X_i = \ln x_i$, and $Y_i = \ln y_i$. The quality of the fit is determined by the coefficient of determination:

$$r^2 = 1 - \frac{\sum_{i=1}^{n}(y_i - y(x_i))^2}{\sum_{i=1}^{n}(y_i - \bar{y})^2}. \tag{A.3}$$

Uncertainty in estimate of parameter γ is characterized by standard error of estimate:

$$\sigma_\gamma = \frac{\sigma}{\sqrt{\sum_{i=1}^{n}(x_i - \bar{x})^2}}. \tag{A.4}$$

In more reliable approach the minimizing quantity should be

$$\chi^2 = \sum_{i=1}^{n}\left(\frac{y_i - y(x_i)}{\sigma_i}\right)^2, \tag{A.5}$$

where σ_i are know standard deviations (measurements errors). This quantity has χ^2 distribution with $n-2$ degrees of freedom if y_i follows Gaussian distribution.

Appendix B

On Mass in 4π Solid Angle Around SONG CsI Scintillator Aboard CORONAS-I Satellite

The complex geometric setup around the SONG CsI scintillator aboard the CORONAS-I satellite is modeled, to evaluate the mass thickness passed through by the cosmic ray particle striking the detector.

B.1 Instruments Setup

A schematic configuration of the scientific equipment on the spacecraft instrument platform is shown in Fig. B.1. Fig. B.1a displays view from the front -parallel to the longitudinal satellite X-axis, and Fig. B.1b view from the side -parallel to the satellite Y-axis. The forward end of the satellite body is indicated on the bottom of Fig. B.1b. Due to the large linear size of some devices in the direction to the Sun, the instruments were situated in the holes on the plate to minimize their inertia moments relatively to the plate.

A list of all devices on the instrument platform and their corresponding masses are provided in Tab. B.1. Notice that the masses of devices number 15 and 16 have been only estimated as a product of their approximate volume and mean device density. The last quantity is evaluated in the next section.

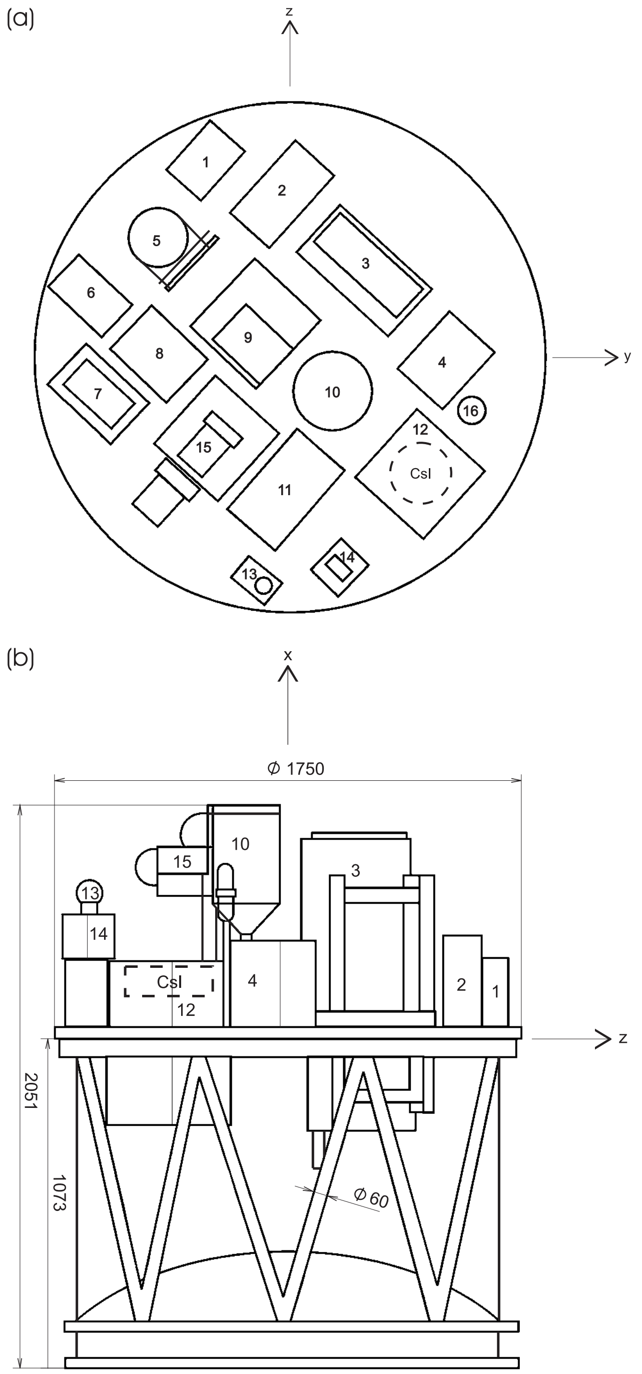

Figure B.1. Configuration of the scientific equipment on the instrument platform of the CORONAS-I satellite. (a) view from the front (normal view of y-z plane), (b) view from the side (normal view of x-z plane) [from *Bučík and Kudela*, 2003].

B.2 Model Description

B.2.1 Model of the Mass Around the CsI

Devices on the Platform

The layout of all devices around the CsI on the upper platform was modeled by two homogeneous right circular cylinders: (1) cylinder located in the hemisphere above the center of the CsI and designated as C1 and (2) cylinder located in the opposite hemisphere and designated as C2. All we need now are the radii, heights and densities of the proposed cylinders.

To obtain the mean cylinder density we need to know the mass m_i and the volume V_i of the ith instrument or its part lying in the upper or lower hemispheres (uh or lh) according to equation

$$\varrho = \frac{\sum m_i}{\sum V_i} \tag{B.1}$$

Unfortunately, the devices dimensions are not readily available (except for the SONG instrument), so we take their from the sketch (Fig. B.1). Moreover, only several instrument heights (vertical dimensions) are visible in Fig. B.1b. Therefore, the calculated cylinder density presents only crude approximation. The measurements obtained from Fig. B.1 are summarized in Tab. B.2. The labels of the visible instruments in Fig. B.1b are shown in the column 2. The normally viewed surface area S_i (column 3) was taken from Fig. B.1a and was considered the area of the base of the ith instrument on the platform. The fractional volume V_i has been computed as the product $S_i h_i$. The instrument heights were taken from Fig. B.1b. Our simplifications suppose the homogeneity (i.e. constant density across the body) of all devices on the instrument platform. Under this assumption the fractional device mass m_i has been estimated to be proportional to the device height h_i in the particular hemisphere. By eqn. B.1, $\varrho_1 = 0.28872$ g cm^{-3} and $\varrho_2 = 0.34499$ g cm^{-3}, the densities of the cylinders C1 and C2, respectively. Data given in Tab. B.2 can also provide the overall mean device density on the instrument platform.

Since we have no information about the heights of other devices than those given in Tab. B.2 we only evaluate their possible maximal values. Taking into account the device

Label	Name	Mass (kg)
1	DIAGENNESS-BF	5.4
2	DIAGENNESS-BS	7.8
3	TEREK-BD	38.0
4	TEREK-BE2	7.5
5	VUSS	18.5
6	IRIS BV2	6.3
7	IRIS BV1	8.0
8	RES-K-BE2	7.5
9	RES-K-BD	37.2
10	GELIKON-D1	12.3
11	GELIKON-E	7.4
12	SONG-D	44.7
13	DIFOS-BF	4.1
14	SURF	3.6
15	The satellite service system	34.1
16	Thermodetector	1.8
$\sum$		244.2

Table B.1. A list of all devices on the upper platform and their respective masses [from *Bučík and Kudela*, 2003].

arrangement on the upper platform (see Fig. B.1) we get the following set of relations:

$$h_5 \leq h_1, h_6 \leq h_2, h_{7,8,9} \leq h_4, h_{15} \leq h_{10}, h_{11} \leq h_{12}, \tag{B.2}$$

where h_j indicates the height of the jth instrument and j refers to the instrument label on the platform.

Knowing the area of the cylinder base, we can determine the radius of the right circular cylinder. The areas of the bases of all devices on the instrument platform, which are listed

			h_i (cm)		V_i (cm^3)		m_i (kg)	
i	Label	S_i (cm^2)	uh	lh	uh	lh	uh	lh
1	1	470.5	9.8	19.6	4602	9203	2.1	3.3
2	2	718.4	19.6	19.6	14051	14051	3.9	3.9
3	3	1181.3	60.8	63.0	71887	74453	18.7	19.3
4	4	661.7	17.4	19.6	11504	12942	3.6	3.9
5	12	1225.0	.0	54.3	0	66558	.0	30.7
6	13	163.8	41.3	19.6	6765	3204	2.8	1.3
7	14	231.1	28.3	19.6	6528	4519	2.2	1.4
$\sum$					115337	184930	33.3	63.8

Table B.2. Summary of observations from Fig. B.1 [from *Bučík and Kudela*, 2003].

in Tab. B.3 (the second column) have been evaluated from Fig. B.1a. By summing up all these values, we find the area of the base of the cylinder C2. In case of the cylinder C1 we must exclude the areas of the bases of the devices labeled as 11 and 12, which entirely lie in the lower hemisphere. The calculated values of the radii are $r_1 = 53.19$ cm for C1 and $r_2 = 59.31$ cm for C2.

Tab. B.3, column 3, gives the fractional instrument masses in the lower hemisphere, assuming again to be proportional to their respective heights. In case of the hidden devices in Fig. B.1b, their heights have been taken according to the relations in (B.2). The last value in the rightmost column presents the mass m_2 of the cylinder C2. The mass m_1 of the cylinder C1 is found as follows.

$$m_1 = m_t - m_2 - m_{CsI}, \tag{B.3}$$

where m_t is the total mass of devices on the instrument platform (given in Tab. B.1) and $m_{CsI} = 14$ kg is the mass of the CsI crystal.

Label	S_i (cm^2)	m_i (kg)
1	470.5	3.3
2	718.4	3.9
3	1181.3	19.3
4	661.7	3.9
5	427.6	11.4
6	433.5	3.2
7	672.2	4.2
8	548.2	3.9
9	1225.0	19.2
10	668.1	2.5
11	937.7	7.4
12	1225.0	30.7
13	163.8	1.3
14	231.1	1.4
15	1405.6	8.9
16	81.1	0.5
$\sum$	11050.8	125.0

Table B.3. The summary of the areas S_i of device bases on the upper plate and the fractional instrument masses m_i in the lower hemisphere [from *Bučík and Kudela*, 2003].

The height of the right circular cylinder is given by

$$h = \frac{m}{S\varrho} = \frac{m}{2\pi r\varrho}, \tag{B.4}$$

where S, r, ϱ and m have their common meaning. Eqn. B.4 yields the following cylinder heights: $h_1 = 40.99$ cm for C1 and $h_2 = 32.79$ cm for C2.

Instrument Platform

The cylindrical aluminium platform (designated as C3) has 175 cm diameter and 1.2 cm height. Its calculated approximate mass m_3 has value of 78 kg.

Vehicle and Rest Mass

The cylindrical vehicle itself, the solar panels, antennas and instruments on the opposite end of the satellite were simulated by the right circular homogeneous cylinder (labeled as C4) with diameter of 2.3 m and height of 2.94 m . Knowing the values of its volume and mass (1978 kg), we have a mean density of 0.16193 g cm^{-3}. The mass of the proposed cylinder C4 was taken approximately to be

$$m_4 = M - m_t - m_3, \tag{B.5}$$

where M is the spacecraft mass (2300 kg), and m_t and m_3 have their previous meaning.

B.2.2 Model of Geometry Configuration

The proposed model of the geometrical setup of the matter distribution around the CsI crystal is shown in Fig. B.2. The origin O of our reference system (a right-handed Cartesian coordinate system) is placed at the center of the CsI. Fig. B.2a is the front view (parallel to the z-axis), and Fig. B.2b is the cross sectional view (parallel to the x-axis). The center of the CsI crystal was located at a distance of 22.5 cm from the instrument platform and 129.8 cm from the vehicle, respectively. The offset of the CsI center from the vehicle and platform common axis was 56.5 cm.

CsI Solid Angles

In configuration according to Fig. B.2 we evaluate the solid angles subtended by the satellite body, instrument platform and both cylinders modeling the device arrangement on the platform. Consider first the vehicle and the instrument platform.

The solid angle Ω subtended by a surface A, in spherical coordinates, is given by

$$\Omega = \iint_A \sin\theta \mathrm{d}\phi \mathrm{d}\theta, \tag{B.6}$$

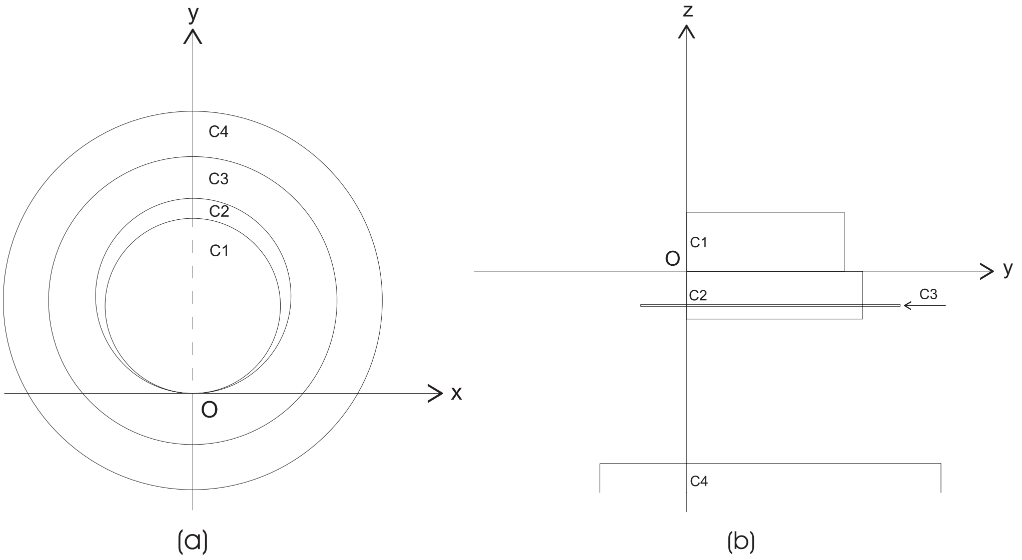

Figure B.2. Schematic of the model of the geometrical arrangement of the cylinders C1, C2, C3, and C4 [from *Bučík and Kudela*, 2003].

where θ is the polar angle and ϕ is the azimuth. Consider the base of the cylinder C3 or C4 with the center $S(0, y_S, z_S)$ and the radius r shown in Fig. B.3 and assume that the origin O is located at the CsI center. Refer to Fig. B.3, the surface A is bounded by a circle $x^2 + (y - y_S)^2 = r^2$. Written in spherical coordinates we have

$$\rho = \frac{y_S \sin\phi + \sqrt{r^2 - y_S^2 \cos^2\phi}}{\sin\phi}. \tag{B.7}$$

The range of ϕ is from 0 to 2π . To find the range of θ we replace ρ with $z_S / \cos\theta$. Then

$$\tan\theta = \frac{y_S \sin\phi + \sqrt{r^2 - y_S^2 \cos^2\phi}}{z_S}. \tag{B.8}$$

Applying eqn. B.6 we obtain the following:

$$\begin{aligned}\Omega &= \int\limits_0^{2\pi} \mathrm{d}\phi \int\limits_0^{\arctan((\mathrm{y_S} \sin\phi + \sqrt{\mathrm{r}^2 - \mathrm{y_S^2} \cos^2\phi})/\mathrm{z_S})} \sin\theta \mathrm{d}\theta \\ &= 2\pi - \int\limits_0^{2\pi} \cos\left(\arctan\frac{y_S \sin\phi + \sqrt{r^2 - y_S^2 \cos^2\phi}}{z_S}\right) \mathrm{d}\phi.\end{aligned} \tag{B.9}$$

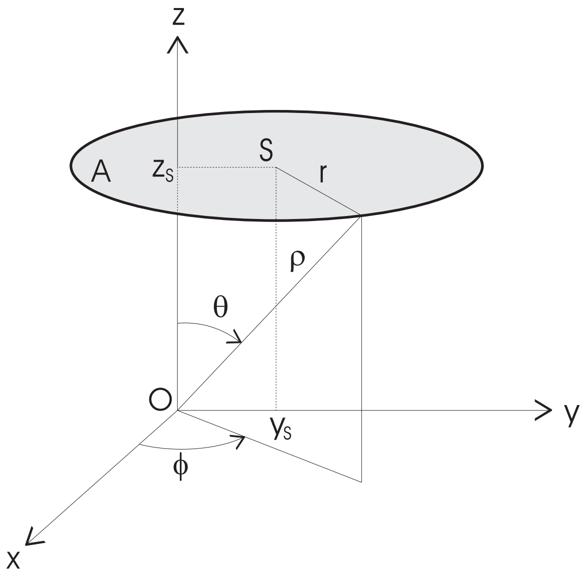

Figure B.3. The coordinate system in which the area A of the base of the right circular cylinder is defined [from *Bučík and Kudela*, 2003].

The last integral has been solved numerically by the Romberg's method [e.g. *Ralston and Rabinowitz*, 1978] with a relative error less than 10^{-6}, using the IDL [1992] routine NR_QROMB[1]. Thus, the solid angles subtended by the satellite body and the instrument platform are 0.45232π sr and 1.30588π sr, respectively. Note that the meaning of the constants y_S, z_S and r are the offset of the cylinder axis, distance between center of the CsI and the cylinder base, and the radius of the cylinder, respectively. All these quantities have been previously evaluated. Recall that the solid angle corresponding to the half hemisphere equals 1π steradians. Refer to Fig. B.2, the cylinder C1 entirely lies in one half hemisphere and due to its special position, the solid angle being subtended is 1 sr. This is also case of the cylinder C2.

B.3 The Average Mass Thickness in the Modeled Absorbers

In this section we evaluate the average mass thickness (in g cm^{-2}) in all suggested cylinders through which the cosmic ray particle must travel in order to reach the point detector (the

---

[1] NR_QROMB is based on the routine `qromb` described in section 4.3 of Numerical Recipes in C: The Art of Scientific Computing [*Press et al.*, 1992].

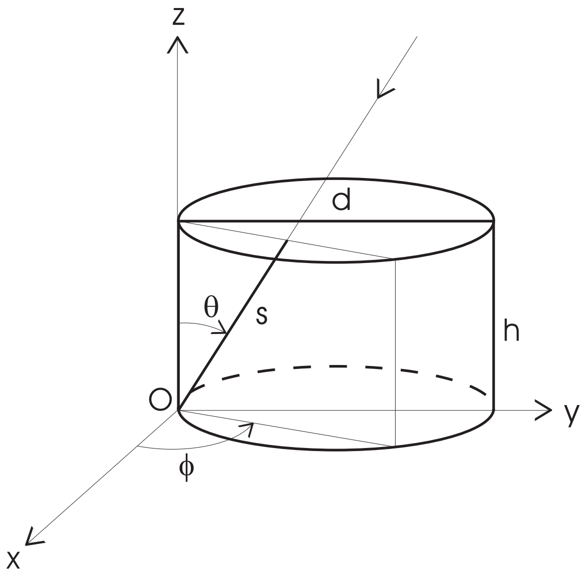

Figure B.4. The geometry used in deriving the pathlength $s(\theta, \phi)$ traversed in the cylinders C1 and C2 [from *Bučík and Kudela*, 2003].

center of CsI). Due to proposed homogeneity of the simulated cylinders we deal with the pathlengths expressed in cm. Furthermore, the isotropy in propagating of the cosmic ray particles is supposed and for simplicity trajectories are assumed to be straight lines. The statement of the problem suggests using a Monte Carlo simulation.

B.3.1 Cylinders C1 and C2

Shown in Fig. B.4, consider the right circular cylinder with the diameter d and the height h. Let the point detector be located at the origin O. The direction of incidence of the cosmic ray particle is defined by spherical coordinates (θ, ϕ). The range of ϕ is $(0, \pi)$, and of θ $(0, \frac{\pi}{2})$. The pathlength of the trajectory that traverse the cylinder may be expressed as:

$$s(\theta, \phi) = \begin{cases} \frac{h}{\cos\theta} & \text{if } 0 < \theta \leq \arctan\frac{d\sin\phi}{h}, \\ \frac{d\sin\phi}{\sin\theta} & \text{otherwise.} \end{cases} \tag{B.10}$$

Assumed isotropy of the radiation implies the uniform frequency distribution of directions of incidence $D(\theta, \phi)$. The average pathlength $\bar{s}$ is given by the first moment of the incident direction distribution.

$$\bar{s} = \iint s(\theta, \phi) D(\theta, \phi) \mathrm{d}\theta \mathrm{d}\phi \tag{B.11}$$

Above integral has been solved by the Monte Carlo technique [e.g. *Buslenko and Schreyder*, 1961]. Its essential basis is the Strong Law of Large Numbers (SLLN) and the Central Limit Theorem (CLT).

The Khintchine SLLN assures that for n sufficiently large,

$$\bar{s} \approx \frac{1}{n} \sum_{i=1}^{n} s(\theta_i, \phi_i) \equiv \frac{1}{n} \sum_{i=1}^{n} s_i \equiv \bar{s}_n, \tag{B.12}$$

with probability close to one, when s_i are n independent, identically distributed (idd) random variables with finite mean $\bar{s}$. Here $\bar{s}_n$ is the sample mean and

$$\sigma_n^2 = \frac{n}{n-1} \left(\frac{1}{n} \sum_{i=1}^{n} s_i^2 - \bar{s}_n^2 \right) \tag{B.13}$$

is the sample variance. Moreover, by the CLT, as n tends to infinity,

$$\frac{\bar{s}_n - \bar{s}}{\sigma} \sqrt{n} \tag{B.14}$$

approaches a standard Gaussian distribution, provided that σ (which is the standard deviation of a sequence idd random variables $s_1, s_2, \ldots, s_n$), is finite and not zero. Finally, the maximum error ε of the estimate of the mean pathlength, under 95% chance of covering the value of $\bar{s}$, is given by

$$\varepsilon = 1.96 \frac{\sigma_n}{\sqrt{n}}, \tag{B.15}$$

where the population standard deviation σ is replaced by its consistent estimator σ_n.

The general procedure that we used may be outlined as follows:

(i) Choose number of trials (or trajectories) n, e.g. 1000 and preliminary compute $\bar{s}_n$ and σ_n by eqn. B.12 and B.13 respectively.

(ii) Choose relative accuracy, e.g. 10^{-2} and find the approximate sample size n by

$$n > \left[\frac{1.96 \sigma_n}{10^{-2} \bar{s}_n} \right]^2. \tag{B.16}$$

Cylinder	$\bar{s}_n\varrho$	$\sigma_n\varrho$	$\varepsilon\varrho$
C1	15.60	7.04	0.16
C2	17.04	9.08	0.17

Table B.4. The results of the simulation of mass thickness for the cylinders C1 and C2 [from *Bučík and Kudela*, 2003].

(iii) According to the step (ii) use n to compute $\bar{s}_n$ (eqn. B.12) as an unbiased estimate of true (population) mean pathlegth $\bar{s}$ with desired relative accuracy, and σ_n^2 (eqn. B.13) as an unbiased estimator of variance σ^2 of the pathlengths about their population mean value.

(iv) Calculate the average mass thickness (g cm^{-2}) as a product of the mean cylinder density ϱ (g cm^{-3}) and mean pathlength $\bar{s}$ (cm) traversed in the cylinder.

The heart of the problem is computing s_i. This is done as follows:

(i) Choose a random trajectory striking the detector. Let ξ_1 and ξ_2 be two pseudorandom deviates drawn uniformly on $(0, 1)$, then

$$\phi = \xi_1 \pi \quad \text{and} \quad \theta = \xi_2 \frac{\pi}{2}$$

define the direction of incidence.

(ii) In this direction calculate pathlength s_i (eqn. B.10).

(iii) Repeat steps (i), (ii) n times.

In this paper, all random deviates are generated using the IDL routine RANDOMU, which generates pseudorandom numbers uniformly distributed in the interval $(0, 1)$.

The results for both cylinders C1 and C2 are summarized in Tab. B.4, and the mass thickness distributions are shown in Fig. B.5. The table lists the average mass thickness $\bar{s}_n\varrho$, the (sample population) standard deviation $\sigma_n\varrho$, and the 1.96σ statistical uncertainty $\varepsilon\varrho$. All quantities are multiplied by ϱ to obtain results in g cm^{-2}. The apparent bimodal

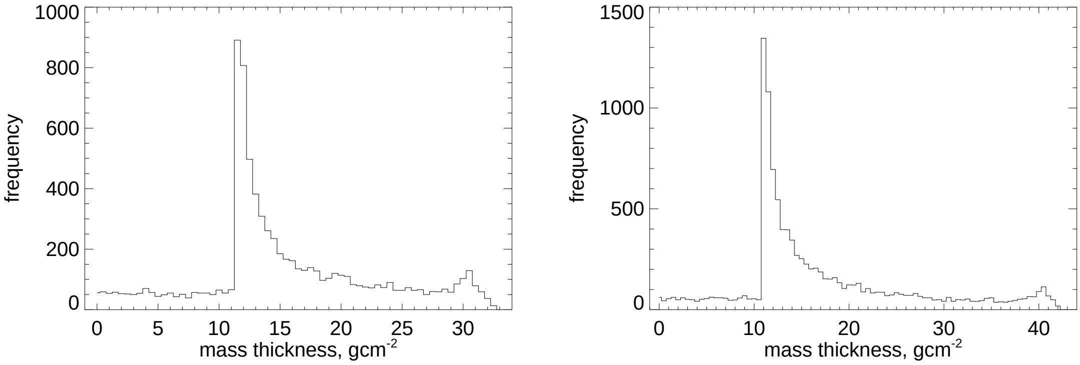

Figure B.5. Mass thickness distributions in the cylinders C1 (*left*) and C2 (*right*) for 7905 (C1), 10988 (C2) trajectories [from *Bučík and Kudela*, 2003].

distribution structure is the property of the proposed cylindrical shape and depends upon the ratio of the diameter to the height.

The fundamental disadvantage of the simple Monte Carlo integration is that its accuracy increases only as the square root of n, the number of sampled points. To achieve higher accuracy the more advanced techniques of Monte Carlo integration (called *reduction of variance* in the literature) are available. Due to simplifications involved in the outlined problem we believe that our requirements on accuracy are quite sufficient.

Note, if the direction of cosmic ray particle is specified then the problem can be modified by modeling of the incident direction density $D(\theta, \phi)$ by the Gaussian distribution.

B.3.2 Cylinders C3 and C4

Shown in Fig. B.6, consider the right circular cylinder with the radius r and height h. Let b denote the offset of the cylinder axis from the origin O, and let l be the distance between the cylinder lower base and the x-y plane.

The pathlength in the cylinder in Fig. B.6 may be expressed as:

$$s(\theta, \phi) = \begin{cases} \frac{h}{\cos\theta} & \text{if } 0 < \theta \le \arctan\frac{\delta}{h+l}, \\ \frac{\delta}{\sin\theta} - \frac{l}{\cos\theta} & \text{otherwise} \end{cases} \tag{B.17}$$

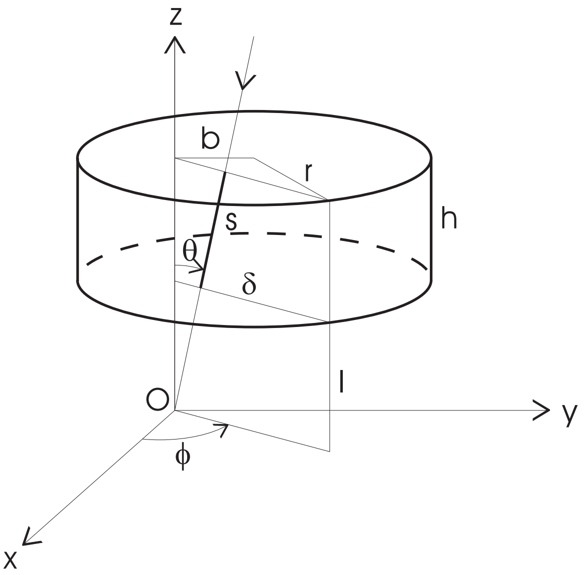

Figure B.6. The geometry used in deriving the pathlength $s(\theta, \phi)$ traversed in the cylinders C3 and C4 [from *Bučík and Kudela*, 2003].

Cylinder	$\bar{s}_n \varrho$	$\sigma_n \varrho$	$\varepsilon \varrho$
C3	4.75	2.29	0.05
C4	29.00	18.08	0.29

Table B.5. The results of the simulation of mass thickness for the cylinders C3 and C4 .

with

$$\delta = b \sin \phi + \sqrt{r^2 - b^2 \cos^2 \phi} \tag{B.18}$$

(cf. eqn. B.8). The range of ϕ is $(0, 2\pi)$, and of θ $(0, \arctan \frac{\delta}{l})$.

The random direction of incidence is defined by

$$\phi = \xi_1 2\pi \quad \text{and} \quad \theta = \xi_2 \arctan \frac{\delta}{l}.$$

The results of the simulation are summarized in Tab. B.5, and mass thickness distributions are shown in Fig. B.7.

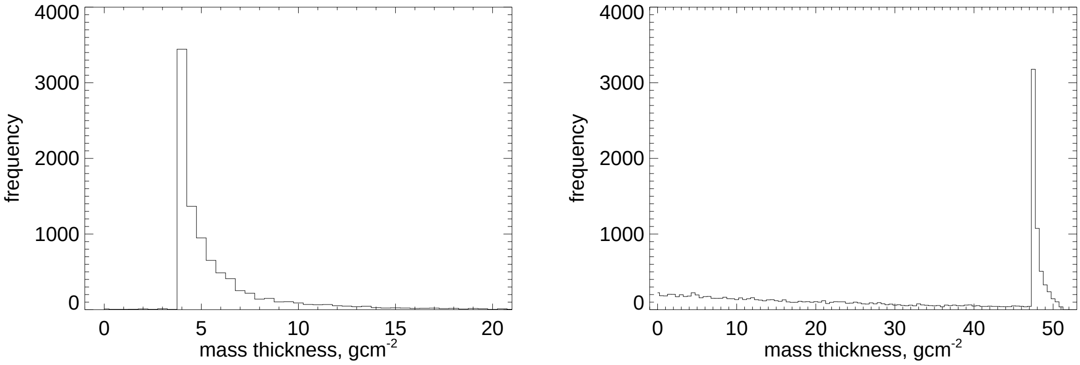

Figure B.7. Mass thickness distributions in the cylinders C3 (*left*) and C4 (*right*) for 9079 (C3), 15214 (C4) trajectories [from *Bučík and Kudela*, 2003] .

B.4 Mass Thickness in Space Around Detector

In this section we find the functional form describing the mass thickness over the whole space around the point detector. We consider this as a rough approximation of true mass thickness near the SONG CsI scintillator on CORONAS-I. For practical application we also evaluate the mean amount of matter in the selected solid angles by the method developed in the preceding section.

B.4.1 The mass thickness definition

Shown in Fig. B.8, consider the model of geometry in the region of the point detector introduced in Section B.2.2. To be more illustrative we diagrammatically give (Fig. B.9) an azimuth dependence of the polar angles subtended by the modeled cylinders. In configuration depicted in Fig. B.8, the amount of matter (in g cm^{-2}) traversed by the cosmic ray particle striking the detector, located at the origin O of our reference system, may be

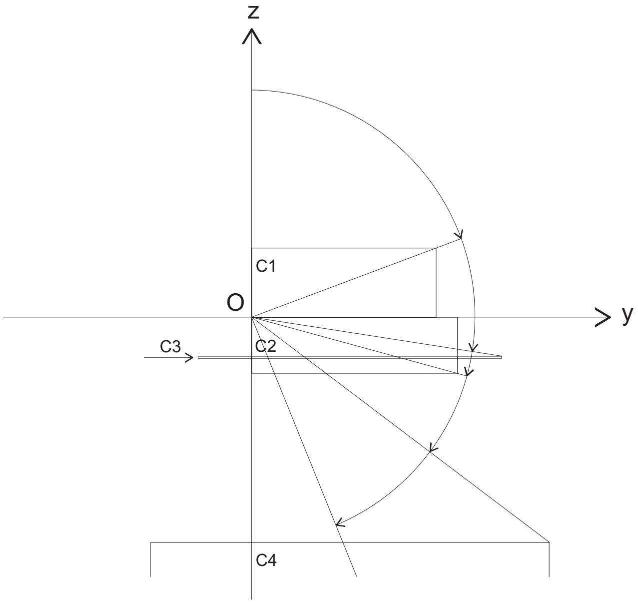

Figure B.8. A model of geometry in the region of the CsI scintillator (introduced in Section B.2.2). The polar angles subtended by the bases of the modeled cylinders are denoted as θ_1 (upper base of C1), θ_2 (upper base of C3), θ_3 (lower base of C3), θ_4 (upper base of C4), θ_5 (lower base of C2), and θ_6 (lower base of C4) [from *Bučík and Kudela*, 2003].

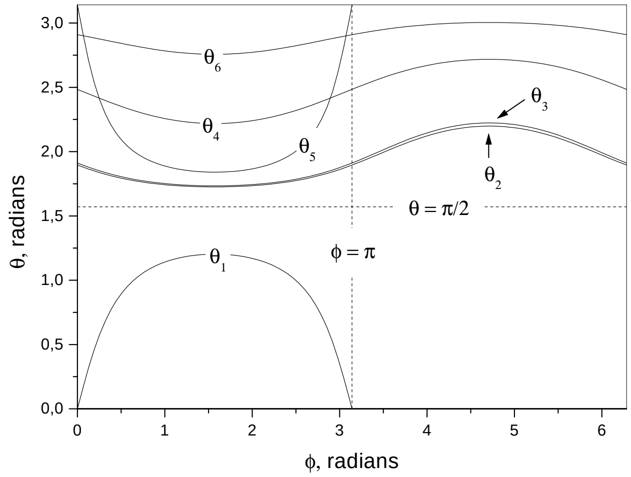

Figure B.9. A schematic diagram showing how polar angles subtended by cylinder bases depend on azimuth ϕ [from *Bučík and Kudela*, 2003].

expressed as:

$$s(\theta,\phi)=\begin{cases}
\eta_1 & 0 < \theta \leq \theta_1 \quad 0 < \phi \leq \pi \\
\nu_1 & \theta_1 < \theta \leq \frac{\pi}{2} \quad 0 < \phi \leq \pi \\
0 & 0 < \theta \leq \frac{\pi}{2} \quad \pi < \phi < 2\pi \\
\nu_2 & \frac{\pi}{2} < \theta \leq \theta_2 \quad 0 < \phi \leq \pi \\
0 & \frac{\pi}{2} < \theta \leq \theta_2 \quad \pi < \phi < 2\pi \\
\nu_2+\tau_3 & \theta_2 < \theta \leq \theta_3 \quad 0 < \phi \leq \pi \\
\tau_3 & \theta_2 < \theta \leq \theta_3 \quad \pi < \phi < 2\pi \\
\nu_2-\eta_3 & \theta_3 < \theta \leq \theta_4 \quad 0 < \phi \leq \phi_1 \vee \phi_2 < \phi \leq \pi \\
-\eta_3 & \theta_3 < \theta \leq \theta_4 \quad \pi < \phi < 2\pi \\
\nu_2-\eta_3 & \theta_3 < \theta \leq \theta_5 \quad \phi_1 < \phi \leq \phi_2 \\
\nu_2-\eta_3+\tau_4 & \theta_4 < \theta \leq \theta_6 \quad 0 < \phi \leq \phi_3 \vee \phi_4 < \phi \leq \pi \\
\nu_2-\eta_3+\tau_4 & \theta_4 < \theta \leq \theta_5 \quad \phi_3 < \phi \leq \phi_1 \vee \phi_2 < \phi \leq \phi_4 \\
-\eta_2-\eta_3+\tau_4 & \theta_5 < \theta \leq \theta_6 \quad \phi_3 < \phi \leq \phi_1 \\
-\eta_2-\eta_3+\tau_4 & \theta_4 < \theta \leq \theta_6 \quad \phi_1 < \phi \leq \phi_2 \\
-\eta_3+\tau_4 & \theta_4 < \theta \leq \theta_6 \quad \pi < \phi < 2\pi \\
\nu_2-\eta_3-\eta_4 & \theta_6 < \theta \leq \theta_5 \quad 0 < \phi \leq \phi_3 \vee \phi_4 < \phi \leq \pi \\
-\eta_2-\eta_3-\eta_4 & \theta_6 < \theta < \pi \quad \phi_3 < \phi \leq \phi_4 \\
-\eta_3-\eta_4 & \theta_6 < \theta < \pi \quad \pi < \phi < 2\pi
\end{cases} \tag{B.19}$$

with

$$\eta=\varrho\frac{h}{\cos\theta},\ \nu=\varrho\frac{d\sin\phi}{\sin\theta},\ \text{and}\ \tau=\varrho\left(\frac{\delta}{\sin\theta}-\frac{l}{\cos\theta}\right),$$

and

$$\theta_1=\arctan\nu_1,\ \theta_2=\pi-\arctan\frac{\delta_3}{l_3},\ \theta_3=\pi-\arctan\frac{\delta_3}{l_3+h_3},$$

$$\theta_4=\pi-\arctan\frac{\delta_4}{l_4},\ \theta_5=\pi-\arctan\nu_2,\ \theta_6=\pi-\arctan\frac{\delta_4}{l_4+h_4},$$

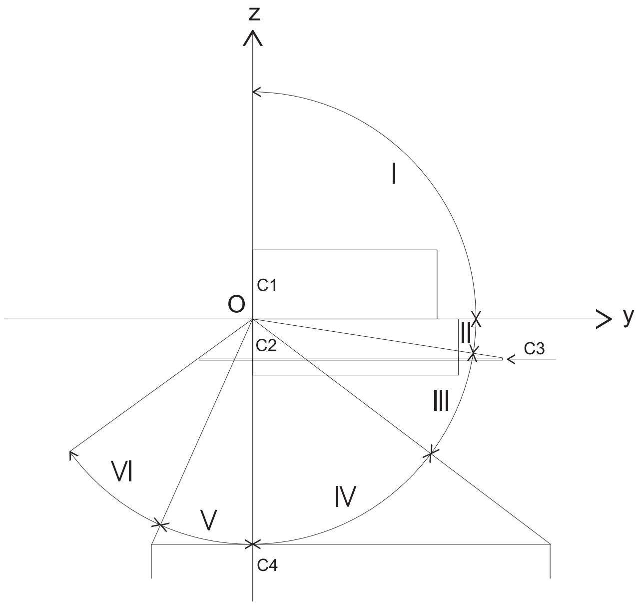

Figure B.10. Illustrating the solid angles selection [from *Bučík and Kudela*, 2003].

$$\phi_{1,2} = \arccos\left(\pm\sqrt{\frac{(r_4h_2)^2 - (l_4d_2 - bh_2)^2}{(bh_2)^2 - (l_4d_2 - bh_2)^2}}\right),$$

$$\phi_{3,4} = \arccos\left(\pm\sqrt{\frac{(r_4h_2)^2 - (l_4d_2 + h_4d_2 - bh_2)^2}{(bh_2)^2 - (l_4d_2 + h_4d_2 - bh_2)^2}}\right),$$

where $\phi_{1,2}$ and $\phi_{3,4}$ are ϕ-coordinates of θ_4 and θ_5, and θ_5 and θ_6 intersections, respectively. The subscripts 1, 2, 3 and 4 refer to the cylinders C1, C2, C3, and C4 respectively. All other symbols have been previously defined.

B.4.2 The Average Mass Thickness in the Selected Solid Angles

As an example, the selection of the solid angles may be done according to the number of different absorbers lying in the individual quadrants, what is demonstrated in Fig. B.10. The results of the Monte Carlo simulations in selected solid angles are summarized in Tab. B.6. The solid angles Ω, given in the column 4 have been found by solving eqn. B.9. Tab. B.7 lists results for another choice of the solid angles.

Design.	θ	ϕ	Ω	$\bar{s}_n$	σ_n	ε	n
I	$(0, \frac{\pi}{2})$	$(0, \pi)$	1.00π	15.60	7.04	0.16	7905
II	$(\frac{\pi}{2}, \theta_2)$	$(0, \pi)$	0.20π	26.09	12.73	0.26	9273
III	(θ_2, θ_4)	$(0, \pi)$	0.47π	30.34	12.44	0.30	6480
IV	(θ_4, π)	$(0, \pi)$	0.33π	45.87	17.87	0.46	5879
V	(θ_4, π)	$(\pi, 2\pi)$	0.13π	30.39	18.06	0.30	13573
VI	(θ_2, θ_4)	$(\pi, 2\pi)$	0.38π	4.66	1.07	0.05	2065

Table B.6. The results of the simulation of mass thickness in selected solid angles. Listed are: θ, ϕ range, the solid angle Ω (sr), the average mass thickness $\bar{s}_n$ (g cm^{-2}), the standard deviation σ_n (g cm^{-2}), 1.96σ statistical error ε (g cm^{-2}), and the number of trajectories n [from *Bučík and Kudela*, 2003].

B.5 Summary

The proposed model of the experimental setup around the CsI scintillation crystal on the CORONAS-I satellite can provide the basis for more sophisticated approach. Whatever next improvements should take into account the real variation of the density of matter near the CsI. The simulated results will also be checked after completing the information on the instruments dimensions and their masses.

Through all this paper we deal with the term *the mass thickness traversed in the absorber*, with the restriction that the particles of radiation travel in the straight lines. Since the incident trajectories are proposed to be uniformly distributed, this term has an another important interpretation, namely *the mass thickness viewed by the detector.* Thus, an amount of matter passed through by the particle can be solved by a more advanced method, called the particle transport technique.

B.6 FOV Evaluation

The SONG detector's FOV has been evaluated as a sum of products of the probabilities that the particles do not interact after crossing the thickness $\bar{s}_n$ in selected solid angle Ω,

	θ	ϕ	$\bar{s}_n$	σ_n	ε	n
Lower right quadrant	$(\frac{\pi}{2}, \pi)$	$(0, \pi)$	37.66	18.01	0.38	8831
Lower left quadrant	$(\frac{\pi}{2}, \pi)$	$(\pi, 2\pi)$	11.25	16.54	0.11	83675
Upper hemisphere	$(0, \frac{\pi}{2})$	$(0, 2\pi)$	7.79	9.26	0.08	54590
Lower hemisphere	$(\frac{\pi}{2}, \pi)$	$(0, 2\pi)$	24.44	21.74	0.24	30468
4π solid angle	$(0, \pi)$	$(0, 2\pi)$	16.24	18.75	0.16	51314

Table B.7. The results of the simulation of mass thickness in selected solid angles. Listed are: θ, ϕ range, the average mass thickness $\bar{s}_n$ (g cm^{-2}), the standard deviation σ_n (g cm^{-2}), 1.96σ statistical error ε (g cm^{-2}), and the number of trajectories n [from *Bučík and Kudela*, 2003].

and value of this solid angle. Manifestly,

$$\mathrm{FOV} = 1.49\pi + \sum \exp(-\mu \bar{\mathrm{s}}_{\mathrm{n}})\Omega \quad \mathrm{sr}, \tag{B.20}$$

where μ is the mass attenuation coefficient and 1.49π is value of the complement on whole solid angle in geometry in Fig. B.10. The summation is through the all solid angles in Tab. B.6.

Applying eqn. B.20, we find that FOV in energy ranges of $0.12 - 0.32$ and $3 - 8.3$ MeV equals to 1.8π sr and 2.9π sr, respectively. The mass attenuation coefficient, averaged in both energy channels was taken for aluminium, as a most common construction material in satellite platforms. For lower energies its value equals to 1.3×10^{-1} cm^2 g^{-1} [*Hubbell and Seltzer*, 1997].

Appendix C

The SONG Database

The telemetry data from the SONG instrument are stored in Institute of Terrestrial Magnetism, Ionosphere, and Radiowave Propagation (IZMIRAN), Russian Academy of Sciences. Before processing, the telemetry data were decoded at Institute of Nuclear Physics, MSU. Obtained data files contain detector count rates per second in the particular energy channels, and Universal Time (UT). The production of the gamma-ray database was comprised into the two basic steps: (1) calculation of the satellite trajectory and required physical quantities for the times that cover our data measurements. The results of the computation are coordinate files, (2) connection of the data files with coordinate ones.

The most easy way how to calculate satellite trajectory is using so called two-line element (TLE) sets, produced by the North American Aerospace Defense Command (NORAD) which is responsible for tracking all satellites on a daily basis. Daily updated orbital TLE's are mean Keplerian orbital element sets, available free of charge via internet. The satellite's position (Geocentric Equatorial Inertial (GEI) coordinates) in earth orbit in a particular time was calculated by NORAD SGP-4 (Simplified General Perturbation) model [*Hoots and Roehrich*, 1988]. Finally, the satellite position in GEI system has been transformed to the Geographic (GEO) [*Hapgood*, 1992] and than to the spherical geodetic [*Kelso*, 1992] coordinates.

McIlwain's L parameter and components of the magnetic field vector have been calculated by IGRF/FELDG/SHELLG software package distributed by National Space Science Data Center (NSSDC). The subroutines SHELLG and FELDG, developed by *Kluge* [1972], determine L-value and magnetic field components, respectively. The subroutine SHELLG computes the L-shell parameter from I and B by using McIlwain's [1961] formulas. The value of the integral invariant I is determined by numerically integrating along the field line from the specified point of interest to its conjugate point. The IGRF model represents the Earth's main field without external sources. It use a spherical harmonics expansion of the scalar potential in geocentric coordinates.

Bibliography

IDL, Research Systems, Inc., Boulder, 1992.

Abel, B., and R. M. Thorne, Modeling energetic electron precipitation near the South Atlantic Anomaly, *J. Geophys. Res.*, *104*, 7037, 1999.

Abramenko, V. V., S. E. Belousov, S. Y. Dudkin, G. V. Lupenko, T. I. Morozova, N. I. Nazarov, N. N. Pavlov, V. P. Sukhanov, and A. F. Titienkov, Experiment in Cosmos-1870 satellite. 1. Investigation of electron energetic spectrum in $8-30$ MeV in cosmic rays in geomagnetic equator range, Technical Report SINP MSU-7/155, Institute of Nuclear Physics, MSU, Moscow, 1990.

Akyüz, A., D. Bhattacharya, K. W. Chuang, D. D. Dixon, T. J. O'Neill, O. T. Tümer, R. S. White, and A. D.Zych, Atmospheric gamma rays at geomagnetic latutides of $-29°$ and $+43°$, *J. Geophys. Res.*, *102*, 17,359, 1997.

Allkofer, O. C., and P. K. F. Grieder, *Cosmic Rays on Earth*, *Physics Data*, vol. 25-1, Fach-informations-zentrum, Karlsruhe, Germany, 1984.

Baker, D. N., J. B. Blake, R. W. Klebesadel, and P. R. Higbie, Highly relativistic electrons in the Earth's outer magnetosphere, 1, Lifetimes and temporal history 1979 – 1984, *J. Geophys. Res.*, *91*, 4265, 1986.

Baker, D. N., S. G. Kanekal, J. B. Blake, and T. I. Pulkkinen, The global efficiency of relativistic electron production in the earth's magnetosphere, *J. Geophys. Res.*, *106*, 19,169, 2001.

Baláž, J., A. V. Dmitriev, M. A. Kovalevskaya, K. Kudela, S. N. Kuznetsov, I. N. Myagkova, Y. I. Nagornikh, J. Rojko, and S. P. Ryumin, Solar flare energetic neutral emission measurements in the project CORONAS-I, in *Solar Coronal Structures*, *IAU Colloq.*, vol. 144, edited by V. Rušin, P. Heinzel, and J. C. Vial, VEDA, Bratislava, 1994.

Barwick, S. W., et al., Cosmic ray reentrant electron albedo: High-Energy Antimater Telescope ballon measurements from Fort Sumner, New Mexico, *J. Geophys. Res.*, *103*, 4817, 1998.

Beliaev, A. A., R. A. Nymmik, M. I. Panasyuk, T. I. Pervaya, and A. A. Suslov, Local interstellar spectra of galactic cosmic rays according to particle flux analysis, *Radiat. Meas.*, *29*, 481, 1996.

Beuermann, K. P., Secondary electrons and photons in the upper atmosphere, *J. Geophys. Res.*, *76*, 4291, 1971.

Beutier, T., and D. Boscher, A three-dimensional analysis of the electron radiation belt by the Salammbô code, *J. Geophys. Res.*, *100*, 14,853, 1995.

Blake, J. B., W. A. Kolasinski, R. W. Fillus, and E. G. Mullen, Injection of electrons and protons with energies of tens of MeV into $L < 3$, *Geophys. Res. Lett.*, *19*, 821, 1992.

Blake, J. B., U. S. Inan, M. Walt, T. F. Bell, J. Bortnik, D. L. Chenette, and H. J. Christian, Lightning-induced energetic electron flux enhancements in the drift loss cone, *J. Geophys. Res.*, *106*, 29,733, 2001a.

Blake, J. B., R. S. Selesnick, D. N. Baker, and S. Kanekal, Studies of relativistic electron injection events in 1997 and 1998, *J. Geophys. Res.*, *106*, 19,157, 2001b.

Blake, J. B., M. D. Looper, K. R. Lorentzen, K. Kudela, and R. Bučík, Correlation of spacecraft observations of energetic gamma ray fluxes with those of relativistic electrons in the drift loss cone, *Geophys. Res. Abs.*, *4*, 2002, 27th General Assebmly EGS, Nice, France, 21–26 April 2002, Abstarct 00774.

Bogomolov, A. V., A. V. Dmitriev, S. N. Kuznetsov, I. N. Myagkova, S. P. Ryumin, and K. Kudela, Investigation of GCR with the help of SONG instrument on-board CORONAS-I satellite, *Proc. 24th Int. Cosmic Ray Conf.*, *4*, 836, 1995.

Bogomolov, A. V., S. N. Kuznetsov, I. N. Myagkova, S. P. Ryumin, and Y. I. Nagornikh, Latitude dependences of energetic neutrons and gamma-rays measured on the orbital complex Salute-7-Kosmos-1686, *Radiat. Meas.*, *26*, 531, 1996.

Bogomolov, A. V., R. Bučík, A. V. Dement'yev, Y. I. Denisov, A. V. Dmitriev, K. Kudela, M. I. Kudryavtsev, I. N. Myagkova, S. P. Ryumin, S. I. Svertilov, and N. M. Sobolevskiy, Energetic neutron and gamma-ray fluxes observed on board CORONAS-I satellite, Salute-7-Kosmos-1686 orbital complex and Mir orbital station, *32nd Scientific Asembly of Cospar Abstracts*, p. 395, 1998a.

Bogomolov, A. V., A. V. Dmitriev, I. N. Myagkova, S. P. Ryumin, O. N. Smirnova, and I. M. Sobolevsky, Energetic neutron and gamma-ray spectra under the Earth radiation belts according to "Salute-7-Kosmos-1686" orbital complex and "CORONAS-I" satellite data, *Adv. Space Res.*, *21*, 1801, 1998b.

Bogomolov, A. V., R. Bučík, A. V. Dement'yev, A. V. Dmitriev, K. Kudela, M. I. Kudryavtsev, I. N. Myagkova, S. P. Ryumin, S. I. Svertilov, and N. M. Sobolevskiy, Fluxes and spectra of secondary neutrons with energies $>$ 20 MeV and gamma-rays with energies $>$ 0.12 MeV on CORONAS-I satellite, Salute-7-Kosmos-1686 orbital complex and Mir orbital station (in Russian), *Izv. Akad. Nauk Ser. Fiz.*, *63*, 1660, 1999.

Bogomolov, A. V., V. V. Bogomolov, Y. I. Denisov, Y. I. Logachev, S. I. Svertilov, M. I. Kudryavtsev, V. I. Lyagushin, and T. V. Ershova, The properties of gamma-radiation and high-energy neutron fuxes in "Mir" station orbit, *Radiat. Meas.*, *35*, 473, 2002.

Bogomolov, A. V., A. P. Ignat'ev, K. Kudela, S. N. Kuznetsov, Y. I. Logachev, O. V. Morozov, I. N. Myagkova, S. N. Oparin, A. A. Pertsov, S. I. Svertilov, and B. Y. Yushkov, Parameters of the intense X-ray and gamma-ray radiation from the solar flare of May 20, 2002, as observed from the Coronas-F spacecraft, *Astron. Letters*, *29*, 199, 2003.

Brautigam, D. H., and J. T. Bell, CRRESELE documentation, Technical Report PL-TR-95-2128, Phillips Laboratory, Hanscom, AFB, MA, 1995.

Buslenko, N. P., and Y. A. Schreyder, *Monte Carlo Methods*, Fizmatgiz, Moscow, 1961.

Bučík, R., and K. Kudela, On mass in 4π solid angle around SONG CsI scintillator aboard CORONAS-I satellite, *Acta Phys. Slovaca*, *53*, 329, 2003.

Bučík, R., A. V. Dmitriev, K. Kudela, and S. P. Ryumin, Gamma-radiation of the Earth's atmosphere from the CORONAS-I data, *Proc. 26th Int. Cosmic Ray Conf.*, *7*, 433, 1999a.

Bučík, R., K. Kudela, A. V. Bogomolov, S. N. Kuznetsov, I. N. Myagkova, and S. P. Ryumin, Survey of "the geomagnetically trapped" low energy gamma radiation, in *WDS'99, Proc. of Contributed Papers*, edited by J. Šafránková, MFF UK, Prague, 1999b.

Bučík, R., K. Kudela, A. V. Bogomolov, I. N. Myagkova, S. N. Kuznetsov, and S. P. Ryumin, Distribution of gamma ray fluxes at altitude 500 km: CORONAS-I data, *Acta Phys. Slovaca*, *50*, 267, 2000.

Bučík, R., K. Kudela, S. N. Kuznetsov, I. N. Myagkova, and S. P. Ryumin, Changes in cosmic ray intensity observed on CORONAS-I satellite during magnetic storms in April 1994, *Proc. of ICRC 2001*, p. 3520, 2001.

Bučík, R., A. Dmitriev, K. Kudela, and S. Ryumin, Model of gamma-ray fluxes on CORONAS satellites, *Proc. of Space Radiation Environment Workshop*, 2002a.

Bučík, R., K. K. A. V. Dmitriev, S. N. Kuznetsov, I. N. Myagkova, and S. P. Ryumin, Spatial distribution of low energy gamma-rays associated with trapped particles, *Adv. Space Res.*, *30*, 2843, 2002b.

Bučík, R., K. Kudela, S. N. Kuznetsov, and I. N. Myagkova, The fluxes of gamma rays in the magnetic coordinates $L-B$ at CORONAS-I altitude, *Space Weather, Special Theme section - Proceedings of ISEC 2003, Toulouse: Conference on Radiation belt and Solar energetic particle Science*, 2003a, submitted.

Bučík, R., K. Kudela, A. V. Dmitriev, S. N. Kuznetsov, I. N. Myagkova, and S. P. Ryumin, Review of electron fluxes within the local drift loss cone: Measurements on CORONAS-I satellite, *Adv. Space Res.*, 2003b, in press.

Cayton, T. E., M. Tuszewski, J. C. Ingraham, and R. M. Kippen, Bremsstrahling effects in energetic particle detectors: Nature's flanking maneuver, Paper presented at ISEC 2003: Radiation Belt Science, Toulouse, France, 2–5 September 2003.

Chupp, E. L., *Gamma-ray Astronomy*, D. Reidel, Dordrecht, Holland, 1976.

da Costa Ferreira Neri, J. A., B. Agrinier, and J. M. Lavigne, Measurement of atmospheric and diffuse radiation using a time-of-flight telescope, *J. Geophys. Res.*, *97*, 1541, 1992.

Daniel, R. R., and S. A. Stephens, Cosmic-ray-produced electrons and gamma rays in the atmosphere, *Revs. of Geophys. and Space Phys.*, *12*, 233, 1974.

Dean, A. J., F. Lei, K. Byard, A. Goldwurm, and C. J. Hall, Radioactivity induced background noise in space-borne astronomical gamma-ray telescopes employing inorganic scintillation spectrometers, *Experimental Astron.*, *1*, 35, 1989.

Dean, A. J., F. Lei, and P. J. Knight, Background in space-borne low-energy γ-ray telescopes, *Space Sci. Rev.*, *57*, 109, 1991.

Dean, A. J., A. J. Bird, N. Diallo, C. Ferguson, J. J. Lockley, S. E. Shaw, M. J. Westmore, and D. R. Willis, The modelling of background noise in astronomical gamma ray telescopes, *Space Sci. Rev.*, *105*, 285, 2003.

Dmitriev, A. V., K. Kudela, S. N. Kuznetsov, I. N. Myagkova, J. Rojko, and S. P. Ryumin, The SONG device for detection of the solar flare neutron and gamma radiation in CORONAS experiment (in Russian), *Izv. Akad. Nauk Ser. Fiz.*, *57*, 27, 1993.

Efimov, Y. E., A. A. Gusev, K. Kudela, L. Just, and G. I. Pugacheva, Spatial distribution of albedo particles on altitudes $\sim$ 500 km, *Czech. J. Phys. B*, *35*, 1371, 1985.

Fichtel, C. E., D. A. Kniffen, and H. B. Ögelman, Results of gamma-ray astronomy, *Astrophys. J.*, *158*, 193, 1969.

Fishman, D. J., et al., Discovery of intense gamma-ray flashes of atmospheric origin, *Science*, *264*, 1313, 1994.

Flückiger, E. O., D. F. Smart, and M. A. Shea, On the latitude dependence of cosmic ray cutoff rigidity variations during the initial phase of a geomagnetic storm, *Proc. 20th Int. Cosmic Ray Conf.*, *4*, 216, 1980.

Galper, A. M., S. V. Koldashov, V. V. Mikhailov, S. A. Voronov, L. V. Maslenikov, and N. I. Shvetz, Energy spectrum and charge composition of a new, long-lived, unstable electron radiation belt, *J. Geophys. Res.*, *104*, 28,685, 1999.

Golenetskii, S. V., E. P. Mazets, V. N. Il'inskii, R. L. Aptekar', M. M. Bredov, Y. A. Gur'yan, and V. N. Panov, Cosmic gamma-ray measurements in the range 0.3 to 3.7 MeV, *Astrophys. Lett.*, *9*, 69, 1971.

Graser, U., and V. Schönfelder, Theoretical zenith angle distribution of atmospheric MeV gamma radiation at high balloon altitudes, *J. Geophys. Res.*, *82*, 1055, 1977.

Gur'yan, Y. A., E. P. Mazets, M. P. Proskura, and I. A. Sokolov, Atmospheric hard gamma ray studies on Kosmos 461, *Geomagn. Aeron.*, *19*, 11, 1979.

Gusev, A. A., G. I. Pugacheva, L. Just, and K. Kudela, On the sources of high energy electrons trapped in the inner radiation zone, *Planet. Space Sci.*, *35*, 1281, 1987.

Hapgood, M. A., Space physics coordinate transformations: A user guide, *Planet. Space. Sci.*, *40*, 711, 1992.

Harris, M. J., G. H. Share, and M. D. Leising, Spatial and temporal variability of the gamma radiation from Earth's atmosphere during a solar cycle, *J. Geophys. Res.*, 2003, in press.

Hoots, F. R., and R. L. Roehrich, Models for propagation of NORAD element sets, *Spacetrack Report*, vol. 3, edited by T. S. Kelso, Department of Commerce, Springfield, VA, 1988.

Hubbell, J. H., and S. M. Seltzer, Tables of X-ray mass attenuation coefficients and mass energy-absorption coefficients (version 1.03), 1997, [Online] Available: http://physics.nist.gov/xaamdi [2003, November 26]. National Institute of Standards and Technology, Gaithersburg, MD.

Imhof, W. L., Review of energetic (> 20 keV) bremsstrahlung X-ray measurements from satellites, *Space Sci. Rev.*, *29*, 201, 1981.

Imhof, W. L., G. H. Nakano, R. G. Johnson, and J. B. Reagan, Satellite observations of bremsstrahlung from widespread energetic electron precipitation events, *J. Geophys. Res.*, *79*, 565, 1974.

Imhof, W. L., G. H. Nakano, and J. B. Reagan, High-resolution measurements of atmospheric gamma rays from a satellite, *J. Geophys. Res.*, *81*, 2835, 1976.

Imhof, W. L., H. D. Voss, M. Walt, E. E. Gaines, J. Mobilia, D. W. Datlowe, and J. B. Reagan, Slot region electron precipitation by lightning, VLF chorus, and plasmaspheric hiss, *J. Geophys. Res.*, *91*, 8883, 1986.

Johnson, W. N., R. L. Kinzer, J. D. Kurfess, M. S. Strickman, W. R. Purcell, D. A. Grabelsky, M. P. Ulmer, D. A. Hillis, G. V. Jung, and R. A. Cameron, The Oriented Scintillation Spectrometer Experiment: Instrument description, *Astrophys. J. Suppl.*, *86*, 693, 1993.

Kappadath, S. C., J. Ryan, K. Bennett, H. Bloemen, D. Forrest, W. Hermsen, R. Kippen, M. McConnell, V. Schöenfelder, R. van Dijk, M. Varendorff, G. Weidenspointner, and C. Winkler, The preliminary cosmic diffuse gamma-ray spectrum from 800 keV to 30 MeV measured with COMPTEL, *Proc. 24th Int. Cosmic Ray Conf.*, *2*, 230, 1995.

Kasturirangan, K., U. R. Rao, and P. D. Bhavsar, Low energy atmospheric gamma rays near geomagnetic equator, *Planet. Space Sci.*, *20*, 1961, 1972.

Kelso, T. S., Orbital coordinate systems, Part III, *Satellite Times*, January/February, 1992.

Kennel, C. F., and H. E. Petchek, Limit on stably trapped particle flux, *J. Geophys. Res.*, *71*, 1, 1966.

Khazanov, G. V., M. W. Liemohn, E. N. Krivorutsky, J. M. Albert, J. U. Kozyra, and B. E. Gilchrist, Relativistic electron beam propagation in the Earth's magnetosphere, *J. Geophys. Res.*, *104*, 28,587, 1999.

Kluge, G., Direct computation of the magnetic shell parameter, *Computer Phys. Communications*, *3*, 31, 1972.

Kuznetsov, S. N., et al., Preliminary results in the CORONAS-I experiment with help of the SCR scientific set of instruments (in Russian), *Izv. Akad. Nauk Ser. Fiz.*, *59*, 2, 1995.

Kuznetsov, S. N., and I. N. Myagkova, Quasi-trapped electron fluxes (> 0.5 MeV) under the radiation belts: analysis of their connection with geomagnetic indices, *J. Atmos. Terr. Phys.*, *64*, 601, 2002.

Kuznetsov, S. N., Y. V. Gotselyuk, A. N. Podorolsky, S. P. Ryumin, S. Fisher, and K. Kudela, Scientific goals and specific devices of the "Solar Cosmic Rays" (SCR) scientific set of instruments in the "CORONAS" project, *CORONAS information*, vol. 3, edited by K. Pflug, Central Institute for Astrophysics, Potsdam, Germany, 1991.

Kuznetsov, S. N., A. V. Bogomolov, A. V. Dmitriev, K. Kudela, I. N. Myagkova, and S. P. Ryumin, Investigation of the galactic cosmic ray variations onboard CORONAS-I satellite (in Russian), *Izv. Akad. Nauk Ser. Fiz.*, *61*, 1104, 1997.

Kuznetsov, S. N., I. N. Myagkova, S. P. Ryumin, K. Kudela, and H. Mavromichalaki, Forbush-effect April 17, 1994 on data of the flying detector on a board of CORONAS-I satellite, *Proc. 26th Int. Cosmic Ray Conf.*, *6*, 427, 1999.

Kuznetsov, S. N., R. Nymmik, S. P. Ryumin, B. Y. Yushkov, K. Kudela, and R. Bučík, Energetic charged particle fluxes under the radiation belts, *Proc. of ICRC 2001*, p. 1651, 2001.

Kuznetsov, S. N., K. Kudela, S. P. Ryumin, and Y. V. Gotselyuk, CORONAS-F satellite: Tasks for study of particle acceleration, *Adv. Space Res.*, *30*, 1857, 2002a.

Kuznetsov, S. N., I. N. Myagkova, S. P. Ryumin, K. Kudela, R. Bučík, and H. Mavromichalaki, Effects of the April 1994 Forbush events on the fluxes of the energetic charged particles measured on board CORONAS-I: their connection with conditions in the interplanetary medium, *J. Atmos. Sol-Terr. Phy.*, *64*, 535, 2002b.

Kuznetsov, S. N., K. Kudela, I. N. Myagkova, and B. Y. Yushkov, Gamma and X-ray solar flare emissions: CORONAS-F measurements, *Proc. 28th Int. Cosmic Ray Conf.*, *SH1*, 3183, 2003.

Lavigne, J. M., M. Niel, G. Vedrenne, B. Agrinier, E. Bonfand, B. Parlier, and K. R. Rao, Study of diffuse cosmic and atmospheric gamma radiation using a spark chamber in the energy range 4 MeV-100 MeV, *Astrophys. J.*, *261*, 720, 1982.

Lemaire, J., A. D. Johnstone, D. Heynderickx, D. J. Rodgers, S. Szita, and V. Pierrard, Final report of the TREND-2 project, Technical Report Contract No. 9828/92/NL/FM, ESA/ESTEC/WMA TRP, 1995.

Letaw, J. R., G. H. Share, R. L. Kinzer, R. Silberberg, E. L. Chupp, D. J. Forrest, and E. Rieger, Satellite observation of atmospheric nuclear gamma radiation, *J. Geophys. Res.*, *94*, 1211, 1989.

Li, X., D. N. Baker, M. Temerin, T. E. Cayton, G. D. Reeves, R. A. Christensen, J. B. Blake, M. D. Looper, R. Nakamura, and S. G. Kanekal, Multisatellite observations of the outer zone electron variation during the November $3-4$, 1993, magnetic storm, *J. Geophys. Res.*, *102*, 14,123, 1997.

Lin, R. P., et al., The Reuven Ramaty high-energy solar spectroscopic imager (RHESSI), *Solar Phys.*, *210*, 3, 2002.

Ling, J. C., A semiempirical model for atmospheric γ rays from 0.3 to 10 MeV at $\lambda = 40°$, *J. Geophys. Res.*, *80*, 3241, 1975.

Ling, J. C., and D. E. Gruber, Spectra and angular distributions of atmospheric gamma rays from 0.3 to 10 MeV at $\lambda = 40°$, *J. Geophys. Res.*, *82*, 1211, 1977.

Lockwood, J. I., and W. R. Webber, Forbush decreases and interplanetary magnetic field disturbances: associations with magnetic clouds, *J. Geophys. Res.*, *96*, 11,587, 1991.

Lyons, L. R., Magnetospheric processes leading to precipitation, *Space Sci. Rev.*, *80*, 109, 1997.

Martin, I. M., F. Albernhe, and G. Vedrenne, Variation du flux des neutrons rapides et des-rayons gamma d'origine cosmique en fonction de la latitude et de l'altitude, *Revista Brasileira de Física*, *1*, 263, 1971.

Martin, I. M., S. L. G. Dutra, and R. A. Palmeira, Calcul du spectre des photons gamma atmosphériques entre 1 et 1000 MeV, *Revista Brasileira de Física*, *5*, 43, 1975.

Mazets, E. P., S. V. Golenetskiy, V. N. Ilinskiy, Y. A. Gur'yan, and J. B. Kharitonova, Diffuse cosmic gamma-ray background in the 28 keV - 4.1 MeV range from Kosmos 461 observations, *Astrophys. Space Sci.*, *33*, 347, 1975.

McAdams, K. L., G. D. Reeves, R. H. W. Friedel, and T. E. Cayton, Multisatellite comparisons of the radiation belt response to the Geospace Envirinment Modeling (GEM) magnetic storms, *J. Geophys. Res.*, *106*, 10,869, 2001.

McIlwain, C. E., Coordinates for mapping the distribution of magnetically trapped particles, *J. Geophys. Res.*, *66*, 3681, 1961.

Meffert, J. D., and M. S. Gussenhoven, CRRESPRO documentation, Technical Report PL-TR-94-2218, Phillips Laboratory, Hanscom, AFB, MA, 1994.

Miyoshi, Y., A. Morioka, T. Obara, H. Misawa, T. Nagai, and Y. Kasahara, Rebuilding process of the outer radiation belt during the 3 November 1993 magnetic storm: NOAA and Exos-D observations, *J. Geophys. Res.*, *108*, 1004, 2003.

Morris, D. J., Production of high-energy gamma rays by cosmic ray interactions in the atmosphere and lunar surface, *J. Geophys. Res.*, *89*, 10,685, 1984.

Murphy, R. J., D. M. Smith, G. H. Share, R. A. Schwartz, A. Y. Shih, and R. P. Lin, Solar gamma-ray lines at high resolution with RHESSI, *Proc. 28th Int. Cosmic Ray Conf.*, *SH1*, 3187, 2003.

Nagata, K., H. Kondo, T. Kohno, H. Murakami, A. Nakamoto, N. Hasebe, J. Kikuchi, and T. Doke, The geographical distributions of electrons (0.05 – 3.2 MeV) and protons (0.58 – 35 MeV) at altitudes of 350 – 850 km, Technical Report ISAS RN 358, The Institute of Space and Astronautical Science, Komaba, Meguro, Tokyo 153, 1987.

Paulikas, G. A., and J. B. Blake, Effects of the solar wind on magnetospheric dynamics: Energetic electrons at the synchronous orbit, in *Quantitative Modeling of Magnetospheric*

Processes, *Geophys. Monogr. Ser.*, vol. 21, edited by W. P. Olsen, AGU, Washington, DC, 1979.

Press, W. H., S. A. Teukolsky, W. T. Vetterling, and B. P. Flannery, *Numerical Recipes in C: The Art of Scientific Computing*, Cambridge University Press, Cambridge, 1992.

Ralston, A., and P. Rabinowitz, *A First Course in Numerical Analysis*, McGraw-Hill, New York, 1978.

Ramaty, R., and R. E. Lingenfelter, Gamma-ray astronomy, *Ann. Rev. Nucl. Part. Sci.*, *32*, 235, 1982.

Reeves, G. D., Relativistic electrons and magnetic storms: 1992-1995, *Geophys. Res. Lett.*, *25*, 1817, 1998.

Réveillé, T., P. Bertrand, A. Ghizzo, F. Simonet, and N. Baussart, Dynamic evolution of relativistic electrons in the radiation belts, *J. Geophys. Res.*, *106*, 18,883, 2001.

Roederer, J. G., *Dynamics of Geomagnetically Trappped Radiation*, Springer-Verlag, Berlin, 1970.

Rossi, B., and S. Olbert, *Introduction to the Physics of Space*, McGraw-Hill, New York, 1970.

Rostoker, G., S. Skone, and D. N. Baker, On the origin of relativistic electrons in the magnetosphere associated with some geomagnetic storms, *Geophys. Res. Lett.*, *25*, 3701, 1998.

Ryan, J. M., B. Dayton, S. H. Moon, R. B. Wilson, A. D. Zych, and R. S. White, Atmospheric gamma ray angle and energy distributions from 2 to 25 MeV, *J. Geophys. Res.*, *82*, 3593, 1977.

Ryan, J. M., M. C. Jennings, M. D. Radwin, A. D. Zych, and R. S. White, Atmospheric gamma ray angle and energy distributions from sea level to 3.5 g/cm^2 and 2 to 25 MeV, *J. Geophys. Res.*, *84*, 5279, 1979.

Ryumin, S. P., A. V. Bogomolov, A. V. Dmitriev, and I. N. Myagkova, Background conditions for recording γ radiation and energetic neutrons on CORONAS satellites from SONG data, *J. Moscow Phys. Soc.*, *6*, 423, 1996.

Sawyer, D. M., and J. I. Vette, AP-8 trapped proton environment for solar maximum and solar minimum, Technical Report NSSDC 76-06, NASA Goddard Space Flight Center, Greenbelt, Md., 1976.

Schönfelder, V., F. Graml, and F. P. Penningsfeld, The vertical component of $1-20$ MeV gamma rays at ballon altitudes, *Astrophys. J.*, *240*, 350, 1980.

Share, G. H., and R. J. Murphy, Atmospheric gamma rays from solar energetic particles and cosmic rays penetrating the magnetosphere, *J. Geophys. Res.*, *106*, 77, 2001.

Share, G. H., R. L. Kinzer, M. S. Strickman, J. R. Letaw, and E. L. Chupp, Instrumental and atmospheric background lines observed by the SMM gamma-ray spectrometer, in *High-Energy Radiation Background in Space*, *AIP Conf. Proc.*, vol. 186, edited by A. C. Rester and J. I. Trombka, American Institute of Physics, New York, 1989.

Share, G. H., R. J. Murphy, B. R. Dennis, R. A. Schwartz, A. K. Tolbert, R. P. Lin, and D. M. Smith, RHESSI observation of atmospheric gamma rays from impact of solar energetic particles on 21 april 2002, *Solar Phys.*, *210*, 357, 2002.

Share, G. H., R. J. Murphy, J. G. Skibo, D. M. Smith, H. S. Hudson, R. P. Lin, A. Y. Shih, B. R. Dennis, and R. A. Schwartz, RHESSI observation of the solar annihilation line, *Proc. 28th Int. Cosmic Ray Conf.*, *SH1*, 3199, 2003.

Shea, M. A., D. F. Smart, and L. C. Gentile, Estimating cosmic ray vertical cutoff rigidities as a function of the McIlwain L-parameter for different epochs of the geomagnetic field, *Phys. of the Earth and Planet. Interiors*, *48*, 200, 1987.

Sheldon, W. R., and J. R. Benbrook, The interaction of the outer belt with the atmosphere, Paper presented at ISEC 2003: Radiation Belt Science, Toulouse, France, 2–5 September 2003.

Smart, D. F., M. A. Shea, E. O. Flückiger, A. J. Tylka, and P. R. Boberg, Changes in calculated vertical cutoff rigidities at the altitude of the International Space Station as a function of geomagnetic activity, *Proc. 26th Int. Cosmic Ray Conf.*, *7*, 337, 1999.

Summers, D., and C. Y. Ma, A model for generating relativistic electrons in the Earth's inner magnetosphere based on gyroresonant wave-particle interactions, *J. Geophys. Res.*, *105*, 2625, 2000.

Thompson, D. J., A three-dimensional study of 30− to 300− MeV atmospheric gamma rays, *J. Geophys. Res.*, *79*, 1309, 1974.

Thompson, D. J., G. A. Simpson, and M. E. Özel, SAS2 observations of the Earth albedo gamma radiation above 35 MeV, *J. Geophys. Res.*, *86*, 1265, 1981.

Trombka, J. I., and C. E. Fichtel, Gamma-ray astrophysics, *Phys. Rev. (Letters)*, *97*, 173, 1983.

Truscott, P. R., C. S. Dyer, P. S. Haskins, and J. E. McKisson, *IEEE Trans. Nucl. Sci.*, *42*, 946, 1995.

Vampola, A. L., and D. J. Gorney, Electron energy deposition in the middle atmosphere, *J. Geophys. Res.*, *88*, 6267, 1983.

Vampola, A. L., and G. A. Kuck, Induced precipitation of inner zone electrons. Volume I: Observations, Technical Report SAMSO-TR-77-134, The Aerospace Corporation, Los Angels, CA, 1977.

Vette, J. I., The AE-8 trapped electron model environment, Technical Report NSSDC 91-24, NASA Goddard Space Flight Center, Greenbelt, Md., 1991.

Voss, H. D., et al., Lightning-induced electron precipitation, *Nature*, *312*, 740, 1984.

Walt, M., *Introduction to Geomagnetically Trapped Radiation*, University Press, Cambridge, Great Britain, 1994.

Willett, J. B., and W. A. Mahoney, High spectral resolution measurement of gamma ray lines from the earth's atmosphere, *J. Geophys. Res.*, *97*, 131, 1992.

Xinlin, L., I. Roth, M. Temerin, J. R. Wygant, M. K. Hudson, and J. B. Blake, Simulation of the prompt energization and transport of radiation belt particles during the March 24, 1991 SSC, *Geophys. Res. Lett.*, *20*, 2423, 1993.

Yoshimori, M., S. Nakayama, H. Takeda, H. Ogawa, and S. Masuda, Recent Yohkoh solar gamma-ray observations, *Proc. 27th Int. Cosmic Ray Conf.*, *SH1*, 3017, 2001.

Yoshimori, M., H. Hirayama, and S. Mori, Energetics of nonthermal electrons and protons in intense solar flares, *Proc. 28th Int. Cosmic Ray Conf.*, *SH1*, 3191, 2003.